Università degli Studi di Cagliari

DOTTORATO DI RICERCA

Ingegneria Elettronica ed Informatica

Ciclo XXXI

TITOLO TESI

SPACE DEBRIS OBSERVATIONS WITH THE SARDINIA RADIO TELESCOPE

Settore/i scientifico disciplinari di afferenza

ING-INF/02

Presentata da:	Giacomo Muntoni
Coordinatore Dottorato:	prof. Fabio Roli
Tutor:	prof. Giorgio Montisci

Esame finale anno accademico 2017 – 2018

Tesi discussa nella sessione d'esame Febbraio 2019

Osservatorio
Astronomico
di Cagliari

SPACE DEBRIS OBSERVATIONS WITH THE SARDINIA RADIO TELESCOPE

Doctoral Thesis by:

Giacomo Muntoni

Advisor:

Prof. Giorgio Montisci

CONTENTS

ABSTRACT

Space debris are manmade objects orbiting around Earth that represent a growing problem for on-going and future space operations. In order to avoid possible collisions between debris and spacecraft and to monitor the objects during the re-entry process, gathering as much information as possible about them is a primary need. These information can be acquired by means of radar or optical measurements depending on the observing scenario.

Among the worldwide radio telescopes, the Sardinia Radio Telescope (SRT) is a new comer in the space debris detection plan. Although it has been used for several years to acquire and analyze distant radio astronomical sources, only recently it has been tested for space debris detection purposes. For this reason the research group of the Department of Electrical and Electronic Engineering of the University of Cagliari, in collaboration with the Cagliari Astronomical Observatory (OAC), has studied a set of upgrades for the L-P band receiver of the SRT, in order to make the antenna a suitable instrument within the European space debris detection plan.

This doctoral dissertation focuses on the characterization and upgrade of the receiving system and on the test of the whole receiving chain before and after the upgrade.

INTRODUCTION

The start of the so called “Space Age” can be placed symbolically on 1 October 1957, with the launch of the first man-made satellite Sputnik I, due to the Russian space program. Since then, the goal of the space exploration led to the enthusiastic rush to the stars, concerning the main world powers such as Russia itself and United States with the Apollo program. However, at that time, there was no concern about the possible pollution of the space environment with the space operations discards. This initial negligence is the primary cause of the present congestion of the near-Earth orbits. The above mentioned objects are usually referred as space debris or orbital debris.

Space debris are comprised of man-made orbiting objects, with various sizes and shapes, including payloads for the most part, but nonetheless even rocket bodies, satellite fragments and other objects, once part of a spacecraft, that have ceased to be active [1]. The presence of these objects represents a serious threat for ongoing and future space operations, since spacecraft may collide with them and become damaged, or, in the worst case, destroyed in the process. Smaller debris can be partially stopped with the application of some shields onto the spacecraft bodies but, in order to face the hazard of the bigger ones, the constant monitoring of the most populated orbits is necessary.

In order to monitor the space situation and to determine the effective level of threat of the space debris, some measurements are required. These measurements can be split in two categories: ground- and space-based measurements. Space-based measurements are meant to gather information about the small-sized debris, the sub millimeter-sized particles in particular, thanks to the detection surfaces, namely detection devices that can be launched in space for space debris exposure. The detection devices may serve as impact detectors, to study the type and speed of the smaller debris, or as particle catchers, for further analysis of the objects once the device is retrieved after its return on Earth. However, due to the cost, these operations are possible only in near-Earth orbits (i.e. Low Earth Orbit, between 200 and 2000 km from Earth’s surface). On the other hand, ground-based measurements fall in two categories: radar and optical measurements. Radar measurements are typically used to detect and track space debris in Low Earth Orbit (LEO) [2], while optical measurements can perform the same task but at higher orbits. The reason of this difference is related to the observation’s conditions and to the power needed. In fact, optical observations are tied to the weather conditions and to the time of the day: they are able to detect a debris only when illuminated by the sun within a dark background (in lower orbits this is possible only shortly after sunset of before sunrise) in clear sky

conditions. These constraints do not affect radar measurements. However, if we consider the power budget, radar measurements require high levels of power that increase together with the distance of the object (distance to the fourth power to be precise), while optical measurements are passive detectors, i.e. they take advantage of the power reflected by the object from a source (the sun), so that the power travelling back toward the optical receiver decreases only with the square of the distance.

Since the space debris problem is becoming more and more important, in recent years, some important organizations, such as the Inter Agency Space Debris Coordination Committee (IADC) and the United Nation, have published space debris mitigation guidelines in order to take control over the space situation [3]. Other than that, the United States, through the Department of Defense (DoD), can count on a complete and efficient network of radio and optical detectors that allow a thorough surveillance of the objects resident in space. Thanks to this knowledge, the United States Strategic Command (USSTRATCOM) is able to maintain a catalogue of a portion of the total population of the space debris (larger than 10 cm) that settles in around 20 000 units [4]. Clearly, within this context, even the European Space Agency (ESA) has drawn up its program, to safeguard the space environment, with the Space Situation Awareness (SSA) program and, as a branch of this program, with the Space Surveillance and Tracking (SST) segment. It is in this framework that an SST agreement between the Italia Space Agency (ASI), representing Italy as a member state of the ESA, and the National Institute for Astrophysics (INAF) was born. One of the most important instrument available to INAF is the Sardinia Radio Telescope (SRT) which is managed by the Cagliari Astronomical Observatory (OAC).

The SRT is a new comer in the space debris detection plan, but it has already shown its potential [5]. This 64-m parabolic dish is located near San Basilio, in Sardinia (Italy) and it is one of the largest radio telescopes in the world provided with an active surface system [6]. Some preliminary space debris-related observations have already been made in 2014, with a view to the above mentioned SST agreement, showing that the radio telescope is suitable for these types of observations. However it is worth mentioning that the SRT is not actually provided with a space debris dedicated receiving chain, since the antenna is devoted mainly to radio astronomical observations and furthermore it is able to work only in beam park mode, for survey observations. For this reason, the DIEE and OAC research group have studied, designed and tested a brand new receiving channel of the SRT for space debris monitoring (and tracking) in order to make the radio telescope

and the entire Bistatic Radar for LEO Tracking (BIRALET) system a suitable instrument within the European Space Situational Awareness (EU-SSA).

This doctoral dissertation is organized as follows: chapter 1 gives a complete overview of the space debris problem and the actual countermeasures employed to mitigate the space pollution. Chapter 2 offers a light approach on the theory behind the radar measurements. In chapter 3, a summary of the state of the art regarding radio telescopes employed worldwide in space debris monitoring, is assessed. The main characteristics of the Sardinia Radio Telescope will be discussed in chapter 4. One of the main cores of this work concerns the first observations of space debris ever made with the SRT, which are described in chapter 5. Every aspect of the upgrade of the Sardinia Radio Telescope (update of the receiving chain, tracking mode) is addressed in chapter 6. The implications of the doctoral dissertation are explained in the seventh and final chapter.

1. THE SPACE DEBRIS PROBLEM

More than 330 million pieces of debris are estimated to populate the orbits around Earth: the Low Earth Orbit (LEO), between 200 and 2 000 km, the Medium Earth Orbit (MEO), between 2 000 and 35 786 km, and the Geostationary Earth Orbit (GEO), at 35 786 km from Earth's surface. Within this quantity, only 18 000 units have an average size larger than 10 cm and only 560 000 units range from 1 to 10 cm. This means that for the most part the orbital debris have an average size smaller than 1 cm [7]. In near-Earth space the presence of the debris is more significant – for objects larger than a few millimeters – than natural meteoroids. The risk represented by the space debris is double:

- A collision risk, that may occur between a debris and a spacecraft or between debris themselves;
- A re-entry risk, that happens when the orbital life of a debris comes to its end.

Debris populating lower orbits must struggle with the gravity attraction from the Earth and so, to maintain a regular orbit, they travel at typical speeds of 10 km/s. With this velocities at stake, even smaller debris can cause catastrophic break-ups. A collision event may lead to a cascading process in which the impact generates more fragments, other than damage spacecrafts. This self-sustained growth in the object population has been predicted and studied by Donald Kessler and so named after him - and known today as - "Kessler syndrome". A graphical representation of the problem is shown in Fig. 1.1, for objects larger than 10 cm. It can be noticed the predominance of the objects in LEO.

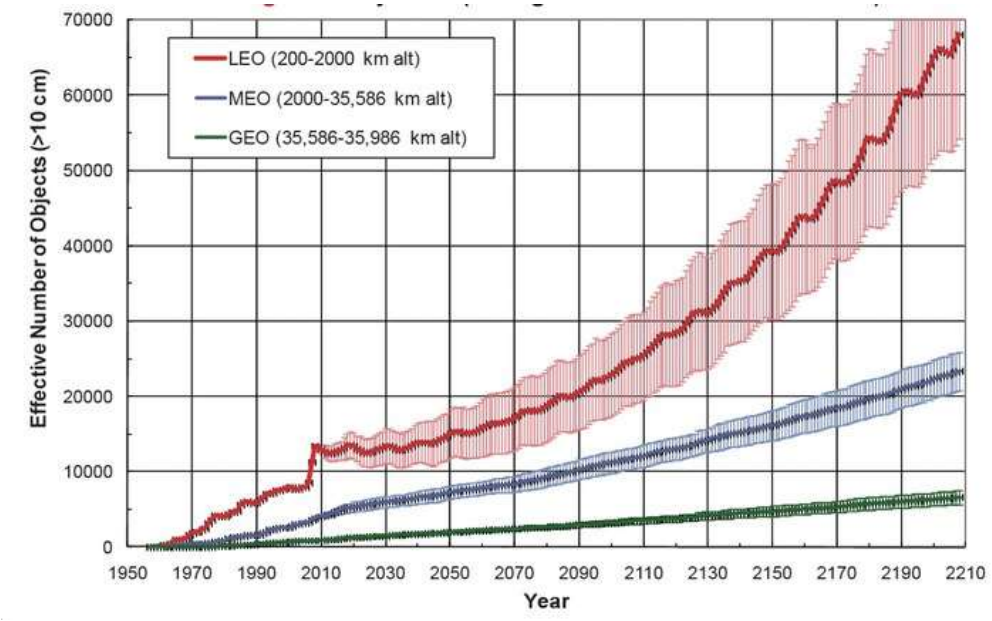

Fig. 1.1. Graphical representation of the Kessler syndrome.

An interesting fact that arises from this graph is the sudden increase of the red curve slope, around year 2007. Indeed, for the most part, the catalogued objects are originated by break-up events. Two of them are responsible for a considerable increase in the space debris population: the anti-satellite Chinese test on January 2007, that completely destroyed the weather satellite Feng Yun-1C, increasing the total population of orbital debris by a 25% and the accidental collision between two satellites – the Iridium-33 and the Cosmos-2251 -causing a further increase of the population by a 16%.

As for the re-entry risk, when a spacecraft lifetime decays, the orbit of the object and the orbit of the Earth collide. Smaller debris does not represent a serious threat, because of their reduced size, in fact they are vaporized by the friction with the atmosphere. However, larger objects may re-enter in the atmosphere and there is a small but definitely not negligible chance that they land in an inhabited area. For instance, recently, the re-entry of the Chinese space station Tiangong-1 aroused great interest worldwide and was constantly monitored in the first months of the 2018.

From the situation described above, the necessity to monitor and catalog the population of the space debris is born. The most extensive database of catalogued objects is held by the NASA with its Satellite Situation Report (SSR) and by the US Strategic Command USSTRATCOM (formerly known as US Space Command USSPACECOM) with its TLE (Two-Line Element set) catalogue that will be described later in this chapter. In both cases the major source of information are the observation data and orbit determination performed by the US Space Surveillance Network (SSN), that can count on a total number of 25 observation sites worldwide, both optical and radar [7]. The US Joint Space Operation Center (JSpOC) act as coordinator for the large amount of data coming from the SSN sensors, elaborating the orbital information and making them available in a recognizable and ready-to-use format, i.e. the above cited TLEs. Given the importance of the space debris problem, also Europe has started a program devoted to the space surveillance activity. The European Space Agency (ESA), following the steps of US Strategic Command, gave birth to the Space Situational Awareness (SSA) program and within it to the Space Surveillance and Tracking (SST) segment focused on the creation and maintaining of a catalog of all orbiting objects.

Mitigation guidelines for space debris include:

- the monitoring of the orbiting objects using radar and optical measurements from ground as well as from space;

- the design of new spacecraft which, in the event of a break-up, will be divided into as few pieces as possible, minimizing a further increase in the debris population;
- the study of the so called Active Debris Removal (ADR), a number of methods aimed to the disposal of the useless orbiting objects.

These mitigation guidelines have been studied and described by the Inter Agency Space Debris Coordination Committee (IADC), an international governmental committee for the worldwide coordination of activities related to the problem represented by the space debris. The IADC member agencies count a total of 12 nations besides ESA: Italy (Agenzia Spaziale Italiana – ASI), France (Centre Nationale d'Etudies Spatiales – CNES), China (China National Space Administration – CNSA), Canada (Canadian Space Agency – CSA), Germany (German Aerospace Center – DLR), India (Indian Space Research Organization – ISRO), Japan (Japan Aerospace Exploration Agency – JAXA), Korea (Korea Aerospace Research Institute – KARI), United States (National Aeronautics and Space Administration – NASA), Russia (State Space Corporation – ROSCOSMOS), Ukraine (State Space Agency of Ukraine – SSAU) and United Kingdoms (UK Space Agency). One of the primary purposes of the IADC is to synchronize the efforts of the members involved and to exchange information between space agencies in order to ease the cooperation in space debris research, to control the progress of ongoing space actions and to identify debris mitigation options.

1.1 Two-Line Element set

As already said, the information on space debris contained in the catalogue held by the NASA and the USSTRATCOM and made available thanks to the JSpOC, are in the form of Two-Line Element set, a particular data format which include the orbital parameters of known objects orbiting around Earth in a specific astronomical epoch. They appear as a simple text file in ASCII code with two (or three if the name of the object is included) rows. These information are extremely useful to predict the position of the object to observe and, thereby, to properly point the transmitting and receiving antennas. An example of TLE is reported in Fig. 1.2. It is possible to identify the fields that define this particular format. The meaning of every field is reported hereafter:

- *Name of Satellite*. When the TLE is given in the 3 rows format (in this case is named 3LE), the first field is the name associated with the orbital element. This is true for satellite as well as for space debris. In the case of space debris the most

common stamp is the name of the satellite/spacecraft from which the debris derived followed by a number (e.g. Cosmos 2238).

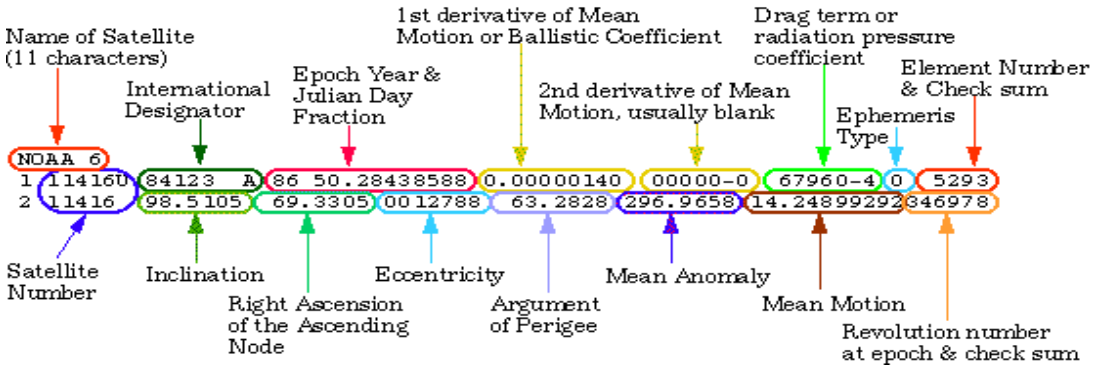

Fig. 1.2. Example of a TLE, with the identification of every field.

- *Satellite Number*. A 5-digit number assigned to the object in the USS STRATCOM catalogue.
- *International Designator*. In this field, the first two digits represent the last two of the launch year (in the example would be 1984), whereas the remaining digits represent the number of objects already launched in the same year. The capital letter at the end identifies the part of the launched spacecraft.
- *Inclination*. It is the angle, measured in degrees, between the equator and orbital plane.
- *Epoch Year and Julian Day Fraction (JDF)*. This number represents the date of the release of the TLE (the astronomical epoch). The first two digits represents the year, the JDF represents the number of days elapsed starting from the 1st January of that year.
- *Right Ascension of the Ascending Node (RAAN)*. It is the angle, expressed in degrees, between the spring equinox and the point where the orbit of the object crosses the equatorial plane.
- *Eccentricity*. It is a constant value ranging from 0 to 1, which defines the shape of the orbit of the object. A value of 0 is associated with an elliptical orbit, whereas a value of 1 is associated with a circular orbit.
- *1st derivative of Mean Motion (Ballistic Coefficient)*. It represents the daily fraction of changes in the number of revolutions made by the object, expressed in revolutions/day.
- *Argument of Perigee*. It is the angle, expressed in degrees, between the RAAN and the perigee of the object's orbit.

- *2nd derivative of Mean Motion*. It measures the second derivative of the daily mean motion of the object, expressed in revolutions/day^3.
- *Mean Anomaly*. It is the angle, measured from the perigee and expressed in degrees, of the position of the object in orbit, referred to a circular orbit with radius equal to the semi-major axis.
- *Drag Term (Radiation Pressure Coefficient)*. It is defined as the atmospheric drag on the satellite's motion, expressed in Earth radius^{-1}.
- *Ephemeris Type*. A number used for internal analysis only, usually set to zero. It represents the orbital model used to generate the data.
- *Element Number & Check Sum*. The first three digits represent the count of the TLEs generated for this object by the US STRATCOM. The counter increases with time, up to the value 999, after then is set again to zero. The last digit is the checksum for line 1.
- *Revolution Number at Epoch & Check Sum*. It is, roughly, the number of revolutions of the objects at the specified epoch. The last digit is the checksum for line 2.

The data coming from the TLEs is the most reliable source of information that can be find in order to predict the position of an orbiting object in a given epoch. Therefore, TLEs are used worldwide to predict the pointing coordinates of the sensors used to monitor the space debris.

1.2 Space debris measurements

Space debris measurements can be performed from space (space-based measurements), as well as from the ground (ground-based measurements). Space-based measurements are only used in LEO, due to its cost, and they are mostly performed to gather information about submillimiter-sized particles in space. The majority of space-based sensors is characterized by a detection surface, namely a surface exposed to the impact of the orbital debris. The impact of the debris appears in the form of small craters which can be measured to obtain the diameter of the particles.

Ground-based measurements, generally fall into two categories: optical measurements and radar measurements. Optical measurements are often used at high orbits (MEO and GEO), rather than in LEO, in which the measurement interval is limited to a couple of hours after the sunset or before the sunrise. This is due to the fact that the object must be lit by the sunlight while in a dark background, in order to be spotted. Other than that, optical

measurements are weather-dependent, being feasible only in clear sky conditions. Radar measurements, on the other hand, can be performed in all-weather and all-day conditions. However, the available power and the operating wavelength are limiting factors for the maximum range appreciable using this type of measurements. For this reason, ground-based radar measurements are commonly used to detect and track objects in LEO. Radar for space debris monitoring and tracking have been used both in mono-static configuration, where a single antenna act, at the same time, as transmitter and receiver, and bi-static configuration, with one antenna for the transmission and a different one for the reception. Although more complicated, the bi-static configuration allows more flexibility and is capable to detect smaller objects, with respect to the mono-static configuration.

Typically, the antenna employed in both these configurations is a reflector antenna with high directivity and limited Field of View (FOV). In this case, the beam of the antenna is often controlled mechanically, and only the actual objects inside the FOV on the antenna can be detected and measured. Otherwise, radar measurements can be performed using phased array antennas, with electronically controlled beam, able to detect and measure objects from different directions. The most frequently radar modes used to detect space debris are the beam-park mode, the tracking mode and the mixed mode. The beam-park mode is used for survey sessions, in this case the antenna is maintained fixed in a given direction, waiting for the objects to cross its FOV. This procedure is mainly used to gather statistical information about number and size of the detected objects but it is less precise to retrieve orbital parameters. The tracking mode is used to follow the object for a few minutes, keeping the objects as close as possible to the center of the antenna beam. The information that can be obtained with this mode are angular direction, range, range rate of the echoes scattered from the debris. From these information it is possible to extract direction and velocity of the objects and, from them, the orbital parameters. The mixed mode, sometimes called stare-and-chase, is a combination of the two previous modes. The radar is initially in beam-park mode, but when an object crosses its FOV, the antenna starts to follow it for a few minutes, eventually returning in beam-park mode after that.

2. RADAR MEASUREMENTS

RADAR stands for RAdio Detection And Ranging, namely a distance, velocity and direction detection device that works by means of electromagnetic waves belonging to the radio waves spectrum (or microwaves) with high accuracy [8]. Radars are based essentially on the principle of echo: a transmitter radiates high power microwave signals (whether they are continuous or pulsed) searching for objects (targets) in a given area, a receiver detects the power reflected by the objects (if present) and according to the time delay, the level of power and the frequency shift of the echo is able to determine the distance (range) and the velocity (Doppler) of the object. In order to describe how a radar system works, in Fig. 2.1 the block diagram of a typical mono-static radar system is shown.

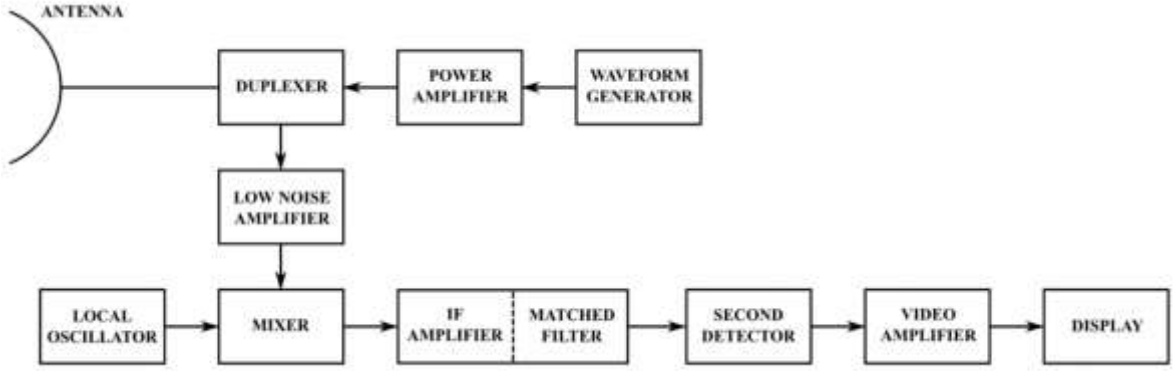

Fig. 2.1. Simple mono-static radar block diagram.

The radar signal, typically a short pulse, is created by the waveform generator, amplified and sent to the antenna. The antenna transmit the signal that propagates into di air medium, eventually intercepting a reflective object. The echo of the object is sent back to the antenna. In this particular case, the antenna is able to work both as transmitter and receiver thanks to the duplexer, which can switch between the transmitting and the receiving chain. The returning signal is further amplified by a Low Noise Amplifier (LNA) and shifted, in frequency, to the base band. This operation is known as down-conversion, and it will be discussed later in this chapter. The down-converted signal is amplified and filtered, in order to cut undesired frequency contributions. If the echo is strong enough, it can be received by a detector and visualized in a display of the measurement instrument employed. Since most of the radar used for space debris monitoring can be described using the very same block diagram reported above, it is worth describing in greater detail every single block. The transmitter section is composed by a signal generator and a power

amplifier. Common examples of power amplifiers used in radar systems are the klystron, the traveling-wave tube and the crossed-field amplifier. However, many configurations are based on power oscillator, such as the magnetron, which can deliver a lower average power, though. The waveform generator allows to choose the shape of the signal, and thus of the transmitted pulse, accordingly to the type of measurement. The most common waveform used in radar applications is the train of short pulses, but Continuous Wave (CW) and Frequency Modulated CW (FM/CW) are also used. The power budget for radars employed in the space debris monitoring can be in the order of magnitude of a megawatt, a very high power due to the weakness of the echoes scattered from the objects. The duplexer is an electronic device used to isolate the transmitting chain from the receiving chain. This device is employed only in mono-static systems, to allow the sharing of the same antenna for transmission and reception, by means of a rapid switch. In order to be sent and received, the signals must pass through an electromagnetic transducer, such as an antenna. For radar communications, the antenna configuration is usually a directive one, commonly a reflector antenna or a phased array. The narrow beam of directive antennas is preferred for its ability to concentrate the high transmitted power in a given direction. A typical Half-Power Beamwidth (HPBW) of an antenna for airborne tracking is in the order of 1 – 2 °, whereas for spaceborne radar configuration can be significantly smaller. The receiver configuration in a radar system is most likely a superheterodyne type. In these systems, the Radio Frequency (RF) signal coming from the antenna is amplified by the LNA, trying to keep the noise level as low as possible, and shifted to an Intermediate Frequency (IF) by the mixer. The IF signal need to be filtered, to cut off undesired spectral contributions and obtain the best Signal-to-Noise Ratio (SNR), and further amplified. The second detector is a diode, which extracts the modulation envelope of the IF signal, if the radar is meant to retrieve the range of the objects, or the phase if we are dealing with a Doppler radar. At this point the signal is ready to be processed and visualized.

2.1 Radar Equation

Fig. 2.2 illustrates the principle on which a pulsed radar is based, where T represents the Pulse Repetition Time (PRT), namely the time interval between one pulse and the next, t represents the pulse width and τ represents the echo's time of arrival. Since electromagnetic waves travel at the speed of light ($c = 3 \cdot 10^8$ m/s) we can find the distance D from the observer as:

$$R = \frac{c\tau}{2} \tag{1}$$

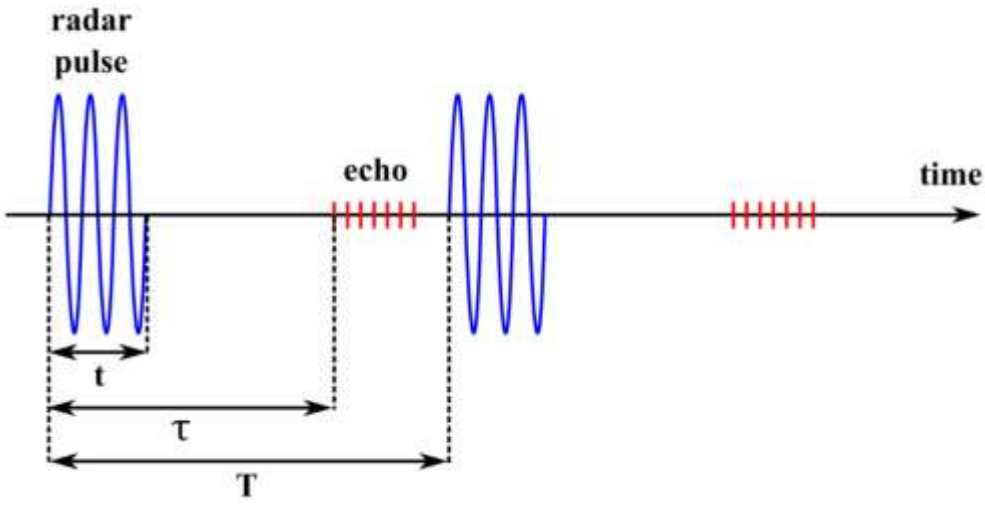

Fig. 2.2. Simple mono-static radar block diagram.

Hence, if the radar pulse is characterized by high power and short duration, the mean value of the power per time unit is much lower than the peak power. The latter relationship can be expressed using the duty cycle, defined as the ratio between the pulse duration and the PRT.

$$D(\%) = \frac{t}{T} \cdot 100 \tag{2}$$

In this way, it is possible to express the mean power as the product between the peak power and the duty cycle:

$$P_M = P_P D \tag{3}$$

As already said, radar antennas should be strongly directive, in order to concentrate the high level of power in a specified direction. The latter sentence implies that the pointing of the antenna must be very accurate. The antenna is pointed by means of azimuth and elevation coordinates. As a convention, the azimuthal angle is measured from 0° to 360° starting from the cardinal point north and moving clockwise. Whereas the elevation angle is the vertical angle between the observer (antenna) horizon and the half-line that unites the observer and the target. To clarify this point, one can refer to the image reported in Fig. 2.3.

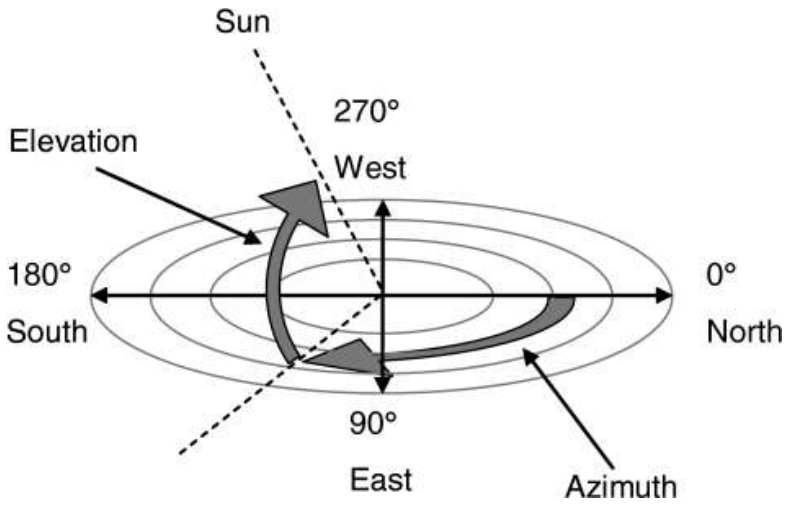

Fig. 2.3. Graphical representation of the azimuth and elevation angles.

The way a radar works can be explained using a single formula, known as the radar equation. By means of this equation it is possible to describe how the radar is capable of discriminating objects at a certain distance and which are the factors that influence this calculation. The following particular form of the radar equation is also called "transmission equation" for mono-static radar:

$$P_R = \frac{P_T G^2 \lambda^2 \sigma F^4}{(4\pi)^3 R^4} \tag{4}$$

where P_R is the received power, P_T is the transmitted power, G is the antenna gain, λ is the wavelength, σ is the target Radar Cross Section (RCS), F is the pattern propagation factor of the antenna and R is the distance between the antenna and the target, most commonly known as range. From this equation, and without further deep investigations, it is pretty clear that the transmitted power is not the only key element in the detection of the target. A preeminent role is played by the type of the antenna, by the size of the target and most of all, the received power strongly depends from the antenna-target distance. The factor F takes into account the fact that the target may be not in the center of the antenna beam (its maximum). However, this factor is often neglected in many representations of the radar equation, reasonably assuming that the target is always kept in the center of the beam. Furthermore, equation (4) represents the case of a mono-static radar, which is not the case discussed in the present dissertation. In the case of a bi-static radar configuration, where the antennas for transmission and reception are different, the radar equation can be written as:

$$P_R = \frac{P_T G_T G_R \lambda^2 \sigma}{(4\pi)^3 R_T^2 R_R^2} \tag{5}$$

where G_T is the transmitting antenna gain, G_R is the receiving antenna gain, R_T is distance between the transmitting antenna and the target (transmission range) and R_R is the distance between the receiving antenna and the target (receiving range). Starting from (5), quite a few interesting considerations can be derived. First of all, it could be very useful to know the minimum detectable power of the radar system, which is tied to the maximum range of the radar. For the sake of simplicity, it is better to propose the equations in the mono-static form. The bi-static case is analogous, with the only difference that the maximum range will be expressed in the form of a slant range, meaning the sum of the transmission and reception range. This power can be expressed as:

$$P_{R,min} = \frac{P_T G^2 \lambda^2 \sigma}{(4\pi)^3 R_{max}^4} \tag{6}$$

and, consequently, the maximum range of the radar system can be written as:

$$R_{max} = \left(\frac{P_T G^2 \lambda^2 \sigma}{(4\pi)^3 P_{R,min}} \right)^{1/4} \tag{7}$$

An alternative, and still, very used representation of the same radar equation is the evaluation in terms of SNR, which is the ratio between the received power and the system noise power.

$$SNR = P_R / P_N \tag{8}$$

At this point, a little digression is in order, to clarify the meaning of the noise power. This quantity is derived from the Johnson-Nyquist's theorem, for which if a circuit element is at a temperature of T (expressed in Kelvin), it generates an open-circuit thermal-voltage equal to:

$$V_N = \sqrt{4kTRB} \quad volts \tag{9}$$

where k is the Boltzmann's constant ($1.38054 \cdot 10^{-23}$ Ws/K), R is the resistance expressed in ohms, and B is the bandwidth of the voltage measurement expressed in hertz. The noise temperature is usually referred as "white noise", characterized by a uniform frequency specter along an infinite bandwidth. Equation (9) is, actually, an approximation, since there is no dependence on the frequency. However, it can be considered sufficiently accurate for frequencies up to 30 GHz and temperatures of at least 300 K. Now, if we connect an impedance-matched load to the open circuit described (as shown in Fig. 2.4), with $R_L = R$, the power transferred from the generator to the load is:

$$P_N = kTB_N \tag{10}$$

which is no more dependent from the resistance value.

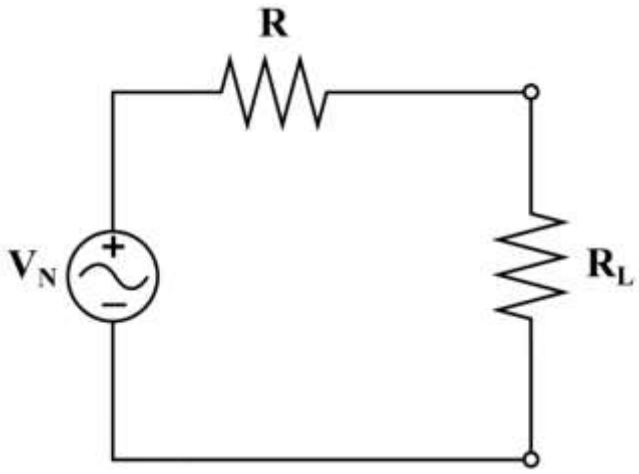

Fig. 2.4. Thermal noise circuit representation.

The latter equation is also an approximation, but, once again, can be considered adequately accurate at regular radar frequencies and temperatures. Once is clarified this concept, merging equations (8) and (10), we can obtain:

$$P_R = (SNR)kT_NB_N \tag{11}$$

where T_N is the system noise temperature. From this equation we can derive:

$$P_{R,min} = (SNR)_{min}kT_NB_N \tag{12}$$

and of course we can rewrite equation (7) as:

$$R_{max} = \left(\frac{P_T G^2 \lambda^2 \sigma}{(4\pi)^3 (SNR)_{min} k T_N B_N L} \right)^{1/4} \tag{13}$$

The quantity L represents the loss factor, namely the ratio between the transmitted power and the power delivered to the antenna. Equation (13) gives the maximum range of the radar system with respect to the minimum SNR detectable.

Two important parameters that can define the radar performance, are the range resolution, which is tied to the maximum non-ambiguous distance, and the non-ambiguous Doppler. The range resolution is the capability of the radar system to discriminate two distinct targets. The closer the targets are, the more difficult is to discriminate them, and, consequentially, the better the range resolution has to be. With reference to the schematic in Fig. 2.5, let us assume that a mono-static radar transmits a pulse that intercepts two objects.

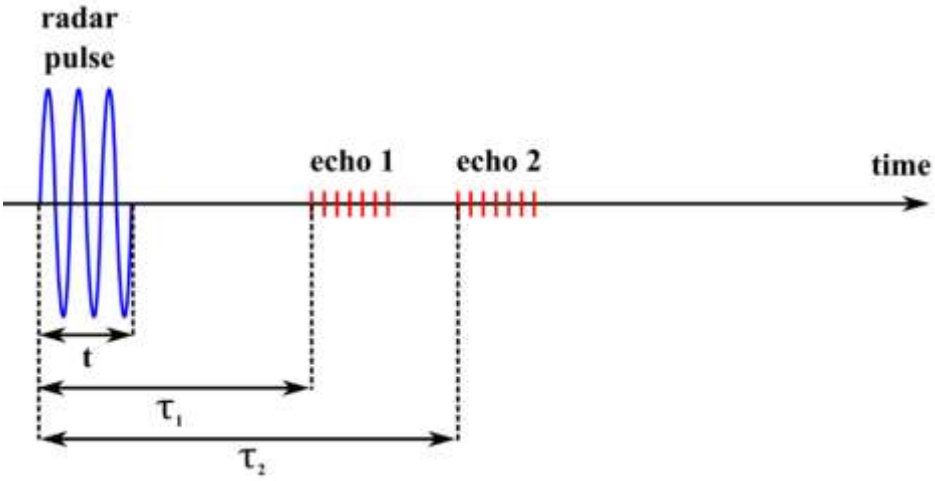

Fig. 2.5. Reception of a double echo from the same transmitted pulse.

Keeping in mind equation (1), the range of the two objects can be found as:

$$R_1 = \frac{c\tau_1}{2} \tag{14}$$

$$R_2 = \frac{c\tau_2}{2} \tag{15}$$

In order to be able to receive both echoes, the duration of the pulse must be smaller (equal in the borderline case) than the difference between the echoes' times of arrival:

$$\tau_2 - \tau_1 \geq t \tag{16}$$

This means that if we multiply by c (light speed) and divide by 2, we get:

$$\Delta R = R_2 - R_1 \geq \frac{ct}{2} = \frac{c}{2B} \tag{17}$$

where ΔR is the range resolution and B is the signal bandwidth. We can also find the maximum non-ambiguous distance as:

$$R_{n.a.} = \frac{cT}{2} = \frac{c}{2PRF} \tag{18}$$

where we defined the Pulse Repetition Frequency (PRF) as the inverse of the PRT. To conclude this paragraph, the condition of non-ambiguous Doppler is reported hereafter:

$$PRF > \Delta f = \frac{2v}{\lambda} \tag{19}$$

in which Δf is the Doppler frequency and v is the target speed.

2.2 Radar Architectures

The most commonly used radar architectures are the pulsed radar and the Continuous Wave (CW) radar. As the name suggest, the first type of radar transmits high power pulses whereas the second uses continuous signals. Pulsed radar fall into two main categories:

- Pulse Doppler (PD) radar;
- Moving Target Indication (MTI) radar.

PD radars are characterized by relatively high PRF and they are used mainly to detect moving targets in highly clutter environments. By changing the PRF of the transmission it is possible to retrieve both the range and the velocity of the target, but not at the same time. By definition, for any radar architecture it is impossible to obtain both non-ambiguous range and velocity. As a matter of fact high PRF radars are conceived to obtain the Doppler and, so, the velocity of the objects, whereas low PRF radars are meant to retrieve the range. For this reason, PD radars are mostly oriented to Doppler measurements, but

range measurements, even though not very accurate, are still possible by decreasing the PRF. It must be clear that these considerations are true for very long distance scenarios, like the space debris monitoring. In fact, for nearby objects, in airborne applications for instance, PD radar are capable of accurate range data acquisition. On the other hand, MTI radars are characterized by low PRF to avoid any type of range ambiguity. The purpose of MTI architectures is to reject radar echoes from slow-moving or fixed objects, like buildings and trees, to better focus on signals traveling back from high speed objects. This features make them the ideal system of airborne surveillance. Even if the MTI falls into the range measurement radar, it utilizes the Doppler shift of the reflected signals to discriminate moving targets from fixed ones. In the pulsed radar context, a Doppler shift is received as a change in the phase of the signal. The echoes of the signals coming from fixed objects have no phase change, whereas for moving objects the change in phase is due to the speed of the target. Table 2.1 [8] shows an overview of the characteristics of the PD and MTI radars.

Table 2.1. Summary of PD and MTI radar characteristics.

	Advantages	**Disadvantages**
MTI (low PRF)	Able to discriminate moving targets from fixed ones. No range ghosts. Reduced dynamic range requirements	Low Doppler visibility. Poor slow-moving target rejection. Cannot measure radial target velocity.
PD (medium PRF)	Good performance. Good slow-moving target rejection. Can measure radial velocity. Less range eclipsing than high PRF radars.	Range ghosts. Sidelobe clutter limits performance. High stability requirements due to range folding.
PD (high PRF)	Can be sidelobe clutter-free for some targets aspect. Single Doppler blind zone at zero velocity. Good slow-moving target rejection. Measure radial velocity.	Sidelobe clutter limits performance. Range eclipsing. Range ghosts. High stability requirements due to range folding.

CW radars cannot measure range, but the Doppler shift of the returning signal, and from this information it is possible to obtain the velocity of the object. It is worth mentioning that the latter sentence is referred to an unmodulated CW transmission. Essentially a CW transmission, in time, is a continuous sinusoidal signal with constant power. In the case of a mono-static system, the Doppler frequency can be written as:

$$\Delta f = \frac{2v_r}{\lambda} \tag{20}$$

where v_r is the radial velocity of the target with respect to the radar and λ is the wavelength. For bi-static systems, it must be taken into account the different contribution of the velocity of the object with respect to the different antenna locations. In order to obtain non-ambiguous Doppler, this relationship has to respect the condition reported in equation (19).

From the description of the radar systems above it is possible to draw an important conclusion. Pulse radars employ short high power pulses to obtain a better range resolution and retrieve the range measurement with high accuracy. CW radars, on the other hand, are meant to utilize continuous signals, that allows a more efficient use of the average power and to obtain the velocity measurement. The use of long pulses can sort the same effect. The pulse compression technique is a compromise, allows the transmission of long pulses which will have a short pulse equivalent bandwidth. They merge the high detection capability of long pulses while retaining the range resolution of the narrow ones. In this way the transmission can benefit of the advantages of the two worlds. There is no more necessity to transmit high peak power pulses, the average transmission power can be increased without increasing the PRF and, consequentially, avoiding range ambiguities. Basically, with this technique, a long coded pulse can be transformed in a narrow, or "compressed", pulse. The process of shortening the long pulse is explained in Fig. 2.6.

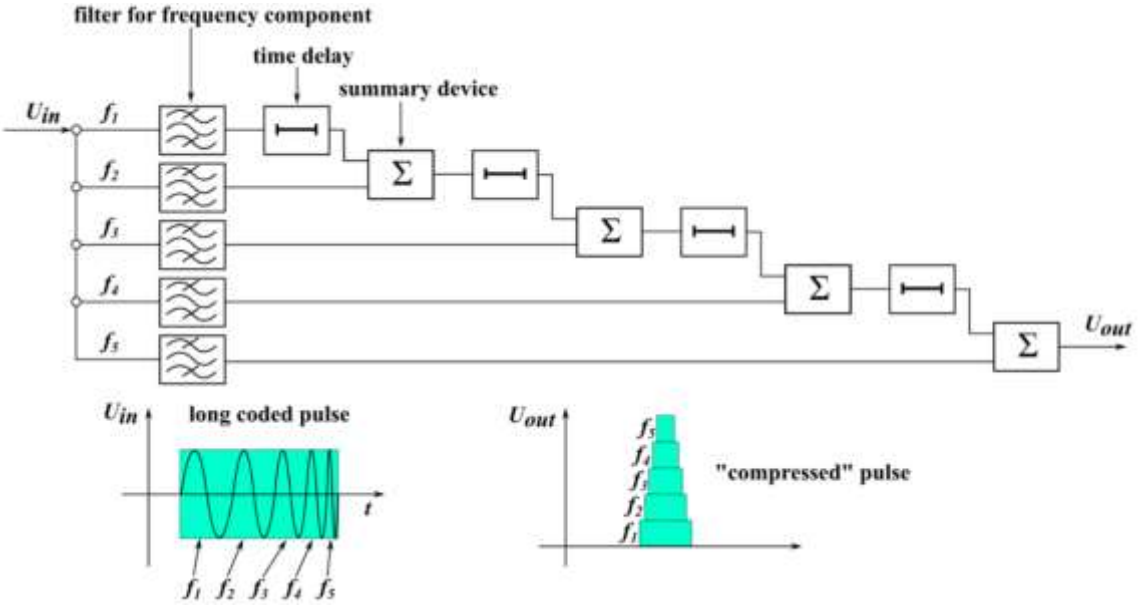

Fig. 2.6. Explanation schematic of the pulse compression technique.

From the practical standpoint, the pulse compression requires the use of a matched filter, obtained by means of an inverse Fourier transform. Among the different waveform used to achieve the pulse compression, the simplest one is, by far, the linear Frequency Modulated (FM) waveform, also known as chirp.

3. STATE OF THE ART

Radar sensors are an essential part of the worldwide SD monitoring program, i.e. Space Situational Awareness (SSA), and they are scattered all over the globe. The United States are the most exhaustive source of information about orbital debris. Thanks to the Space Surveillance Network (SSN), an extensive network of optical and radar sensors, the United States Strategic Command (USSTRATCOM) is able to hold and maintain the largest database of catalogued objects in LEO [7]. The SSN radar sensors are comprised of phased arrays, reflector antennas and multi-static fences and also other types of radar which do not fall under the canonic SSN network but are hosted by the US and could provide useful SSA data [9]. A detailed list of US SSN sensors is reported in [10]. The US Joint Space Operations Center (JSpOC) act as coordinator for the large amount of data coming from the SSN, elaborating the orbital parameters and making them available in a suitable format, i.e. Two-Line Element set (TLE) already discussed in chapter 2 [11]. After the US, Russia holds the second most important radar network for SD observation. Such a network is based, for the most part, on inactive missile warning systems, distributed across the former USSR. In fact, about half of these sensors are located outside of the actual Russian borders. Among the Russian radar network, it is worth mentioning a few of them. The two Daryal-Radar located in Pechora (Russia) and Gabala (Azerbaijan), are both phased array in a bistatic configuration, working in VHF range (150-200 MHz) capable of transmitting up to 350 MW [9], [10]. The same configuration is used by the Volga-type radar in Baranivichy (Belarus) operating at 3 GHz and by the Don-2N radar (also known as Pill Box) located in Moscow [9]. Unfortunately, there is very limited information about the radar sensors owned by the People's Republic of China. From the poor data found in the web, it can be stated that the Chinese Space Surveillance System (CSSS) radar sensors are for the majority phased arrays and some of them might be located in Xuanhua, Zhangjiakou (Hebei province) and Xinjiang [10].

Considering the relevance of the SD problem, also Europe has started a space surveillance program. Following the steps of the USSTRATCOM, the European Space Agency (ESA) created the Space Surveillance and Tracking segment (SST) within the SSA European program, focused on the creation of its own catalogue of orbiting objects. Europe can count on a large network of radar sensors, likewise USA and Russia, within the member states. The European Incoherent Scatter Scientific Association (EISCAT), for instance, is a radar system composed by three separate sites [12]: the monostatic VHF radar, located near Tromsø (Norway), which operates at 224 MHz; the monostatic double antenna EISCAT

Svalbard radar, located in Longyearbyen (Svalbard), which operates at 500 MHz; and the tristatic UHF EISCAT radar operating at 930 MHz, with transmission site located in Tromsø and receiving sites located also in Tromsø, Kiruna (Sweden) and Sodankylä (Finland). All the EISCAT transmitters are able to supply a peak power in the order of magnitude of Megawatts with a duty cycle of about 10-20 %. Other important radar facilities for SD observations can be found in Germany, France, Spain and Italy. Germany has at its disposal a powerful bistatic radar consisting of the FGAN Tracking and Imaging Radar (TIRA), located in Wachtberg, near Bonn, as a transmitter and the Max-Planck-Institute 100-m Effelsberg Radio Telescope as a receiver. In this configuration, the system can transmit 1-2 MW peak power pulses in L-Band, allowing the detection of objects with size down to 1 cm [13]. In the next future, the German Space Administration (DLR) will be able to include the so-called German Experimental Surveillance and Tracking Radar (GESTRA) among the active radar sensors, a close-monostatic pulsed phased array working in L-band (1280-1400 MHz) able to perform digital beamforming [14]. On the French side, remarkable radar facilities for SD are the Grand Réseau Adapté à la Veille Spatiale (GRAVES), a military continuous wave (CW) bistatic phased array radar operating at 143.05 MHz, located in Dijon [15] and the ARMOR, the most powerful of the DGA radar, located on the missile range instrumentation ship Monge, a monopulse C-band system with 1 MW peak power [16]. The Spanish Space Surveillance and Tracking (S3T) system is currently equipped with two radar within its S3T Sensor Network (S3TSN): the Monostatic Space Surveillance Radar (MSSR), a close-monostatic L-band radar, located in the Santorcaz military naval base and the new S3T Surveillance Radar (S3TSR) [17]. As for the United Kingdoms (UK), in 2010, the Chilbolton radar, a fully steerable 25-m dish antenna working in S-band (3 GHz) with a peak power of 700 kW and located near Winchester (Hampshire), was converted for SST purposes in the Chilbolton Advanced Satellite Tracking Radar (CASTR). These features allow the CASTR to detect objects with Radar Cross Section (RCS) greater than 0.5 m^2 beyond 2100 km efficiently [18].

In Italy, the main radar sensor completely dedicated to the SD observations is the Bistatic Radar for LEO Survey (BIRALES). The transmitting antenna of this system is the Radio Frequency Transmitter (TRF), which will be discussed in detail in the next section, being the same transmitter used in this work. The receiver is the Northern Cross Radio Telescope, located in Medicina Radio Astronomical Station, near Bologna, in Northern Italy. The Northern Cross is composed by two branches, the East/West (E/W) and the North/South (N/S). A subsystem of 16 parabolic cylindrical antennas of the N/S branch (named BEST-2)

act as a receiver for the BIRALES. In its actual configuration, BIRALES is capable of performing range measurements and detecting objects as small as 0.01 m^2 [19].

4. THE SARDINIA RADIO TELESCOPE

The Sardinia Radio Telescope (SRT) is located in Pranu de Sanguini, near San Basilio, at about 35 km north from Cagliari, in Sardinia (Italy). The first work on the SRT started in 2002, but the radio telescope saw its first light in August 2012. The primary mirror of the SRT is a 64-meter diameter dish which makes the antenna the largest radio telescope in Italy and one of the largest in the whole Europe. The SRT is capable of observing the sky in the frequency range from 300 MHz to 100 GHz and beyond [20], its main purpose is the scientific research in the radio-astronomical field but a fraction of its employment is devoted to the spacecraft monitoring (such as space debris). Together with the radio telescopes located in Noto and Medicina, the SRT constitute the Italian VLBI (Very Long Baseline Interferometer) network.

4.1 Structure

The Sardinia Radio Telescope is an impressive structure, the height is about 70 m and its weight around 3000 tons. For these reasons the telescope is installed on reinforced concrete foundations with a diameter of 40 m and a depth of 6.5 m. The center of the foundations is provided with an octagonal housing for cable routing and bearing installation that allow azimuth movements of the SRT [21]. Figure 4.1 offers a front view of the SRT structure.

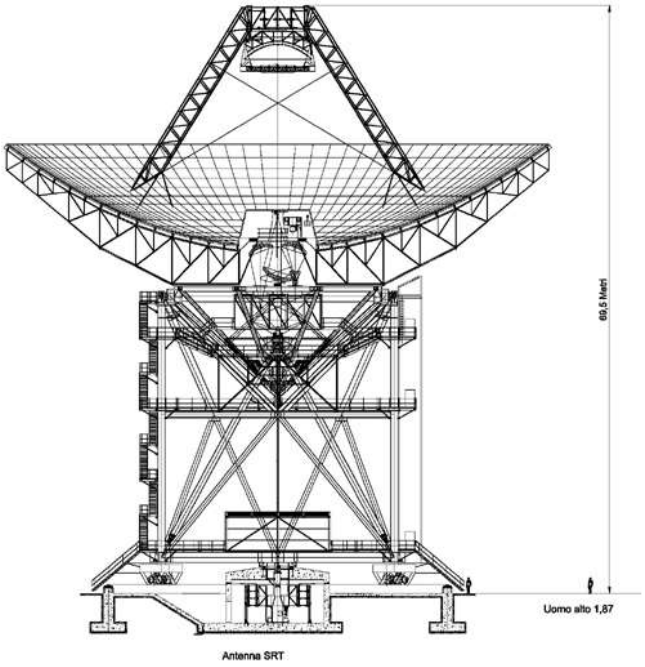

Fig. 4.1. Front view of the SRT structure.

The azimuth rotation is possible thanks to a rail built on the foundations. Such a rail has the same diameter of the foundations and it is coupled with them by means of an interface made of a specific concrete reinforced with thin steel rings. The rotation system can count on a total of 16 wheels (4 of them are drive wheels) permitting an angular excursion of ± 270° at a maximum speed of 0.85°/sec. The wheel for elevation pointing is made up of a conical truss frame behind the primary mirror. In this case the angular excursion is from 5° to 90° at a maximum speed of 0.5°/sec. The primary mirror, 64 m in diameter, consist of 1008 aluminum panels supported by a rear truss frame. The housing for the instrumentation related to the Gregorian focus is located at the top of the primary mirror. The base configuration of the antenna is the Gregorian shaped with a "quasi-parabolic" primary mirror and a "quasi-elliptical" secondary mirror. This configuration guarantee a better illumination of the Gregorian focus, with respect to a standard configuration, creating a zero field zone in the central region of the primary mirror which is obscured by the blockage of the secondary mirror (see Fig. 4.2). In this way the field is redistributed in the non-obscured zone, decreasing the standing waves between the feeds at the secondary focus and the sub-reflector. In addition, the shaped configuration allows to under illuminate the sub-reflector edge, reducing the spill-over.

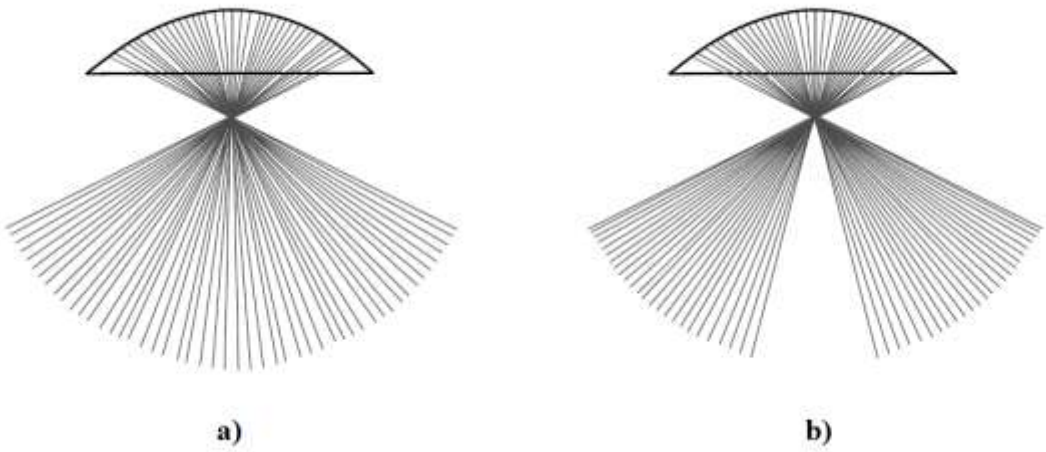

Fig. 4.2. Confrontation between classical and shaped illumination.

This choice, resulting from the combination of the curvature of the primary and secondary mirror, allows the optimization of observations in Gregorian focus and Beam Wave Guide (BWG).

One of the most innovative and recognizable features of the SRT is the active surface: a total of 1116 electromechanical actuators are currently installed in the back of the primary reflector. The actuators, acting on singular panels, help to compensate every possible source of surface deformation, in particular:

- Gravitational effects, due to the weight of the antenna itself;
- Pressure of the wind;
- Thermal gradients;

The trussing of the primary mirror supports the secondary one, located at a distance of about 24 m, by means of a quadrupode. The "quasi-elliptical" 8-m diameter secondary mirror is composed by 49 panels supported by a rear truss frame. A primary focus positioner (PFP) allows positioning different feeds at the primary focus. The PFP is anchored to the truss behind the mirror. The overall blockage on the geometric area of the reflector, by the sub-reflector, the quadrupode, the cables and the positioner is of about 6%. The correct orientation of the sub-reflector is ensured by 6 electromechanical actuators, 3 along the z-axis (the same axis of the primary reflector), 1 along x-axis (parallel to the elevation axis) and 2 along the y-axis (perpendicular to x-axis). One important parameter is the pointing error accuracy, which is tied to the frequency and, thus, to the antenna beam. The higher the frequency, the smaller the beam and the better the accuracy should be. The pointing error is expressed as it follows:

$$\delta_P \leq \frac{HPBW}{10} \tag{21}$$

where HPBW stands for Half-Power Beamwidth, the width of the beam corresponding to –3 dB (half of the total power) in the main lobe. The causes for the pointing error are:

- Systematic errors of the mechanical and electromagnetic alignment of the structural parts and the feeds;
- Non-systematic errors, due to the pressure of the wind and the thermal gradients.

Typically, systematic errors have high values, in the order of few arc minutes. However such errors can be evaluated by means of astronomical observation campaigns of reference radio sources, and, consequentially, removed. As for non-systematic errors, active error correction techniques are needed in order to remove them. Table 4.1 offers a recap of the observational conditions of the SRT, divided in accurate, normal and extreme. The

observations at high frequencies (within the range 22-100 GHz) are possible only during accurate and normal conditions.

4.2 Optics

The design of SRT optics has been made in an attempt to obtain the largest number of focal position in the available space. The availability of several operating foci allows greater freedom in the selection of the receivers to be used.

Table 4.1. Summary of the observational conditions of the SRT.

	Parameters	**Specifications**
Accuracy	Wind	< 15 km/h
	Sun	Absent
	Rainfall	Absent
	Temperature	-10 – 30 °C
	Thermal Excursion	< 3 °C/h
	Humidity	< 85%
Normal	Wind	< 40 km/h
	Sun	Clear sky
	Rainfall	Absent
	Temperature	-10 – 40 °C
	Thermal Excursion	< 10 °C/h
	Humidity	< 90%
Extreme	Wind	< 80 km/h
	Sun	Clear sky
	Rainfall	< 1 cm/h
	Temperature	-10 – 50 °C
	Thermal Excursion	Any
	Humidity	< 100%

There are three main operative areas, for a total of 6 focal positions. With reference to the schematic of the focal positions of the SRT reported in Fig. 4.3, the focal positions are:

- Primary focus (F_1);
- Gregorian focus (F_2);
- Beam Wave Guide (2 x F_3, 2 x F_4).

The Gregorian configuration allows the use of the parabolic mirror focus without the necessity to move the secondary mirror. In order to use the primary focus, the antenna

design includes the PFP, that supports different receivers. The positioner consists of a structure rotating around one of the transverse axes of the sub-reflector. Once extended, the latter can place the feeds in front of the secondary reflector, by the primary focus. In this way, by means of the translation movement along the same rotation axis, it is possible to choose the receiver suitable for the observation, and, by means of the movement along the z-axis, it is possible to hold the optical focal position.

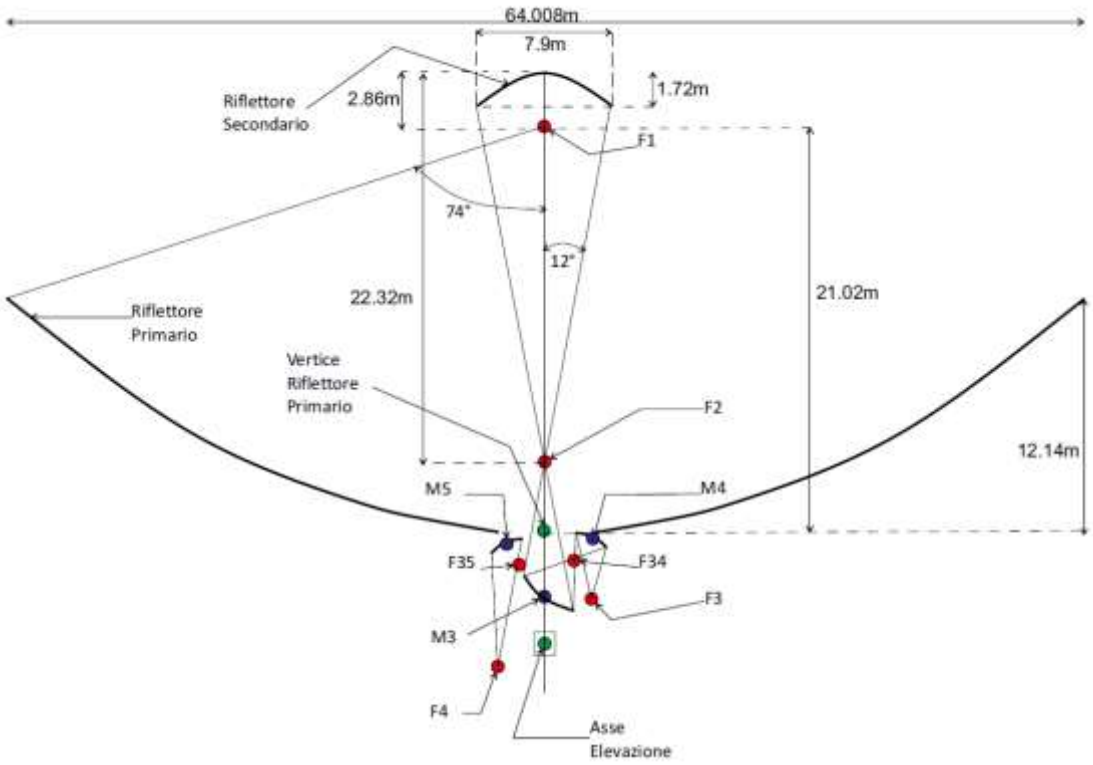

Fig. 4.3. Optics configuration and foci location of the SRT.

The focal length of the primary mirror is about 21 meters, resulting in a ratio $F_1/D \approx 0.33$. The suitable operating frequencies range for the receivers at focal position are in the range 0.3-22 GHz. Moreover, the simultaneous usage of the couple of frequencies 2 and 8 GHz is possible thanks to a coaxial receiver, employed primarily for geodynamic purposes.

The Gregorian focus is located 3.5 m above the reflector vertex. By this point, an observational structure provided with an off-axis cylindrical rotating system, capable of hosting up to 8 receiving systems, is present. It is possible to select the feed to be placed in correspondence of the focal area through the rotation around the cylinder axis. The secondary mirror, thanks to its elliptical geometry, produces a magnification i_2 that depends on the ratio between its focal length and its distance from the first focus (about 20

meters and 3 meters respectively, in this case). The complete focal calculation is herein reported:

$$i_2 = \frac{20.32}{2.85} \approx 7.13 \tag{21}$$

$$F_2 = i_2 \cdot F_1 \approx 149.87\ [m] \tag{22}$$

resulting in a ratio $F_2/D \approx 2.34$. The operating frequencies for this focal position range from 7.5 to 100 GHz.

The BWG foci are located beneath the primary reflector vertex. The housing for these foci, as well as for the Gregorian focus, is a three-floor structure. The top floor of this structure host the instrumentation for the Gregorian focus observations. The lower floors host a combination of 5 "quasi-elliptical" mirrors, a mobile one, in the central position and the others fixed and divided in couples. The central mobile mirror, called M_3 and facing upwards, receive the beam directly from the Gregorian focus, and has a diameter of about 4 meters. The four fixed mirrors are labeled M_4 (A & B), with a diameter of 3 m, located above M_3 on the right side, and receiving its reflected beam, and M_5 (A & B), also with a diameter of 3 m, located above M_3 on the left side, and receiving its reflected beam. Although the elliptical mirrors have similar size, they have different radii of curvature and eccentricity. In this way they can offer different focal positions, a longer one for the M5 couple and a shorter one for the M_4 couple. In order to calculate the focal positions for each couple, it is necessary to find the magnification of M_3 and then the magnification of the next mirror depending on the couple, M_4 and M_5 respectively. In formulas, for the M_4 mirror (focal length 3.6 m) we can translate this in:

$$i_3 = \frac{2.4}{7} \approx 0.34 \tag{23}$$

$$i_4 = \frac{3.6}{2.1} \approx 1.71 \tag{24}$$

$$i_{tot} = i_2 \cdot i_3 \cdot i_4 \approx 4.19 \tag{25}$$

$$F_3 = i_{tot} \cdot F_1 \approx 183.91\ [m] \tag{26}$$

resulting in a ratio $F_3/D \approx 1.38$.

Whereas for the M5 mirror (focal length 7 m) we have:

$$i_5 = \frac{7}{2} \approx 3.5 \tag{27}$$

$$i_{tot} = i_2 \cdot i_3 \cdot i_5 \approx 8.56 \tag{28}$$

$$F_4 = i_{tot} \cdot F_1 \approx 179.87\ [m] \tag{29}$$

resulting in a ratio $F_4/D \approx 2.81$. However the overall accuracy of the BWG, primary and secondary mirrors allow the use of the BWG foci up to 32 GHz. A summary of the focal position of the SRT is reported in table 4.2.

Table 4.2. Summary of the observational conditions of the SRT.

Focus	Min Frequency	Max Frequency	F/D
F_1	0.3 GHz	22 GHz	0.33
F_2	7.5 GHz	100 GHz	2.34
F_3	1.4 GHz	32 GHz	1.38
F_4	1.4 GHz	32 GHz	2.81

4.3 Front-end

The SRT is designed to continuously cover the frequency range 0.3-100 GHz. All the receivers installed on the SRT (except the P-band) are super-heterodyne type, allowing the transformation of a high frequency signal to an intermediate frequency signal (IF), by means of a mixer and a local oscillator. All the receivers are cryogenically cooled to ≈ 20 K by a closed-cycle cooling system. The lower operating bandwidth of the SRT (0.3-3 GHz) is polluted by many radio frequency interferences (RFIs), and many filtering stages are present in the receiving chains within this interval, as a result. For each operating frequency, a total of 4 instantaneous IF bandwidth are available: 150 – 450 – 1000 – 2100 MHz.

The receivers installed on the Gregorian or BWG foci use a double down-conversion. Fig. 4.4 shows a general schematic of the front-end chain. The feed is usually a corrugated

horn that couples the incoming electromagnetic radiation propagating in free space from the antenna to the transmission line. The directional coupler injects a signal for the calibration of the receiving chain in front of a polarizer. The polarizer converts two orthogonal linear polarizations in right-handed and left-handed circular polarization. This is achieved by phase shifting 90° one polarization signal with respect to the other. The Ortho-Mode Transducer (OMT) separates the two polarization channels, which are the amplified by a Low Noise Amplifiers (LNA). From this point the signals are, eventually, converted and sent to the back-end.

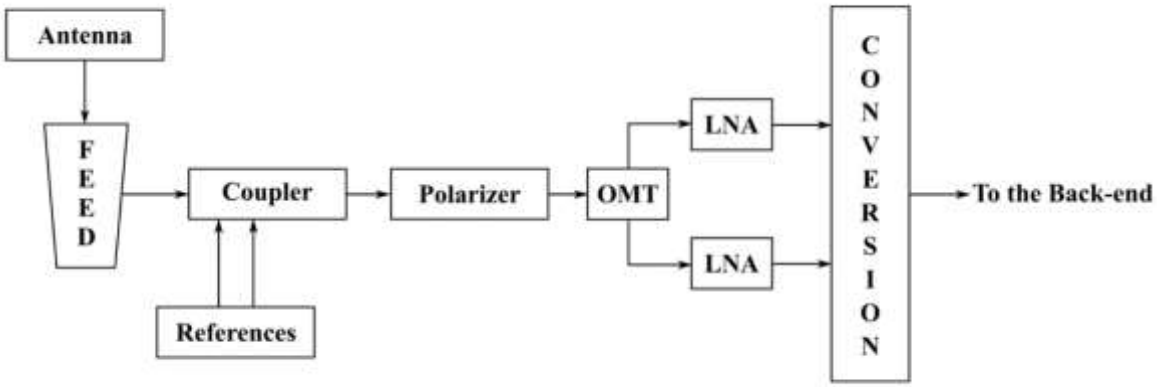

Fig. 4.4. SRT front-end chain schematic. The portion between the antenna and the conversion is usually referred to as "dewar system".

In table 4.3, the edge-taper level for the feeds are reported.

Table 4.3. Taper levels for the SRT feeds.

	Taper Level (dB)	**Taper Angle (°)**
Primary focus feeds	12-15	74.5
Gregorian focus feeds	9-12	12.0
BWG foci feeds	9-12	20.0

The characteristics of the feeds and the receivers currently available for the SRT are reported, in detail, in table 4.4.

In general, the connections between the foci of the SRT regards three different types of signal:

- Local Oscillator (LO); in order to reduce the cost of the design and the construction of a high number of separate super-heterodyne receivers, completely independent, a

very common solution involves the sharing of some LOs (at least one for one of the two conversions, for instance). In this way, a single LO can serve multiple receivers, through a signal distribution system.

- IF; the RF signal coming from the antenna have to be down-converted and sent to the back-end using the same analog fiber optic links which are shared by all the receivers
- Reference; the reference signals used for phase-locking the receivers to a common maser source located near the telescope.

All the signals are transported through coaxial cables connections and optical links that connect the antenna to the control and back-end rooms.

Table 4.4. Parameters of the SRT receivers. The colors show the location of the receiver: red for the primary focus, green for the Gregorian focus and blue for the BWG foci.

Band	**f0 (GHZ)**	**λ (cm)**	**Receiver N.**	**f_{min} (GHz)**	**f_{max} (GHz)**	**$\Delta f/f_c$ (%)**	**Receiver Bandwidth (MHz)**	**Noise Temperature (K)**	**Config.**
P	0.3	90	1P	0.305	0.410	12	2x110	30	1.5 GHz
L	0.6	50	1P	0.58	0.62	7	2x40	25	-
L	1	30	1P	0.70	1.30	60	2x600	-	-
L	1.5	18-21	2P	1.30	1.80	32	2x500	5	0.3 GHz
S	2	13	2P	2.20	2.36	7	2x160	-	8 GHz coax
S	3	10	3P	2.36	3.22	27	2x860	-	-
S	4	7.5	3P	3.22	4.30	32	2x1080	-	-
C	5	6	1B	4.30	5.6	32	2x1500	15	Monofeed
C	7	5	2B	5.70	7.70	30	2x2000	15	Monofeed
X	8	3.6	2P	8.18	8.98	9	2x800	-	2 GHz coax
X	9	3.3	1G	7.50	10.40	32	2x2000	10	-
Ku	13	2.3	2G	10.30	14.40	33	2x2000	14	-
Ku	17	1.8	3G	14.40	19.90	32	2x2000	18	-
K	23	1.3	4G	19.00	26.50	33	2x2000	21	Multifeed (7 elements)
Ka	32	0.9	5G	26.00	36.00	32	2x2000	25	-
Q	43	0.7	6G	35.00	50.00	31	2x2000	40	-
E	86	0.4	7G	70.00	90.00	25	2x2000	90	-

W	100	0.3	8G	90.00	115.00	25	2x2000	100	-

The receivers installed in the Gregorian and BWG foci employ the same two LOs (one for each channel) located in the Gregorian focus, using distribution systems named OLD. The disequalization resulting from the use of coaxial cables over long distances is compensated by using specially designed amplifiers (known as AmpEq). The reference signals are necessary to the calibration of the receivers, and, once again, they are distributed by means of coaxial cables.

4.4 Efficiency and System Temperature

Being the SRT an instrument mainly employed for radio astronomy purposes, a very common representation of the antenna's gain is the following:

$$G = 10^{-26}\frac{m\eta_a A_g}{k_B}\left[\frac{K}{Jy}\right] \tag{30}$$

where m accounts for a completely non-polarized radiation and is equal to 0.5, A_g is the geometric area of the antenna, k_B is the Boltzmann's constant and η_a is the antenna efficiency. G is expressed in Kelvin per Jansky, where the Jansky is 10^{-26} W/m^2·Hz in the International System. The latter term takes into account every possible degradation factor of the received signal that could mostly influence the antenna's overall gain. These contributions are also in the form of an efficiency factor:

- *Blockage efficiency* ($\eta_{Blockage} \approx [1 - A_{Blocked}/A_{Total}]^2 = 0.88$), due to the blockage of the field from the sub-reflector and the supporting structure.
- *Surface efficiency* ($\eta_{Surface} \approx e^{-\left(\frac{4\pi\delta}{\lambda}\right)^2} = 1 \div 0.35$), the worst case is for the highest operation frequency (100 GHz), as for the shorter wavelength. In fact, the efficiency is determined by manufacturing errors of the panels and to their misalignment. The deformation of the reflecting surfaces, the pressure of the wind, the gravitational effects and the dilatation owed to the thermal gradients contribute to decrease the surface efficiency. A metrology system is under development to reduce the RMS of the surfaces to below 150 μm (λ/20 at 100 GHz) and allow observations at highest frequencies. As already said, to counterbalance these effects the antenna is provided with an active surface system.

- *Phase efficiency* ($\eta_{Phase} \approx 0.99$), also known as de-focalization efficiency, it is tied to the lateral (axial) shift of the feed from the focus.
- *Diffraction efficiency* ($\eta_{Diffraction} \approx 0.98 \div 0.86$), that takes into account the losses due to the diffraction on the antenna edges.
- *Illumination efficiency* ($\eta_{Illumination} \approx 0.9 \div 0.76$), takes into account the amplitude and phase distribution unevenness in the antenna's aperture.
- *Cross polarization efficiency* ($\eta_{CrossPol} \approx 1$), takes into account the portion of the power radiated with an orthogonal polarization with respect to the nominal polarization of the radiation received by the antenna.
- *Spill-over efficiency* ($\eta_{SpillOver}$), is the percentage of power radiated by the feed that is intercepted by the reflectors, the rest of the power being radiated outside the reflectors edges; maximizing this term requires to decrease the aperture efficiency. Therefore an optimum is usually adopted in radio-astronomy applications with tapered illumination (a Gaussian profile), such that the feed's beam is more intense in the center and attenuated at the edges.
- *Loss efficiency* ($\eta_{Loss} \approx 0.95$), takes into account the attenuation of the signal before the LNA stage.
- *Return loss efficiency* ($\eta_{ReturnLoss} \approx 0.98$), takes into account the losses due to the reflection of the feed.

The overall efficiency is the product of all these terms.

An important parameter for a radio telescope is the sensitivity, namely the indication of the minimum flux measurable by the system:

$$\Delta S = \frac{\alpha T_{sys}}{G\sqrt{\Delta f \tau n N_{IF}}} \tag{31}$$

where α is a coefficient (≤ 1), T_{sys} is the system temperature, G is the gain expressed in K/Jy, Δf is the observation bandwidth, τ is the integration time expressed in seconds, n is the number of observations and N_{IF} is the number of available channels. In the table 4.5, the system temperature and the sensitivity of the SRT, for various frequencies, are reported. These values were evaluated for an elevation angle of 45°, which represents an optimal configuration for the antenna, since the deformation due to the gravitational effects is lower, as the antenna was aligned at that angle. Thereby, it might change as a function of

the elevation angle, until a suitable metrology system will be in place to provide optimum elevation-independent performance.

Table 4.5. System temperature, sensitivity and gain of the SRT at various frequencies. The colors show the location of the receiver: red for the primary focus, green for the Gregorian focus and blue for the BWG foci.

f0 (GHZ)	Receiver Temp. (K)	Atmosphere Temp. (K)	Soil Temp. (K)	System Temp. (K)	η_a (%)	Gain (dBi)	Bandwidth (MHz)	ΔS (myl$\sqrt{s}$)
0.3	30	16	6	52	58.7	58.7	2x110	5.1
0.6	25	-	-	-	-	-	2x40	-
1		5	8	-	-	-	2x600	-
1.5	5	5	10	20	59.4	57.5	2x500	0.9
2	-	5	5	-	-	-	2x160	-
3	-	5	5	-	-	-	2x860	-
4	-	5	5	-	-	-	2x1080	-
5	15	5	-	20	57.7	67.9	2x1500	0.5
7	15	6	-	21	57.7	70.8	2x2000	0.5
8	-	6	7	-	-	-	2x800	-
9	10	6	-	16	60.8	73.3	2x2000	0.4
13	14	15	-	29	60	76.4	2x2000	0.6
17	18	30	-	48	57	78.3	2x2000	1.1
23	21	60	-	81	56.1	81	2x2000	2
32	25	20	-	45	54.5	84.1	2x2000	1.1
43	40	20	-	60	52.5	86.1	2x2000	1.5
86	90	80	-	170	39.7	90.9	2x2000	5.8
100	100	80	-	180	34.7	91.7	2x2000	7

4.5 Back-end

The back-end is intended as the set of components that allow the processing of the signal coming from the front-end. At the moment the available back-end at the SRT are:

- The Total Power (TP);
- XARCOS;
- The Digital Base Band Converter (DBBC);
- The Pulsar Digital Filter Bank (DFB);
- The Sardinia ROACH2-based Digital Architecture for Radio Astronomy (SARDARA).

The TP platform was developed by the Institute of Radio Astronomy (IRA) that can work in two different modes: the focus selector mode (see Fig. 4.5) and the continuum back-end mode (see Fig. 4.6).

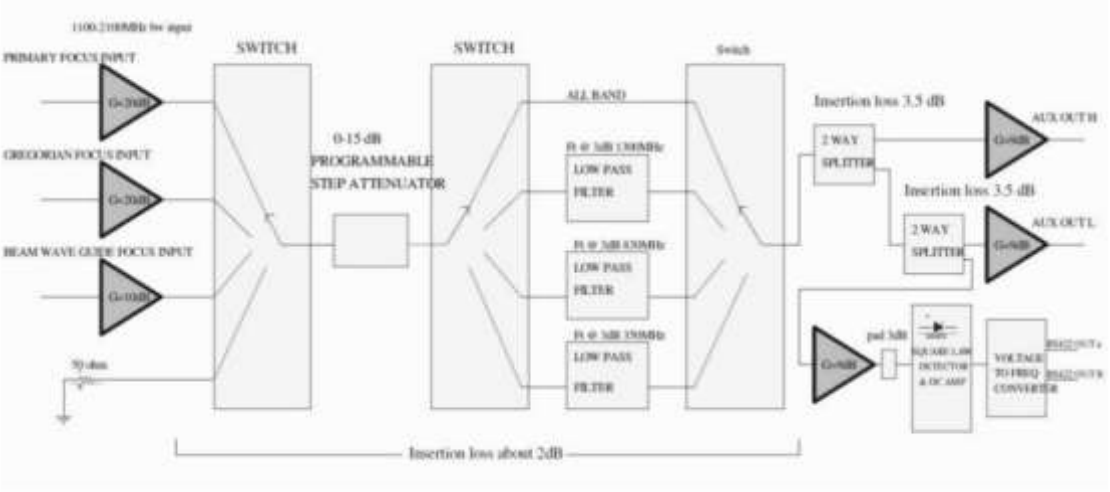

Fig. 4.5. Schematic of the Focus Selector.

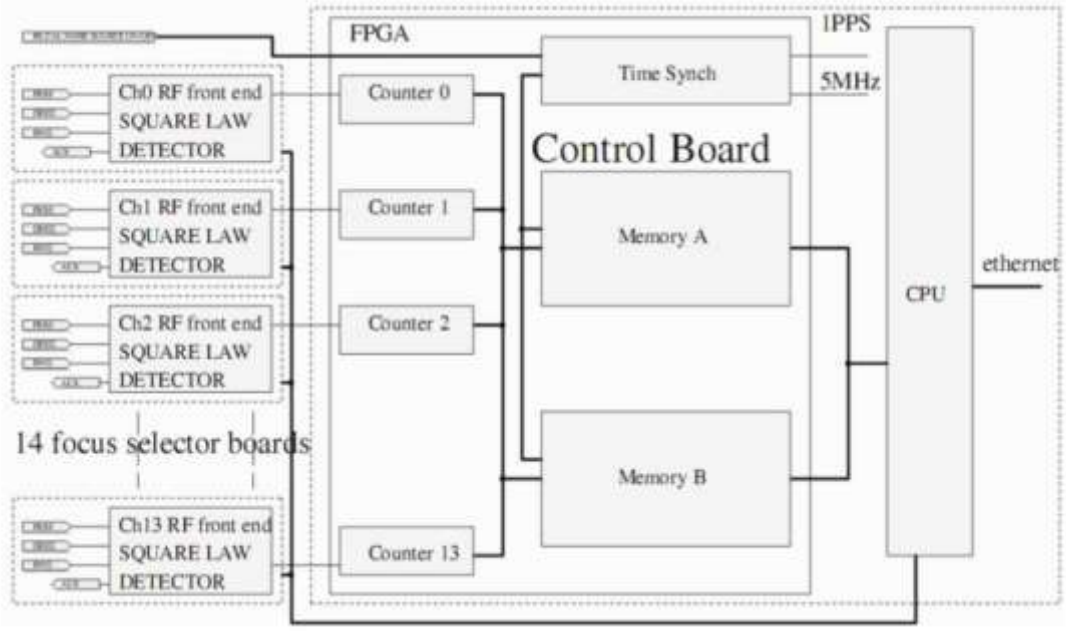

Fig. 4.6. Schematic of the Total Power.

The TP consist of 14 identical boards, each one manages the Intermediate Frequency signals coming from the three SRT foci. The signal selected by the TP is attenuated (in a range of 0-15 dB) and filtered with one of the following LPF: 100-350 MHz, 100-830 MHz, 100-1300 MHz, and 100-2100 MHz. Three copies of the signal are generated to be processed by the others SRT back-end (described below in this section) and one copy is

sent to the TP itself. The signals are then sent to square law detectors and converted in digital format. The back-end is integrated in the so-called ACS (ALMA Common Software)-based Control Software, common to all the Italian Radio Telescopes. It is important to notice that at the moment, the TP is the only back-end capable of performing On-The-Fly (OTF) mapping for the multi-feed K-band receiver.

XARCOS is a spectral polarimeter developed by the Astrophysical Observatory of Arcetri (see Fig. 4.7) containing 40 Field Programmable Gate Arrays (FPGAs) and capable of processing up to 16 signals with 125 MHz bandwidth, giving total power a spectral-polarimetric information. The signal from the front-end is amplified in the first stage of the back-end, filtered with BPFs (125-250 MHz), and converted by means of two ADC boards. The real signals are then converted to complex ones and sent to the FFT boars. For each IF, different values of the input bandwidth can be selected: 25 MHz, 62.5 MHz, 31.25 MHz, 15.625 MHz, 7.8125 MHz, 3.90625 MHz, 1.953125 MHz, 0.9765625 MHz and, finally, 0.48828125 MHz. The FFT spectral-polarimeter provides both auto- and cross-correlation products of the left and right circular polarizations. These signals are later integrated for a programmable time, multiple of 10 seconds.

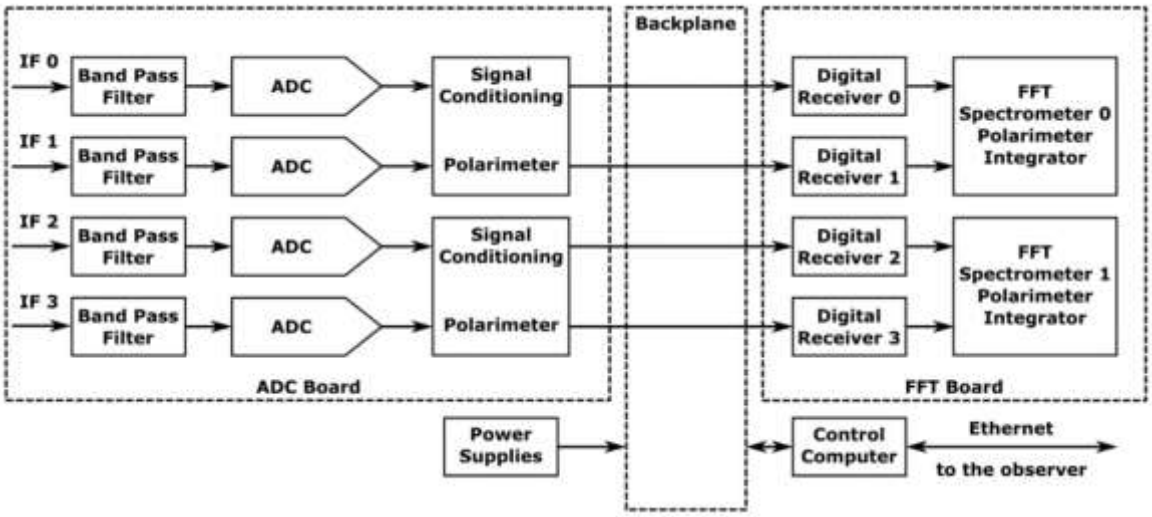

Fig. 4.7. Simplified schematic of the XARCOS with only 4 inputs.

The DBBC is a project developed by the IRA of Noto and consists of a reconfigurable modular data acquisition platform for radio astronomical applications; Figure 4.8 shows a block diagram of the DBBC. It is mainly used as a VLBI (Very Long Baseline Interferometry) machine: almost all the stations of the EVN (European VLBI Network) employ a DBBC for VLBI observations. The DBBC has a flexible architecture with more FPGA-based boards that can be stacked together. One of the strengths of the DBBC is that

is a complete platform: indeed, it contains a control personal computer, a synthesizer, a digital-to-analog board and, more generally, all that is necessary to make it an independent machine.

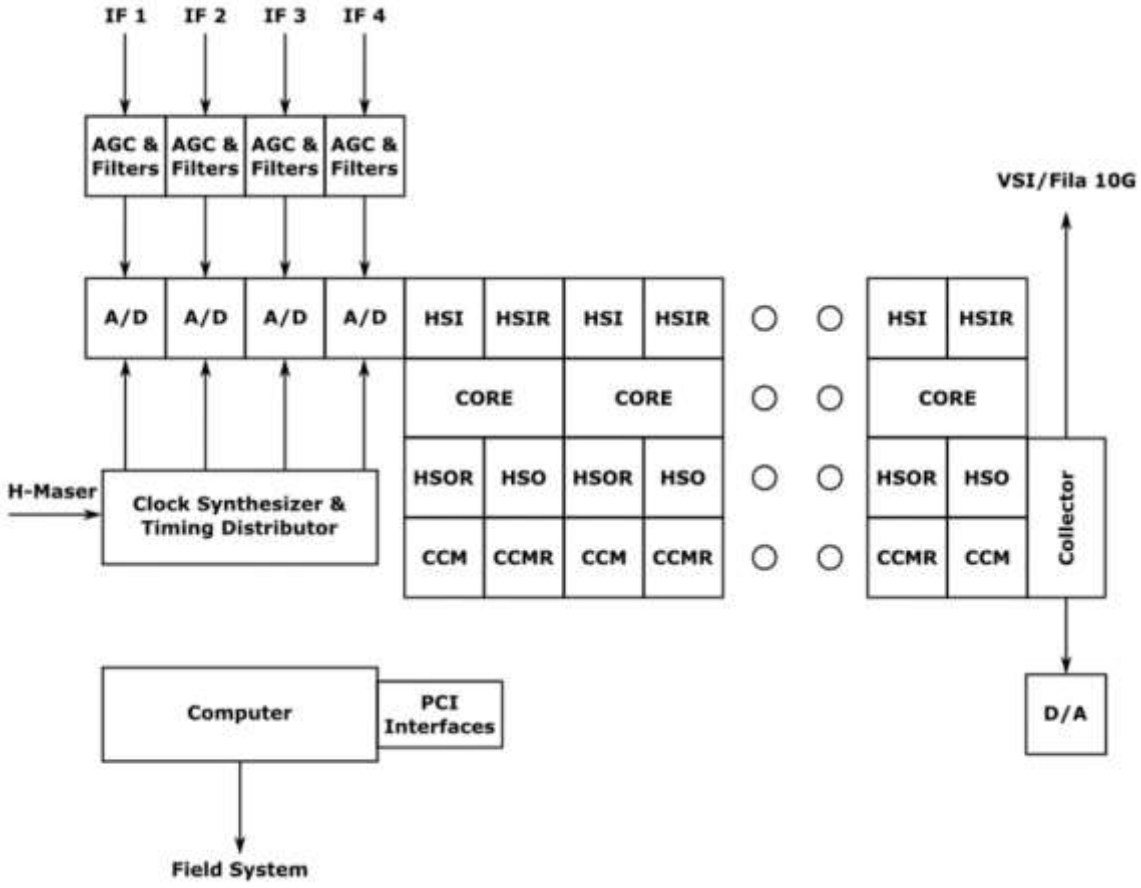

Fig. 4.8. DBBC architecture.

The DFB is a digital back-end developed by CSIRO-ATNF (Australia Telescope Natural Facility) for continuum and spectropolarimetric observations. The system is based on four 2048 MS/s 8-bit samplers to detect both polarizations of two frequency bands with a bandwidth of up to 1024 MHz. It provides full Stokes information of two receivers simultaneously. The spectra are computed by FPGAs with polyphase filters which perform an isolation between neighboring channels that are higher than 60 dB. This prevents even strong in-band RFI from contaminating the other detected channels during an observation. A full set of configurations for pulsar and spectropolarimetric observations is available, although, at SRT it is currently used only for pulsar observations.

SARDARA is the acronym for “Sardinia Roach2-based Digital Architecture for Radio Astronomy”. SRT is equipped with a variety of digital back-ends that are applicable to a significant breadth of radio astronomical studies. However, they each present strengths and weaknesses: the Total Power backend is the only back-end capable of providing the entire

bandwidth (2.1 GHz) and all 14 IFs, but can be used solely for continuum observations; XARCOS can act as a full-Stokes spectrometer, but 125 MHz - reduced to half because of its far from optimal antialiasing filters - is the widest available bandwidth; the DFB can be used as a spectro-polarimeter as well and with a larger instantaneous bandwidth (1 GHz) than XARCOS, but the system is equipped with only 4 ADCs. As a consequence, we need an infrastructure that can overcome the aforementioned drawbacks. In particular, a possible optimal solution for SRT should provide up to 14 IFs, a bandwidth of (up to) 2.1 GHz and, more generally, an easier and quicker re-use for any scientific observing mode: this is what SARDARA offers. Figure 4.9 shows a block diagram of the system. The ROACH2 boards are reconfigurable and suitable for the wide required bandwidth; additionally, we are part of CASPER, namely a consortium where the motto is “hardware and software are open source”. The system consists of seven ROACH2 boards equipped with two 5 GSample/s ADCs and mezzanine cards 10 Gbe SFP+. The eight outputs of the mezzanine cards are used to connect each ROACH2 board to all of the others and to a GPU-based PC, in which a dual port SFP+ 10 Gbe is installed. A 24-port SFP+ 10 Gbe is employed to interface computers with a high-performance data storage unit.

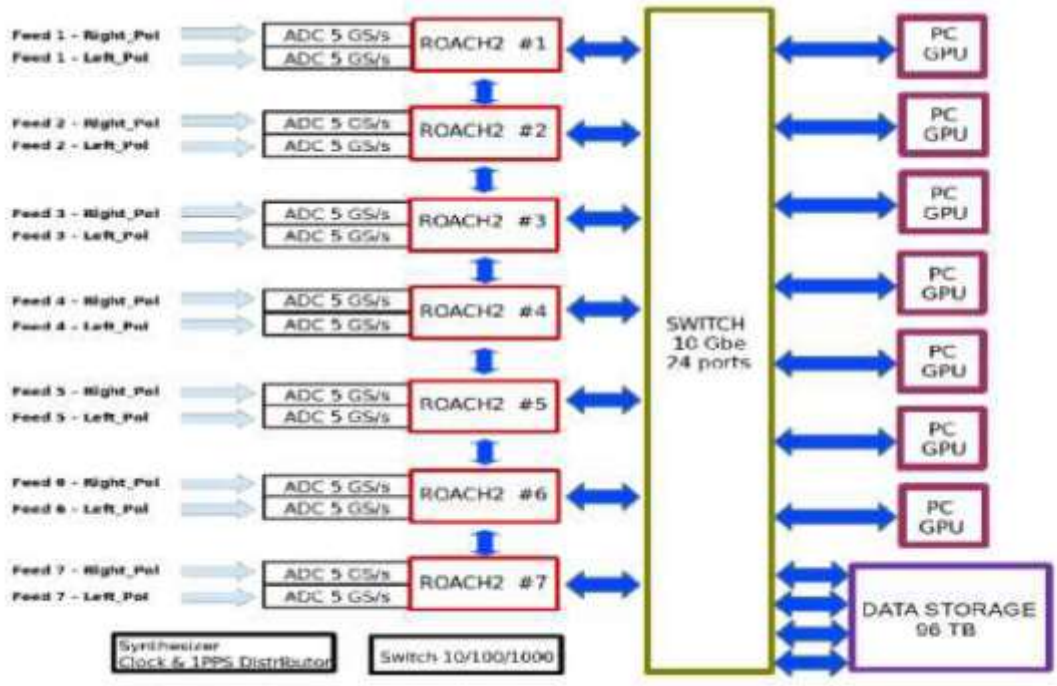

Fig. 4.9. Block diagram of the SARDARA system.

4.6 Overview

A recapitulation of the characteristics of the SRT discussed in this chapter are proposed in table 4.6.

Table 4.6. Overview of the SRT characteristics.

Position	San Basilio (CA), loc. Pranu de Sanguini
Coordinates	Lat. 39° 29’ 50” N, Long. 09° 14’ 40” E
Optics	Gregorian shaped + BWG
Parabolic reflector diameter	64 m
Elliptical sub-reflector diameter	8 m
BWG mirrors diameter	2.9 ÷ 3.9 m
Multi-beam receivers	22 GHz (7 feeds)
Foci	*Primary* f/D = 0.33 *Gregorian* f/D = 2.34 *2xBWG I* f/D = 1.38 *2xBWG II* f/D = 2.81
Elevation excursion	5° ÷ 90°
Azimuth and elevation speed	0.85°/sec in Azimuth, 0.5°/sec in Elevation
Superficial accuracy	630 μm (passive surface) 190 ÷ 200 μm (active surface)
Operating frequencies	0.3 ÷ 100 GHz
Pointing	11 ÷ 1.8 arcsec
Resolution	19.5 arcmin/f (GHz)
Gain	43.5 ÷ 91.7 dBi
Sidelobe level	- 20 dBi
Receivers mounting	*Primary focus*: mobile positioner with 4 housings *Gregorian focus*: rotating cylinder with 8 housings *BWG I-II*: fixed with 4 housings

5. SPACE DEBRIS OBSERVATIONS WITH THE SRT

The SD monitoring has become part of the joint DIEE-OAC research group activity since 2015, within the framework convention n. 2015-028 R.O. between the Italian Space Agency (ASI) and the National Institute for Astrophysics (INAF), named "Space Debris – IADC activity support and SST pre-operative validation". In this framework, the research group activity concerned the testing of the SRT operative capability in detecting signals scattered from SD, illuminated by a transmitter in P-band. The first test concerning the ability of the SRT in SD monitoring date back to April 17th 2014 [5], when the radio telescope was tested in a bi-static configuration and in survey mode. Before those experiments, a detailed forecasting campaign was made to predict the characteristics of the received echoes.

5.1 Bi-static Radar for LEO Tracking

The radar configuration studied and employed for the SD measurement experiments is a bi-static one, where the transmitter and receiver antennas are separated. In particular, the transmitter is the Flight Terminator System (FTS), a small, large-beam-width, sector antenna with 13 dBi gain, owned by the Italian Air Force (AFI) and located inside the Italian Joint Test Range in the region Salto di Quirra (PISQ), at coordinates Lat. 39.493068° N – Long. 9.64308° E (Sardinia Island). The receiver is, obviously, the SRT. Since this architecture was originally designed to perform the tracking of the objects, it was named Bi-static Radar for LEO Tracking (BIRALET). The two antennas are both located in Sardinia, with a baseline of about 40 km; comparing this distance with the range of the debris, the radar configuration could be almost presumed to be a mono-static one.

The FTS is composed by a powerful amplifier, capable to supply an averaged and leveled power of 4 kW within the bandwidth 400-455 MHz. The FTS was always employed in Continuous Wave (CW) mode at 410 MHz and, consequently, this prevented the possibility to directly measure the object range, which was obtained analytically. The list of the objects to observe, which comprehended not only debris but also small satellites, was provided by the Italian Air Force; it was characterized by a good spread in terms of RCS as well as of range values.

5.2 Forecasting campaign

Before the measurement campaign of April 17th 2014, a brief but exhaustive forecasting campaign was carried out, in order to predict the level of signal of the received

echoes and the pointing coordinates of the SRT. The list of the objects to detect, as provided from the Italian Air Force, (AIF) is shown in table 5.1.

Table 5.1. List of the objects to detect, with name, International Designator, Radar Cross Section, distance from FTS and SRT, altitude and FTS turn-on and turn-off times in UTC.

Name	**ID**	**RCS [m^2]**	**Range from FTS [km]**	**Range from SRT [km]**	**Altitude [km]**	**Start time [UTC]**	**Stop time [UTC]**
COSMOS 2237 (first passage)	22565	11.6	865	867	853.6	08:22:40	08:23:00
COSMOS 2237 (second passage)	22565	11.6	1384	1452	852.7	08:25:30	08:25:50
HJ-1A (first passage)	33320	1.5	1842	1798	620.7	08:56:33	08:56:53
HJ-1A (second passage)	33320	1.5	930	902	629.3	08:59:00	08:59:20
CARTOSAT 2A	32783	2.34	1023	1033	629.4	09:10:50	09:11:10
COSMOS 1408	13552	8.45	542	551	523.7	09:30:05	09:30:15
COSMOS 1375	16206	0.48	1185	1141	984.8	10:23:30	10:23:50
VESSELSAT 2	38047	0.28	854	810	460.7	10:51:30	10:51:50

As it can be seen from this table, the transmission was characterized by a total switch on time of about 20 seconds for all the passages, except for the COSMOS 1408, for which the transmission time was of 10 seconds.

In order to forecast the possible object detections, the ESA's software PROOF (Program for Radar and Optical Observation Forecasting) 2009 was used. PROOF 2009 is a software developed by the European Space Agency for the simulation of radar- and telescope-based space debris observations. This software can be a useful tool, in order to plan SD observations and validate previous campaigns. PROOF's simulations need specific parameters in input, mostly tied to the geographical coordinates and the operational settings of the radars and/or telescopes in use (e.g. operating frequency, antenna beam-width, transmission power, etc.) and, of course, to the observation epoch. It is worth mentioning that PROOF cannot run properly without an up-to-date debris population file, which describes the distribution of the objects at a given astronomical epoch. Obviously, the epoch of the population file must be as close as possible to the epoch of the planned observation. Unfortunately, the PROOF database provides population files updated to 1st May, 2009, so that simulations carried out after this specific date could be highly inaccurate. This is the main reason why PROOF should not be used without the support of ESA's MASTER (Meteoroid and Space Debris Terrestrial Environment Reference Model) 2009, a software for the characterization of the natural and man-made particulate environment of the Earth. MASTER's database is constantly updated and it can be used as a reference by PROOF to propagate the last population file available up to the requested epoch.

Once the list of the objects to detect and the illumination time are available, it is necessary to obtain the pointing coordinates (azimuth and elevation angles) for the single radar involved or for the multiple radars in case of bi-static configuration. In the case of the BIRALET system, two sets of pointing coordinates were needed, one for the FTS and the other one for the SRT. Instead of the azimuth and elevations coordinates evaluated for the measurement campaign (where a Python script specifically designed for the event was created), at the time of the forecasting campaign we used the amateur software WXtrack, developed by David Taylor and available for free on the internet. WXtrack allows to obtain the pointing coordinates, for all the catalogued objects, by inputting in the software the coordinates of the radars involved, the time of the passage and the TLE of the objects to observe.

Fig. 5.1 shows the first result of the PROOF simulation, reporting the number of objects detectable by the BIRALET architecture on April 17th, 2014. It can be seen that there is a large number of objects, located at altitudes between 600 and 2 000 km (LEO) that crosses the area illuminated by the FTS and the SRT. However, the red line indicates

that these objects cannot be detected by the BIRALET system, probably because of their small dimension. Nevertheless, there is a significant amount of objects, represented by a light blue line (which identifies the objects catalogued with TLEs), that crosses the illuminated area and that can be detected by the given configuration. Similar results can be obtained also considering different parameters than the altitude (e.g. diameter, range, RCS, etc.).

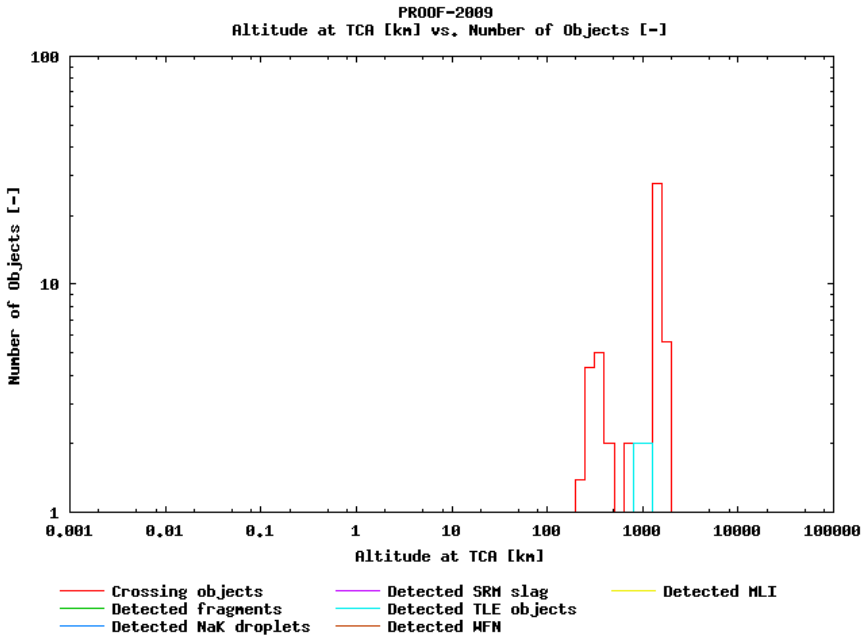

Fig. 5.1. Number of crossing (red line) and detectable (light blue line) objects by the BIRALET configuration, during the whole day of the 17 April 2014.

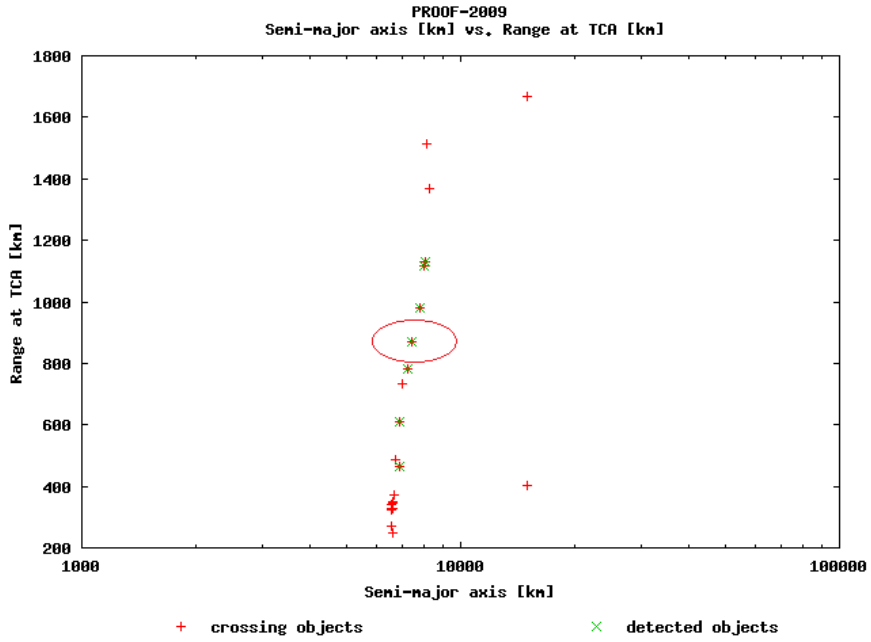

Fig. 5.2. Detection of the COSMOS 2237.

It is also possible to identify a particular debris among the others, even if the process can be complicated. For the sake of simplicity, only one of these diagrams (for a single passage of a single debris) will be shown in Fig. 5.2. The SD taken into account is the COSMOS 2237 in its first passage (as reported in table 5.1). According to the information extracted by WXtrack, this specific debris could have been detected at 08:22:40 UTC on 04/17/2014 (the observation epoch) pointing the FTS toward 144.8° Azimuth and 79.3° Elevation and the SRT toward 109.8° Azimuth and 79.3° Elevation, at a range of about 866 km from both the transmitter and the receiver. From the TLE it is possible to obtain the semi-major axis of the object orbit, which for COSMOS 2237 happened to be equal to about 7 200 km. In Fig. 5.2, it is pretty clear that the debris found by the PROOF simulations is the COSMOS 2237. It follows from this that the procedure to find a singular debris could be very difficult. For this reason PROOF and MASTER should be employed exclusively to know a priori the possible detection of the radar configuration in use.

Another useful information to plan an observation campaign is the evaluation of the back-scattered power from the debris as a function of the RCS and the range of the object. This value can be compared with the noise floor level, due to environmental conditions, to obtain the maximum SNR at the receiver. As a rule of thumb, in order to spot the passage of the object, the level of the back-scattered power must be higher than the noise floor level by at least 10 dB. This prevent the eventuality of a missed detection due to the overall losses of the system. Actually, it is possible to retrieve the information about the passage of a debris even if the peak of back-scattered power is entirely covered by the noise, but this case will not be treated in this dissertation. The noise floor level can be evaluated as:

$$N_F = k_B T_{SYS} B_N \tag{32}$$

where k_B is Boltzmann's constant, T_{SYS} is the system noise temperature evaluated as the sum of the antenna temperature T_A and the receiver temperature T_R, and B_N is the noise bandwidth, set by the bandwidth of the last useful filter (as it will be discussed later, in our case it is equal to the Resolution Bandwidth (RBW) of the instrument employed for the measurements). The back-scattered power is calculated using the radar equation shown in equation (5). The characteristics of the BIRALET configuration, useful to evaluate the radar equation and the SNR, are reported in table 5.2. As shown in Fig. 5.3, in the configuration used on April 17th 2014, the BIRALET system was able to detect objects

larger than 5 cm^2 at a range of 200 km, with RCS larger than 0.3 m^2 at a range of 1000 km and with RCS larger than 4 m^2 at a range of 2000 km.

Table 5.2. Main features of the BIRALET system.

Antenna Parameter	Transmitter Antenna (FTS)	Receiver Antenna (SRT)
Gain [dBi]	13	47
3dB-Beamwidth [deg]	30	0.8
Receiver Noise Temperature T_R *[K]*	-	20
Aperture Efficiency	N/A	0.6
Physical Area $[m^2]$	N/A	3217

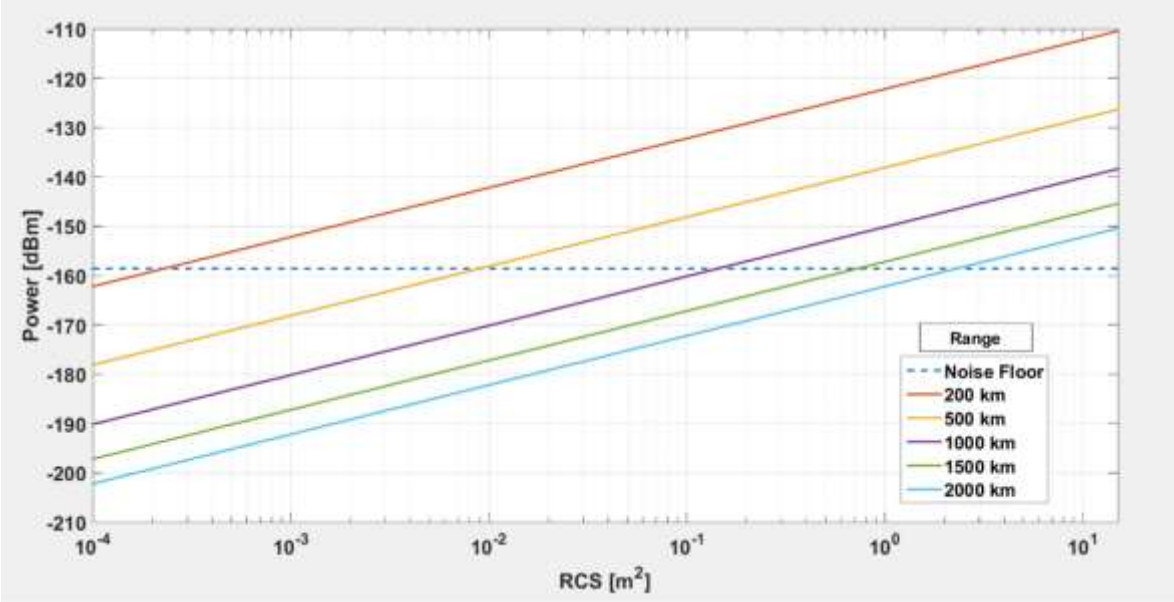

Fig. 5.3. Back-scattered power at the receiver antenna (SRT) as a function of the RCS of the object, for different values of the range from the SRT at 410 MHz.

5.3 Space debris measurement campaign of 17 April 2014

Phase 2 of the Military Aeronautics (AM) – INAF agreement on Space Situational Awareness (SSA) included a set of measures in the UHF band for LEO space debris observations. As already said, the antennas employed in the radar configuration named BIRALET were the FTS as a transmitter and the SRT as a receiver. After a preliminary

test, during April 14th, 2014, three days later the real detection campaign begun. During this session, a sinusoidal signal (CW) of about 4 kW at 410 MHz was transmitted from the FTS to the debris sorted out by the AFI, and the scattered echoes have been detected by both the Northern Cross and the SRT. The session objectives for the SRT were:

- Target revelation (SNR), acquisition time and radar echo loss;
- Measurement of the relative target speed (Doppler frequency);

The back-end used during the sessions were at first the HP 8594E spectrum analyzer, for the preliminary test of April 14th, 2014, and then the Agilent A4446E for the measurements of the April 17th, 2014, with the following setup:

- FFT mode;
- Span 100 kHz (200 kHz for the detection of the COSMOS 2237);
- RBW 200 Hz (400 Hz for the detection of the COSMOS 2237) with 500 points;
- Video Bandwidth (VBW) 200 Hz.

Moreover, for almost all the passages except for the VESSELSAT 2, an amplifier with 25dB-gain was inserted in the measurements setup, and an attenuation of 10 dB was set in the spectrum analyzer. The exact azimuth and elevation pointing coordinates of the SRT, have been calculated for every object using a Python script, before the measurement campaign, as can be summarized below:

1) The TLEs (downloaded the day of the observation) of the objects (satellite or debris) are propagated using a Simplified General Perturbation model 4 (SGP4) up to the UTC time (hh:mm:ss) of the observation.
2) The script takes the latitude, longitude and altitude of the antenna location (in this case the SRT), and the UTC observation date (in the format yy/mm/dd, hh:mm:ss) as input data.
3) The script computes the position of the object (azimuth and elevation) with respect to the location of the observer. The azimuth and elevation angles are computed in terms of degrees, arcminutes and arcseconds with an overall precision up to the third decimal place (more accurate than the coordinates provided by WXtrack), which fits well with the SRT pointing precision of 0.002 degrees.

The above algorithm is also designed to allow a sequential pointing useful for both detection and tracking scenarios. The azimuth and elevation coordinates for the SRT resulting from the script, for every listed object, are shown in table 5.3.

Table 5.4 shows the name (and passage) of the listed object, the duration of the received echoes (visibility interval), the Doppler shift and the SNR, computed as:

$$SNR\ [dB] = DPP\ [dBm] - N_F\ [dBm] \quad (33)$$

wherein DPP is the debris peak power, i.e. the power measured by the spectrum analyzer for a debris at the center of the visibility interval (table 5.4).

Table 5.3. Azimuth and elevation pointing angles for the SRT.

Name	Azimuth [deg]	Elevation [deg]
COSMOS 2237 (first passage)	109.779	79.253
COSMOS 2237 (second passage)	28.829	31.028
HJ-1A (first passage)	18.834	13.501
HJ-1A (second passage)	32.789	42.209
CARTOSAT 2A	22.763	36.993
COSMOS 1408	92.120	71.059
COSMOS 1375	204.524	57.018
VESSELSAT 2	30.764	32.009

Table 5.4. Azimuth and elevation pointing angles for the SRT.

Name	Visibility Interval [s]	Doppler Shift [kHz]	SNR [dB]
COSMOS 2237 (first passage)	0.440	Doppler not measured	39.8
COSMOS 2237 (second passage)	0.473	-5.2	29.4
HJ-1A (first passage)	0.305	+6.2	16.4
HJ-1A (second passage)	0.380	+4.6	15.8
CARTOSAT 2A	0.296	+5.2	11.7
COSMOS 1408	0.507	Doppler not measured	37.2
COSMOS 1375	0.414	+3.4	10.8

VESSELSAT 2	0.390	+5.2	17.4

Figures 5.4 – 5.11 show the spectrogram as a function of frequency and observation time and the screenshots of the spectrum analyzer at the center of the visibility interval for each debris.

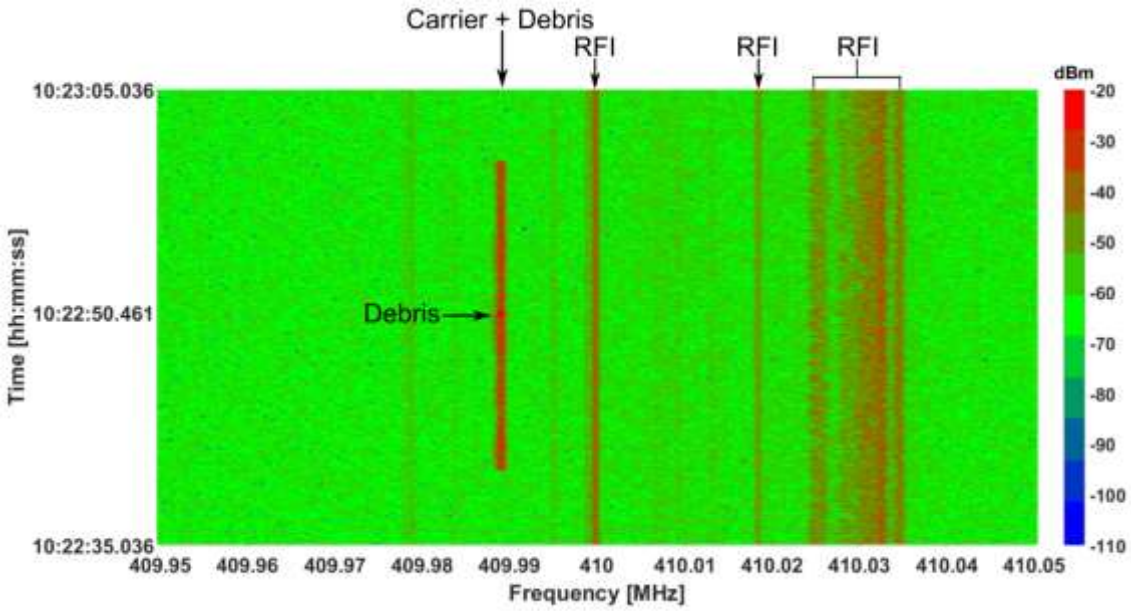

a)

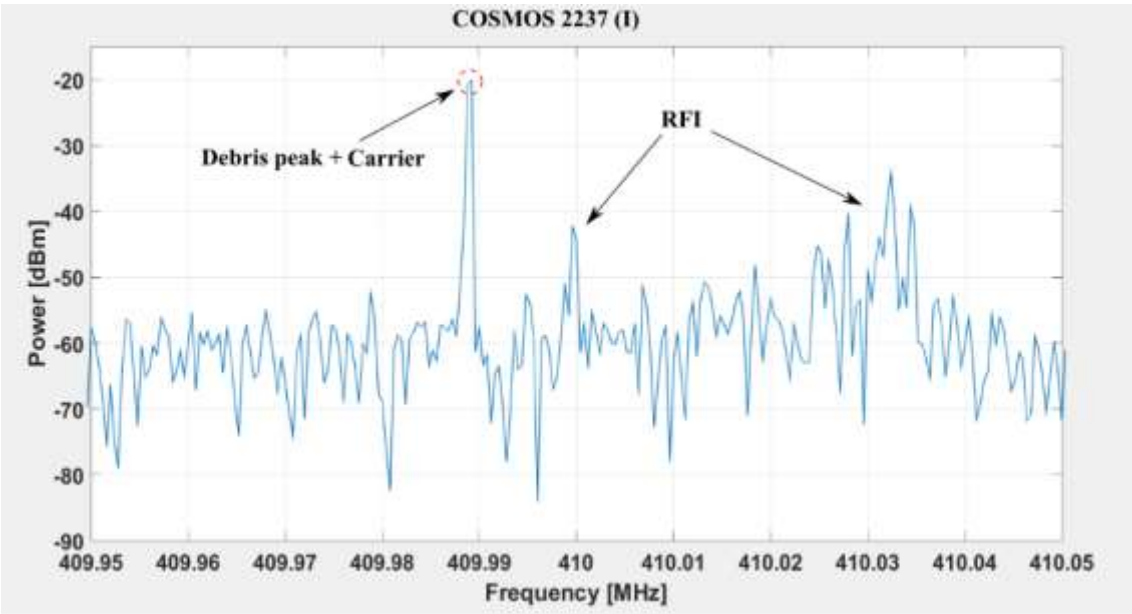

b)

Fig. 5.4. First passage of the COSMOS 2237: a) spectrogram; b) screenshot of the spectrum analyzer at the center of the visibility interval.

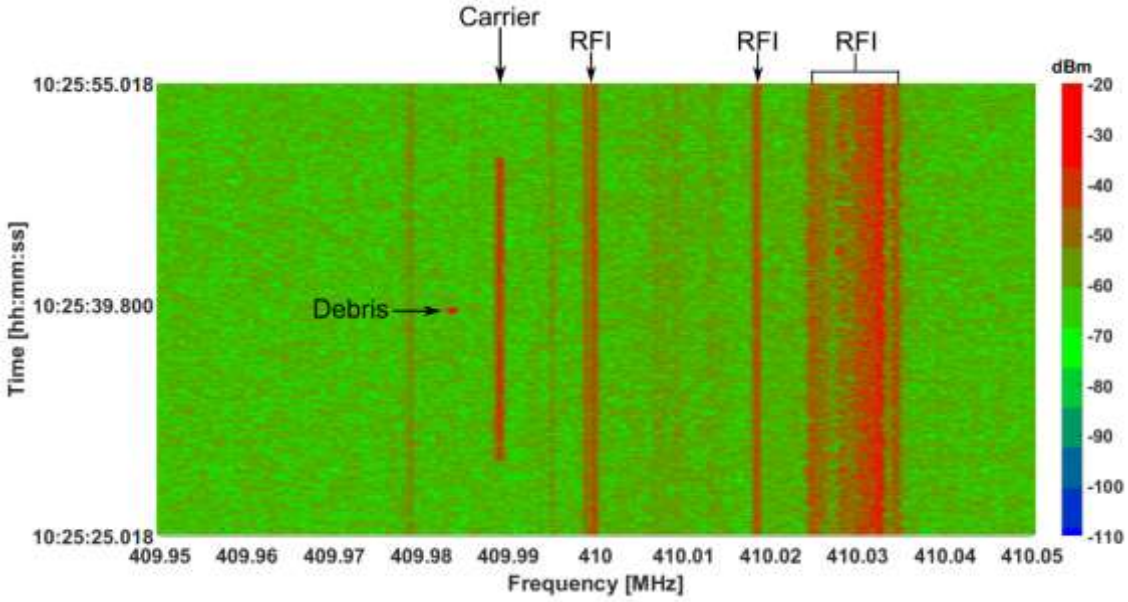

a)

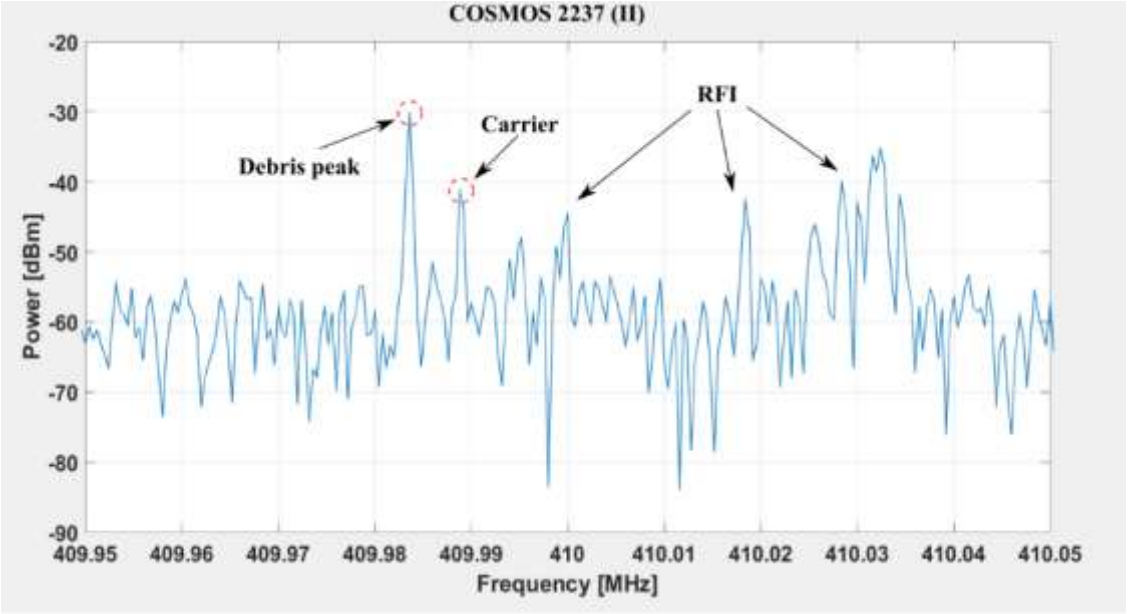

b)

Fig. 5.5. Second passage of the COSMOS 2237: a) spectrogram; b) screenshot of the spectrum analyzer at the center of the visibility interval.

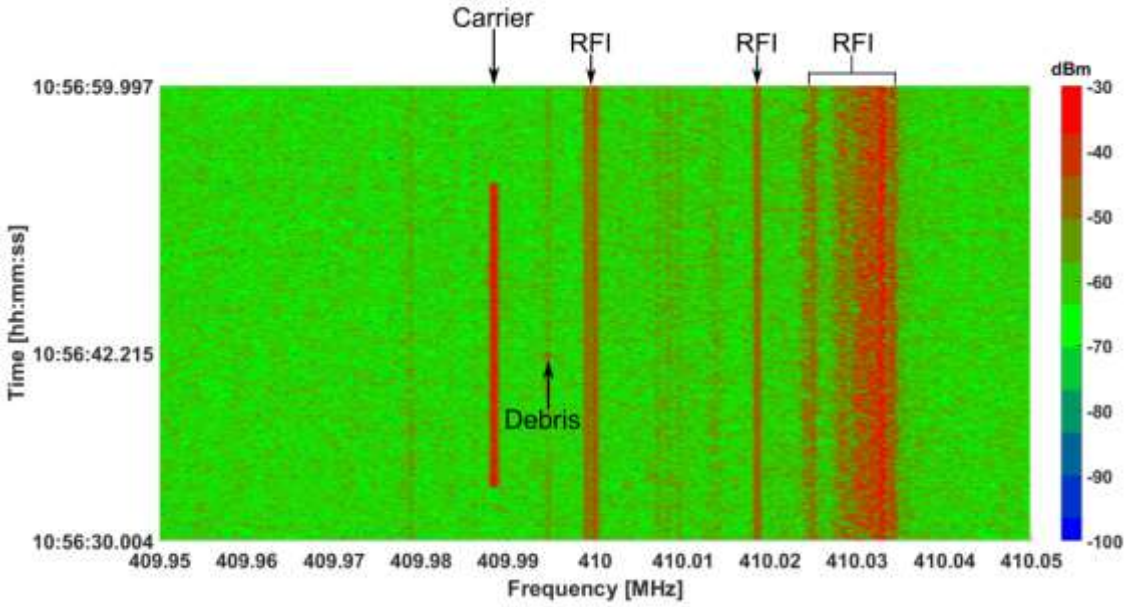

a)

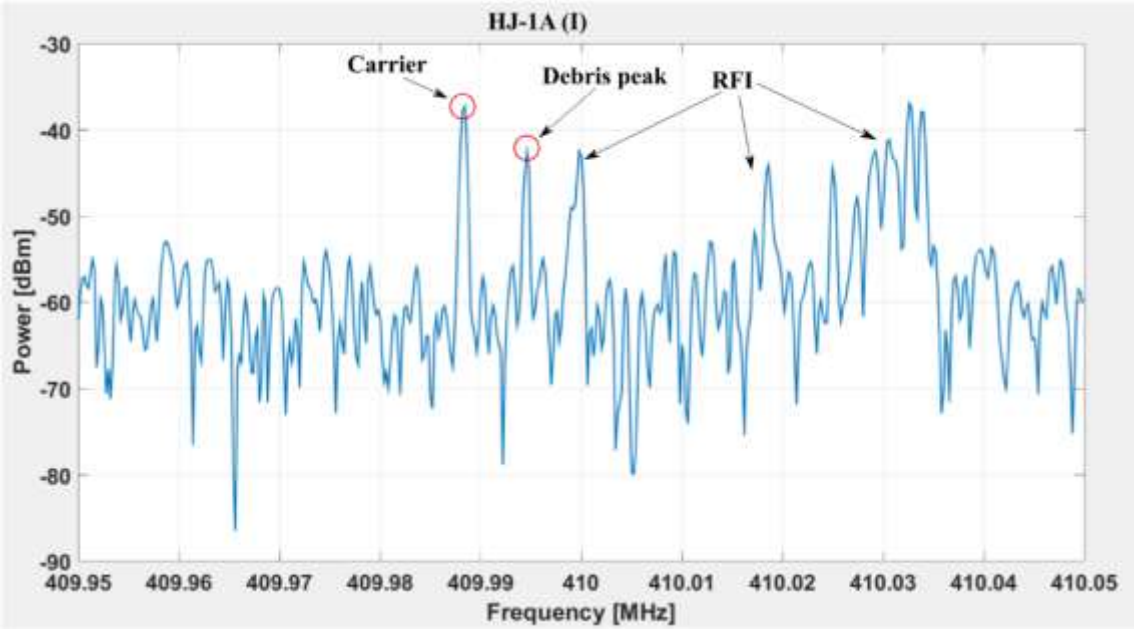

b)

Fig. 5.6. First passage of the HJ-1A: a) spectrogram; b) screenshot of the spectrum analyzer at the center of the visibility interval.

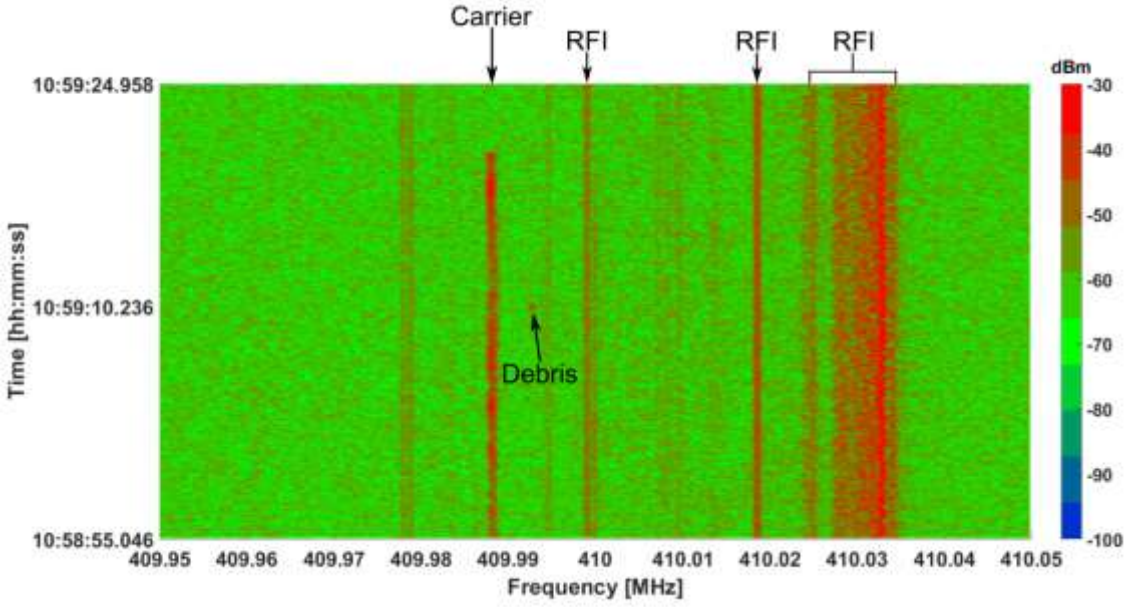

a)

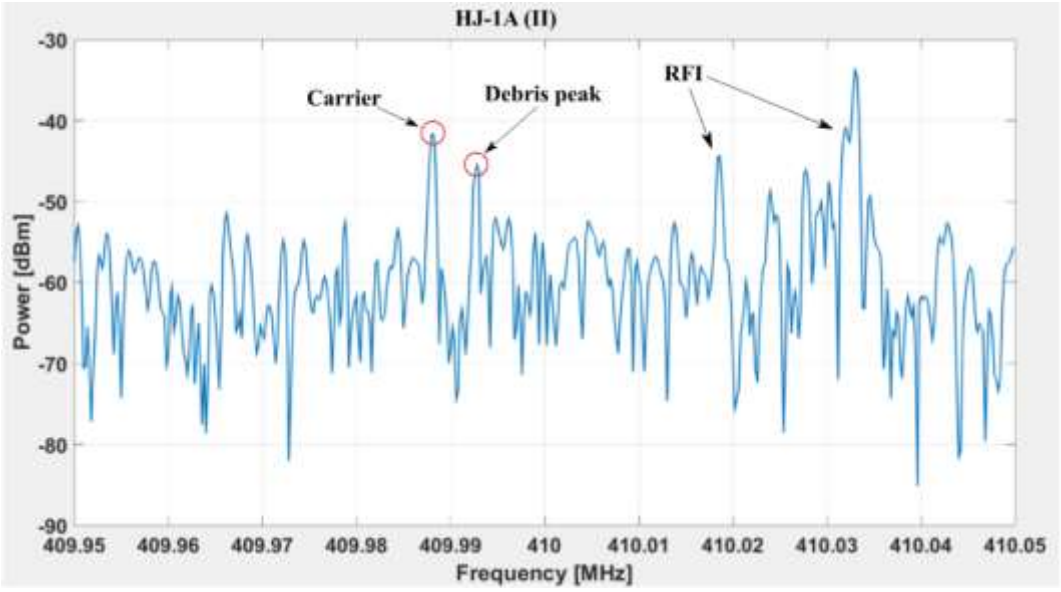

b)

Fig. 5.7. Second passage of the HJ-1A: a) spectrogram; b) screenshot of the spectrum analyzer at the center of the visibility interval.

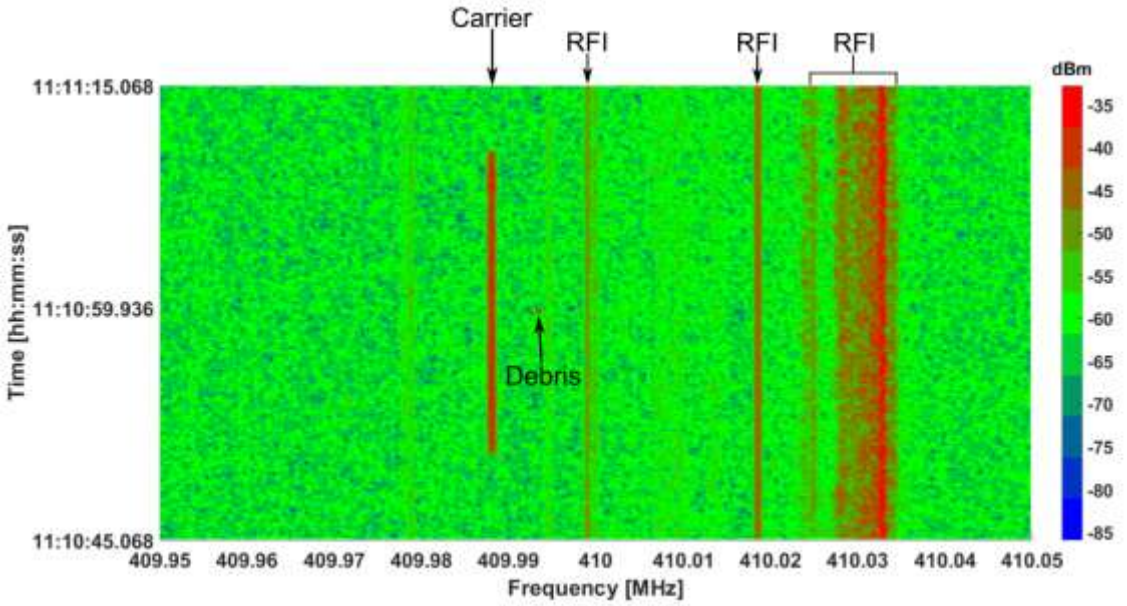

a)

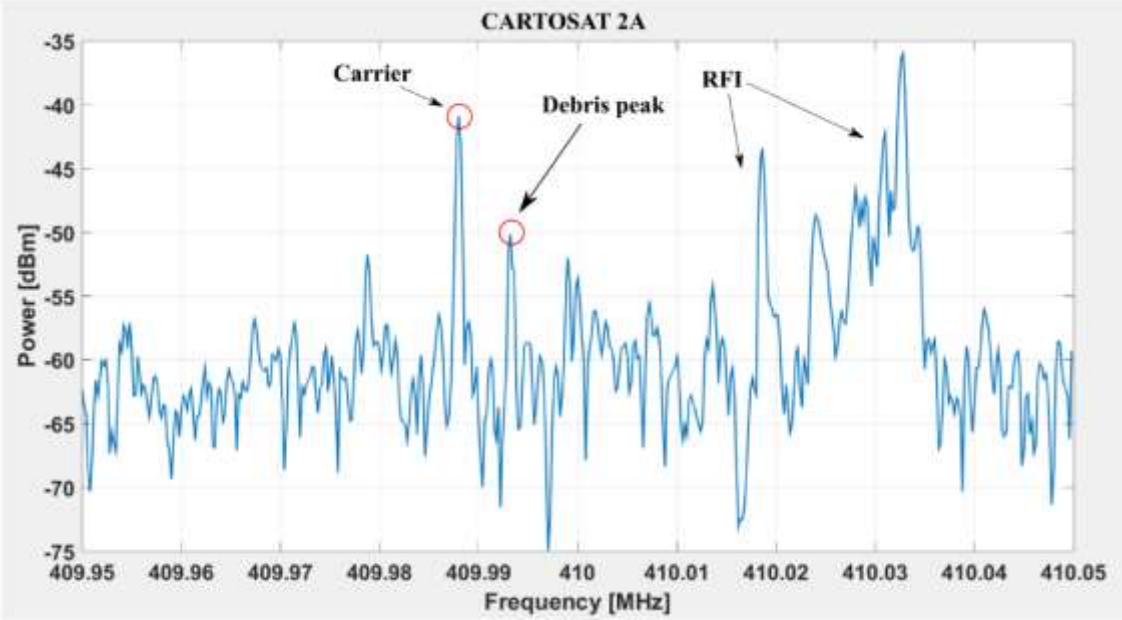

b)

Fig. 5.8. Passage of the CARTOSAT 2A: a) spectrogram; b) screenshot of the spectrum analyzer at the center of the visibility interval.

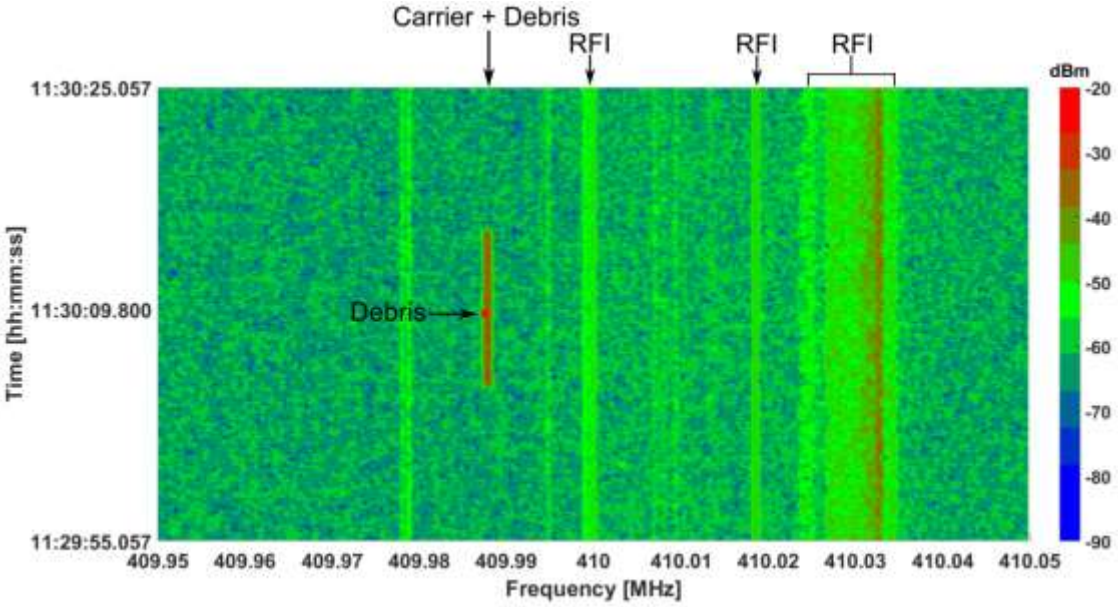

a)

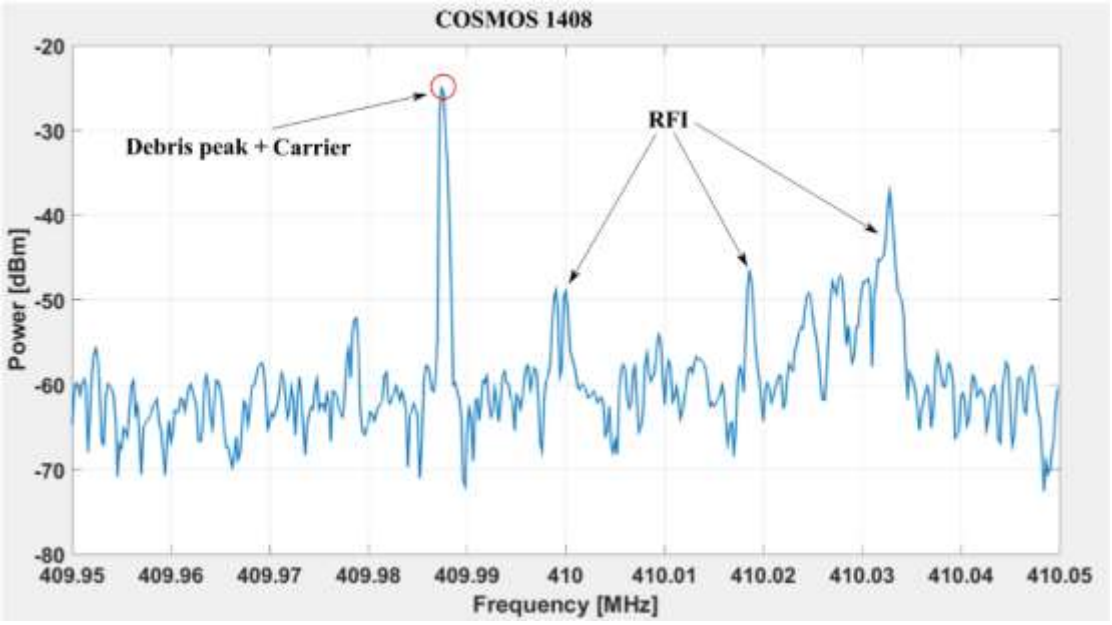

b)

Fig. 5.9. Passage of the COSMOS 1408: a) spectrogram; b) screenshot of the spectrum analyzer at the center of the visibility interval.

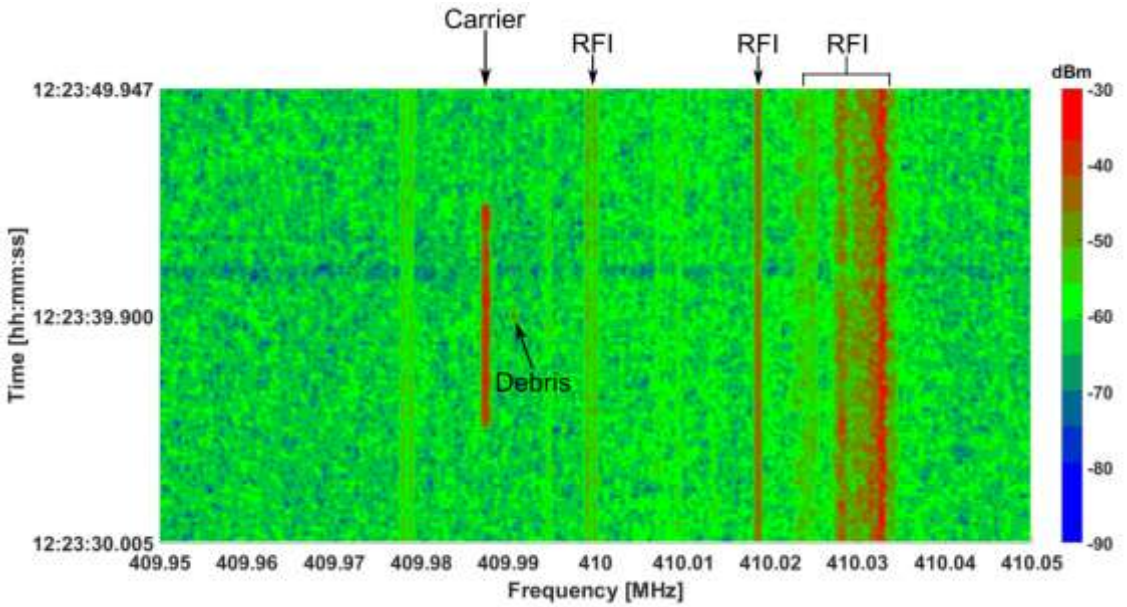

a)

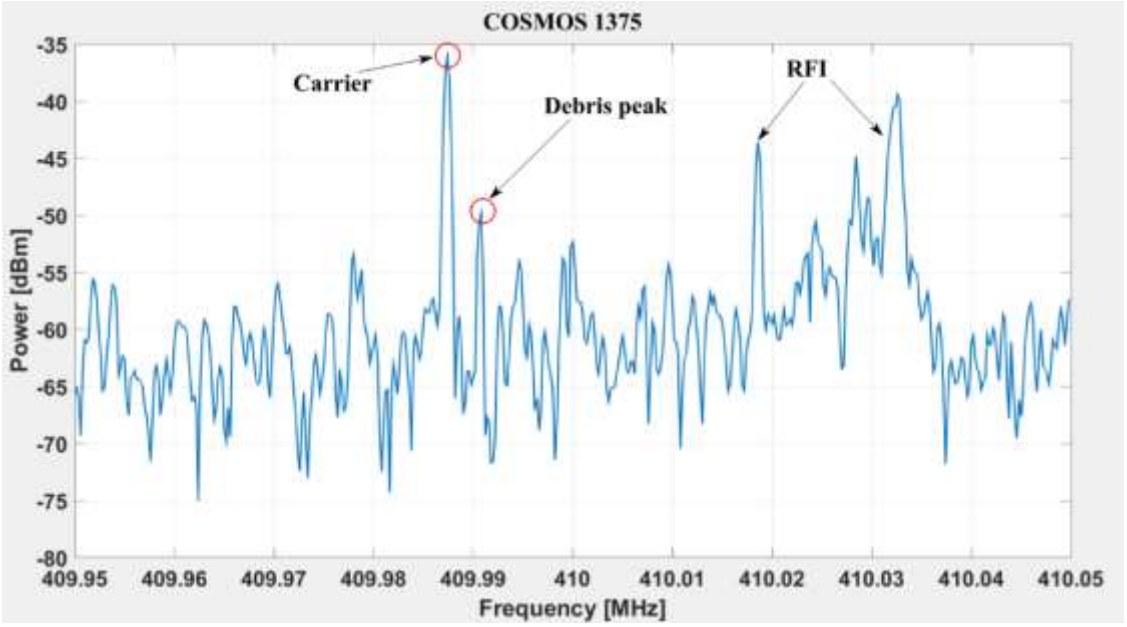

b)

Fig. 5.10. Passage of the COSMOS 1375: a) spectrogram; b) screenshot of the spectrum analyzer at the center of the visibility interval.

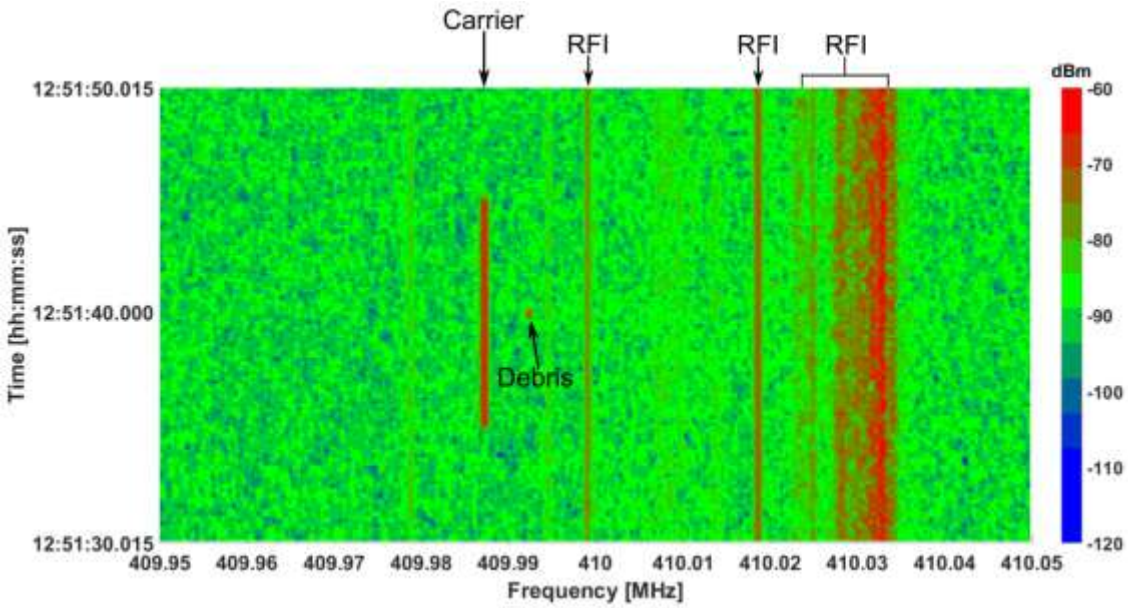

a)

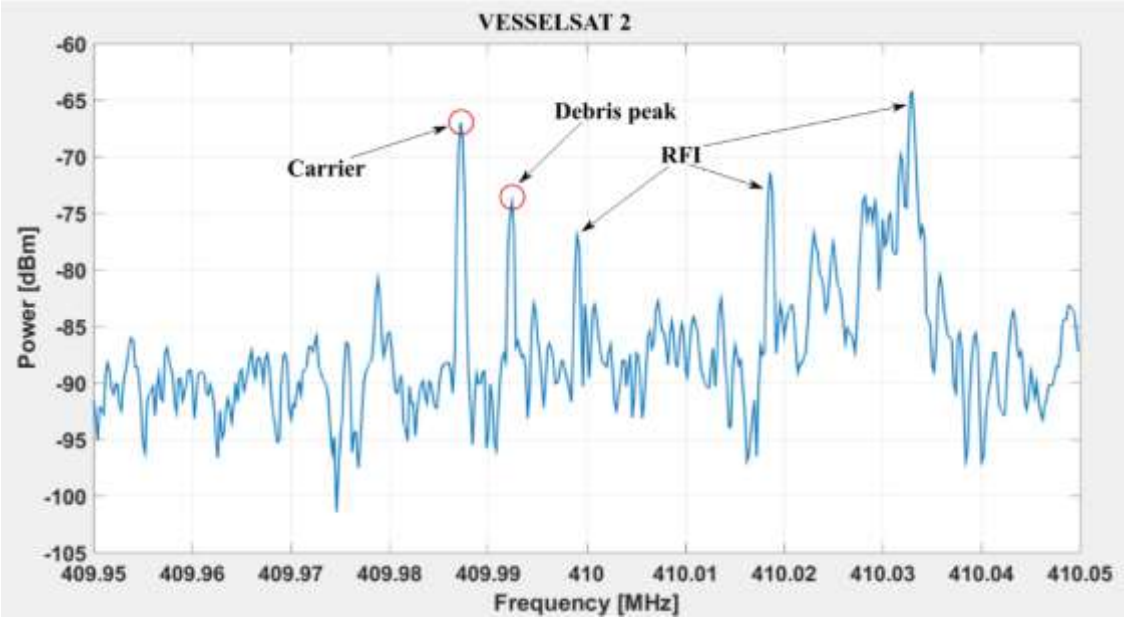

b)

Fig. 5.11. Passage of the VESSELSAT 2: a) spectrogram; b) screenshot of the spectrum analyzer at the center of the visibility interval.

The Doppler shift reported in table 5.4 has been computed by the difference between the carrier frequency and the echo from the debris/satellite (as clearly visible in the screenshots of the spectrum analyzer reported above). Due to the proximity of the transmitter and receiver antennas the carrier frequency is plainly visible in all the spectrograms as well as in the spectrum analyzer screenshots. From these results it can be stated that every object in the list was successfully detected, though in two cases (COSMOS 2237 first passage and COSMOS 1408 in Fig. 5.4 and 5.9) the Doppler shift was not evaluable, since it was smaller than the RBW used in the spectrum analyzer options (from the figures it can be seen that the peak of the carrier virtually overlaps with the echo scattered from the object). It should be noted, as the dissertation will go back to the topic in the next chapter, that during the measurement campaign, part of the bandwidth was occupied by Radio Frequency Interferences (RFIs), which are clearly visible in the spectrograms of figures 5.4 – 5.11 as continuous lines. The P-band is a spectral region largely used for radio communication services, this may lead to a reduction of the useful bandwidth and to the compression of the dynamic of the receiver [22]. These RFIs are related to the Terrestrial Trunked Radio (TETRA) assigned to the Italian Ministry of Defense. The members of the joint research group were aware of the exact frequency of the RFIs, but an automatic system to mitigate the effects of the interferences was not yet available at the time of the observations.

6. UPGRADE OF THE SRT

The measurement campaign of the 17 April 2014 can be considered a first test of the capabilities of the SRT as a receiver in a bi-static configuration for space debris monitoring purposes. The results of the latter campaign could be definitively considered encouraging, since the SRT is a powerful instrument, even if compared to the other Italian cornerstone of the SD monitoring, the Northern Cross. In fact, the SRT can currently count on a higher effective area with respect to the Medicina array, and, consequently, on a higher gain. This works in favor of the overall sensitivity of the radio telescope, which, on equal terms of operating frequency and transmitted power, is able to detect smaller and/or more distant objects. However, the main difference between the two receiving sites is that the Northern Cross is completely devoted to the SD monitoring, whereas the SRT has to share the operating time with other demands, mostly tied to radio astronomical applications. One of the main downsides of this aspect is the lack of SD dedicated receivers on the SRT. Sure enough, the receiving channel for the first SD monitoring experiment was not optimized for the purpose, having exploited an existing channel for radio astronomy applications. In particular, the P-band receiver of the SRT has been used for the detection of pulsars and for ionized hydrogen mapping. Radio astronomical applications are characterized by very large bandwidths both on the front-end side and the on back-end side. This is due to the fact that radio astronomical sources are often “unknown” and large radio telescopes, such as the SRT, are frequently used to discover new sources, thus without knowing the precise frequency, the bandwidth and even the amplitude of the received signal. The characteristics of these signals require that the antenna covers a wide spectral regions. Instead in SD monitoring applications, the signals are characterized by narrow bandwidths. The back-end usually employed for the radio astronomical observations has already been described in chapter 4. In the P-band, every system presented is usable, but, as it can be seen from Fig. 4.5, 4.6 and 4.7, the working bandwidths are still very wide for SD monitoring. Some of these back-end architectures are based on the standalone Field Programmable Gate Array (FPGA) board named Reconfigurable Open Architecture Computing Hardware (ROACH), characterized by very high output rates (the order of 10 Gbps) and large bandwidths (the order of GHz). Once again, the board is designed to work as a back-end for the observation of distant radio astronomical source, and, although a high data rate could be useful even for SD monitoring, the overall features of this FPGA are a waste of resources for this application. During the experiments on 17 April 2014, the receiving chain of the P-band

was simply connected to a spectrum analyzer (see the previous chapter for details), as shown in Fig. 6.1. This choice was dictated by the lack of opportunities available at that moment, since no SD dedicated back-end was ready to be even tested and using an already existing radio astronomical back-end was not a reasonable option, for the above mentioned reasons.

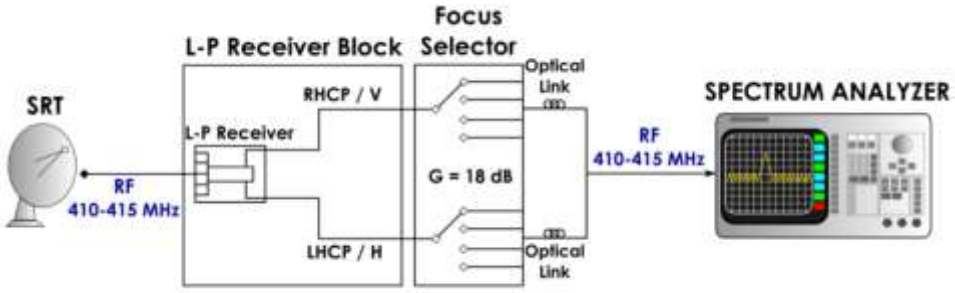

Fig. 6.1. Measurement setup of the P-band receiving chain for the 17 April 2014 observations.

However, spectrum analyzers can be characterized by technical limitations, i.e. speed of the frequency sweep tied to the RBW, poor processing capabilities, missing information due to the "blind time" during the calculations (sampling time). Considering that the typical passage time of a debris in LEO inside the beam of SRT (in P band) can be lower than 500 milliseconds [5], using a non-performing detector may lead to an impairment in the identification of the echo. It is worth remarking that the BIRALET system is a bi-static radar configuration. The two antennas are managed by totally different organizations. Thereby, the choice of the operating frequency of the whole system is determined by the transmitter specifications. Since the transmitter operates in the 400-420 MHz frequency range (the details of the transmitting antenna are reported in the next paragraph), the selection of the P-band receiver of the SRT was mandatory. Unfortunately, the area surrounding the SRT is polluted by many RFIs in the P-band, in particular:

- The 318-321 MHz bandwidth, employed for VOIP telephone services.
- The 327-332 MHz bandwidth, dedicated to the military services.
- The 350 MHz frequency, used for the control system of a near military facility.
- The 385-395 MHz bandwidth, assigned to the TETRA, already mentioned in the previous chapter.
- The 400 MHz frequency, occupied by the control signal of a local TV radio link.
- The 406.8 MHz frequency, utilized for WX weather balloon.

Since the latter measurements, the transmitting antenna of the BIRALET system has been changed from the FTS to the TRF (Radio Frequency Transmitter). The TRF is able to supply a maximum power of 10 kW in the bandwidth 410-415 MHz. Similarly to the FTS, up to now, the new TRF in CW mode allows only the Doppler shift and Signal-to-Noise ratio (SNR) measurements.

A step ahead from the described scenario was the planning and the realization of a new receiving chain for the P-band receiver, in order to make it suitable for SD measurements, reducing the global observation bandwidth, limiting the RFI problem and developing a dedicated back-end. Therefore, the main features in this design had to be focused on the insertion of multiple filtering stages, on the suppression of the interferences inside the observation bandwidth and on the design of a new performing back end. Within this context, the inclusion of a new, dedicated channel for the space debris inside the P-band receiving chain of the SRT is described hereafter.

6.1 The new BIRALET system

As already mentioned above, the transmitter antenna of the BIRALET system has been changed. The TRF (Fig. 6.2), located in the Italian Joint Test Range in the region “Salto di Quirra” (PISQ, Cagliari, Sardinia, Italy), is a 7 m fully steerable wheel-and-track parabolic antenna with a primary focus configuration. The azimuth and elevation excursion of the antenna ranges from 0 to 360 degrees and from 0 to 90 degrees, respectively, with an accuracy of 0.1 deg and a speed of 3 deg/sec [19].

Fig. 6.2. Picture of the TRF antenna at the PISQ.

The system is composed by a set of 7 powerful amplifiers that allows to supply a maximum RMS power of 10 kW (continuous peak power of 14 kW). The latters are wide-band components, optimized to work in the frequency range 400-420 MHz, and filtered with a tunable central frequency (e.g. 412.5 MHz) and a bandwidth of 5 MHz. However, with some modifications, the transmitter could be employed at higher frequencies, since the reflector of the parabolic antenna has been designed to work up to 14 GHz. The block diagram of the system is shown in Fig. 6.3.

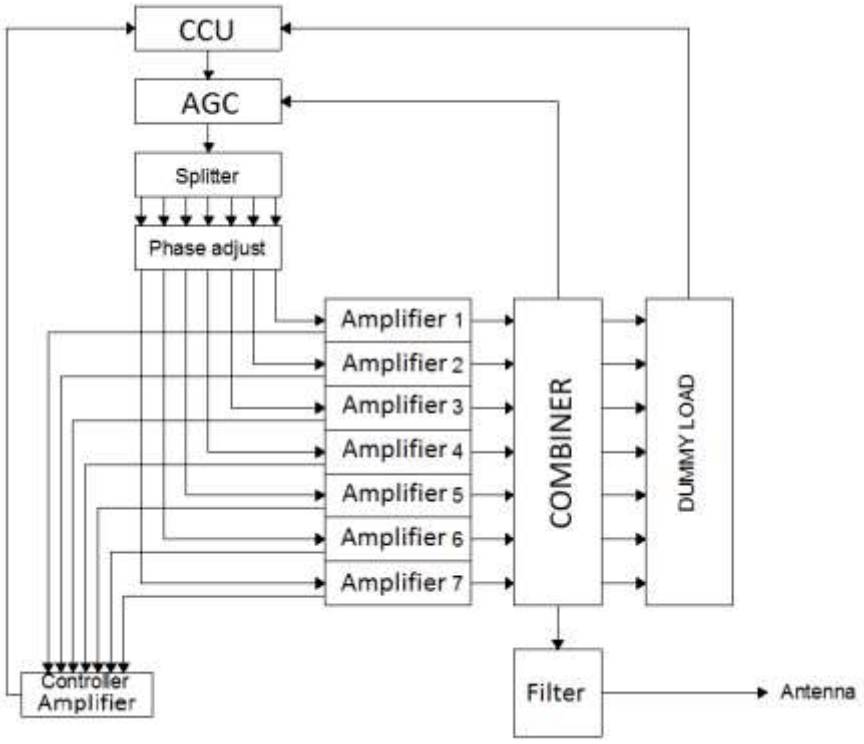

Fig. 6.2. Block diagram of the transmitting system.

The transmitter is composed by a central control unit (CCU) that takes in input a signal originated by a vector signal generator. The CCU is linked to an Automatic Gain Control (AGC) for the adjustment of the system gain depending on the level of the signal coming from the combiner. The AGC sends the signal to the radio frequency splitter. This block creates seven signals, adjusted in phase, each one for every power amplifier available (with nominal continuous peak power of 2 kW). After the power amplification block, the signals are combined, filtered with a low pass filter and sent to the antenna.

6.2 The P-band receiver of the SRT

The P-band receiver of the SRT, used for space debris monitoring within the BIRALET system, is installed on the primary focus of the antenna. The receiver is a cryogenic dual-band coaxial-feed, that simultaneous covers the frequency range of 305-410 MHz (P-band) and 1.3-1.8 GHz (L-band). The P-band section consists of a coaxial waveguide with two linear polarization. The original schematic of the P-band receiver, without the upgrade for space debris monitoring proposed in this dissertation, is shown in Fig. 6.3 [23].

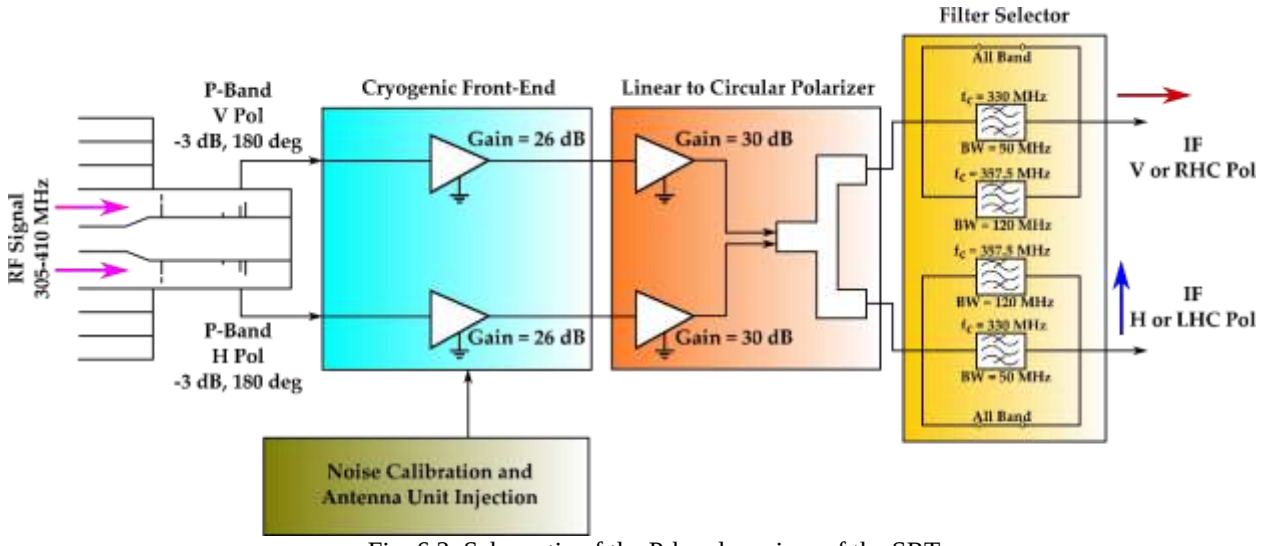

Fig. 6.3. Schematic of the P-band receiver of the SRT.

From the image, four main blocks can be identified: the Cryogenic Front-End (CFE), the Linear to Circular Polarizer, the Noise Calibrator and Antenna Unit Injection and the Filter Selector. The coaxial feed couples the free space Radio Frequency (RF) signal, between 305 and 410 MHz, into a guided wave. This wave propagates inside the coaxial waveguide to reach the coaxial ortho-mode junction that allows to split each polarization into two equal amplitude signals, out of phase by 180 degrees. In this way, the two signals are sent to the CFE block through two distinct equi-phase cables and they are recombined with a 180 degrees hybrid. The CFE block is directly connected with the Noise calibration and Antenna Unit injection block for the calibration of the whole system. The output signals from the CFE enter in the P-band Linear to Circular Polarizer block. This block allows to keep the linear polarizations of the two signals but at the same time to collect them in circular polarization (RHCP and LHCP). The last block is the P-band Filter Selector block, which allows the choice of a suitable filter for the observation [23].

6.3 The new SD dedicated channel

Given the speed of the objects traveling in LEO, which ensures that debris remains in orbit, despite the Earth's gravitational attraction, the passage inside the beam of a radio telescope at the microwave frequencies can be very quick [5]. Therefore, a good responsivity of the measurement and recording system is a priority during the SD monitoring. As shown in the schematic in Fig. 6.3, during the experiments on April 17, 2014, the two channels of the P-band receiver, one for each polarization, already used for radio astronomical measurements, were simply connected to a spectrum analyzer. The downside of this setup have already been outlined and they are mostly tied to the excessively wide band and to the poor processing capabilities. The latter can be avoided saving the entire bulk of raw data deriving from the observation and work in post-processing. A commercial System-on-a-Chip (SoC) FPGA Board, such as the Red Pitaya, can perform this particular task. Other than that, from the spectrograms reported in [5], it is rather clear how the working bandwidth of the P-band receiver is plagued by many RFIs. For this reason, and to reduce the overall bandwidth, the necessity to introduce multiple filtering stages, throughout the entire receiving chain, is risen. The schematic of the new dedicated channel for SD monitoring of the SRT is shown in Fig. 6.4, and is hereafter described in detail in every single block. The main blocks that compose the new channel are the L-P Receiver Block, the Down-conversion Block and the Back End.

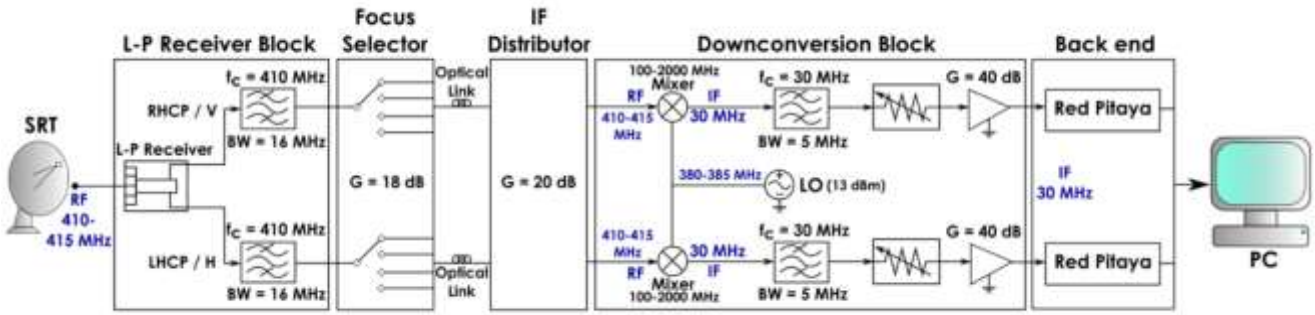

Fig. 6.4. Block diagram of the new SD dedicated receiving channel.

The only modification applied to the P-band receiver (reported in the schematic in Fig. 6.3 and indicated as L-P receiver block in Fig. 6.4) has been the insertion of two tubular 99.06 x 31.75 x 31.75 (mm) Band Pass Filters (BPF), model 3B110-410/T15-O/O purchased from K&L, centered at 410 MHz, with 16 MHz bandwidth and 1.1 dB of insertion loss. The characteristics of these filters are summarized in Fig. 6.5. With reference to the schematic in Fig. 6.3, the BPFs have been installed inside the P-band Filter

Selector block, in place of the “all-band” channels. The choice of the filter was not only influenced by the technical specification but also by the overall dimensions, due to the lack of available space inside the receiver block.

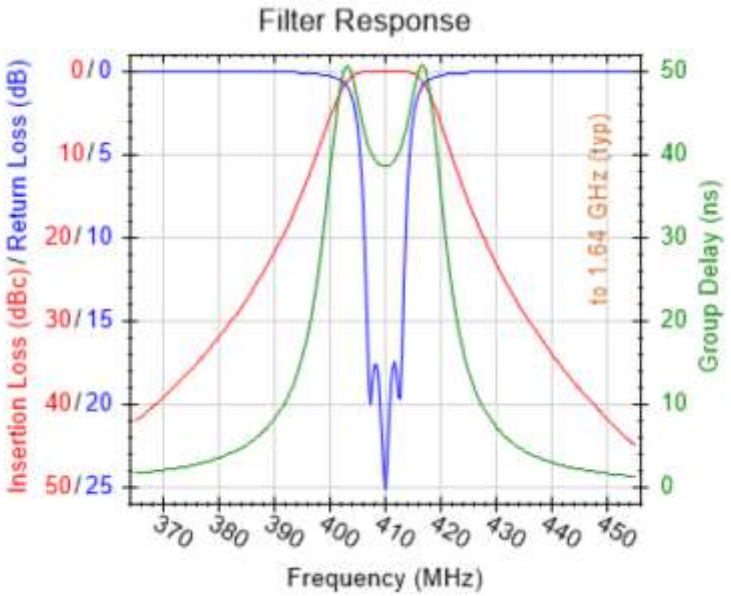

Fig. 6.5. Filter response of the BPF at 410 MHz installed on the L-P Receiver Block.

Fig. 6.6. Picture of the 16 MHz bandwidth tubular BPFs at 410 MHz (the larger ones) mounted inside the filter selector block of the P-band receiver.

Fig. 6.6 shows the picture of the BPFs mounted on the Filter Selector block. This filter allows a first discrimination of the frequencies of interest, decreasing the bandwidth of the P-band receiver (305-410 MHz) and partially mitigating the RFI problem. Before the signal reaches the second block, it has to pass through the focus selector module, which includes switches and Total Power detectors, and is composed by a set of amplifiers, variable attenuators and filters. The latter is used to select the focus of the SRT depending on the type of observation. This system is characterized by an overall gain of about 18 dB. In order to transfer the RF signal from the P-band receiver to the shielded room, where all the back-end used by the SRT are installed, an optical link is necessary. The choice of the optical link is tied to the minimum losses of the system with respect, for instance, to a coaxial cable link. The distance covered by the optical link, which is composed by an initial RF-optical transmitter, the optical fiber and a final RF-optical receiver, is of about 500 m, with a total loss of 0 dB. The IF distributor is placed downstream to the optical link. It allows the distribution of the RF signal coming from the antenna to the different back-ends installed inside the shielded room. This system is composed by an amplification stage and a set of passive splitters that separate the signal into three channels, one for each back-end. The overall gain of this section, which was absent during the 2014 experiments (confront Fig. 6.1 and 6.4), is of about 20 dB.

Although the base-band of the SRT ranges from 100 MHz to 2.1 GHz, in this case the insertion of a down-conversion block was necessary to match the working bandwidth of the dedicated back-end (0-50 MHz), based on the Red Pitaya board, which will be described later in this chapter. Hence, for each path inside the channel, the RF signal in input at the second block is down-converted to an Intermediate Frequency (IF) of 30 MHz and later filtered with a second BPF, model 3LB30-30/T5-O/O from K&L, centered at 30 MHz with 5 MHz bandwidth and 0.9 dB of insertion loss. The characteristics of these filters are summarized in Fig. 6.7.

The Local Oscillator (LO) frequency was tuned in the range 380-385 MHz, depending on the frequency of the input signal; the LO power was 13 dBm. It is worth mentioning that the level of LO power in input at the mixer has to be 10 dBm, thus we doubled the level to be equally shared between the two channels. The mixer is the ZFM-2000 model, from Mini-Circuits, working in the bandwidth 100-2000 MHz, with an isolation between the L-R and L-I ports of about 52 dB and 35 dB, respectively. Considering that, the echoes traveling back from the debris could be very weak, a further amplification stage has been placed before the back-end section. The amplifier is the ZKL-1R5 model, from Mini-

Circuits, working in the bandwidth 10-1500 MHz with about 40 dB gain at 30 MHz, a noise figure of 3 dB and an output power of about 17 dBm at 1-dB compression point. These features are reported in Fig. 6.8.

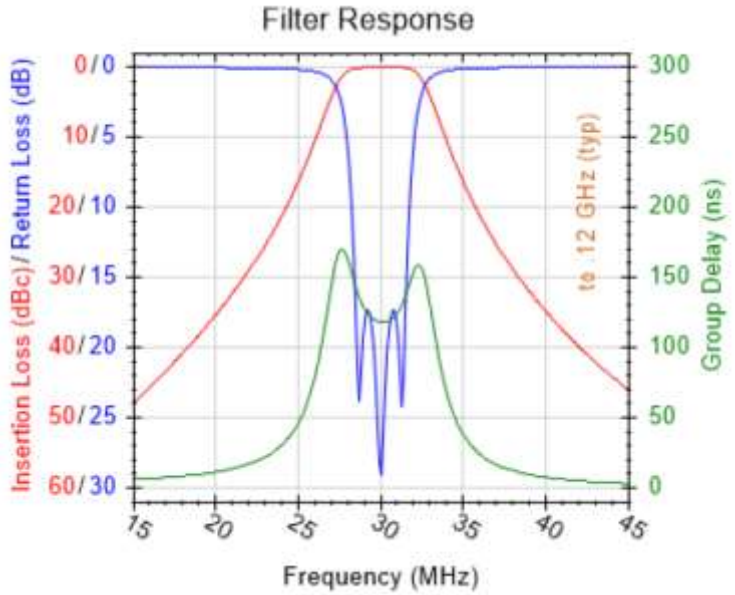

Fig. 6.7. Filter response of the BPF at 30 MHz installed on the Down Conversion Block.

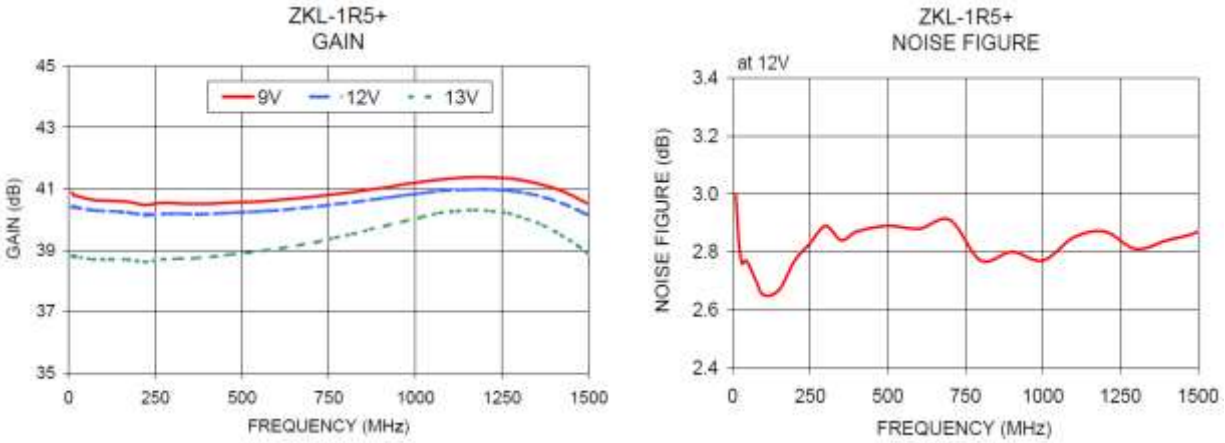

Fig. 6.8. Gain and Noise Figure of the amplifier installed on the Down Conversion Block.

In order to avoid the saturation of the amplifier, a wideband digital step attenuator has been placed upstream of the amplifier. The attenuator is the ZX76-31R75PP-S model, purchased from Mini-Circuits, characterized by a resolution of 0.25 dB, a maximum attenuation of 31.75 dB and controlled by a 7-bit parallel interface with a single positive supply voltage (Fig. 6.9). The control of the step attenuator is undertaken by the Red Pitaya, by means of the digital I/O pins available on the board, with a logic tension of 3.3

V. All the components described above are linked via SMA connector. As there was the necessity to feed the Red Pitaya, the amplifier (both working with 5 V) and the step attenuator (12 V), at the same time, for both channels, a simple rack for supply management has been designed and realized. Inside the supply rack, two commercial switching transformers from Traco Power, again one for each channel, provide the 5 V and 12 V feeding. For each tension provided by the transformers, a fuse has been used. Every fuse has a protection stage against possible short-circuit of the fed elements. Both the down-conversion block and the supply rack have been enclosed in an outer case of aluminum.

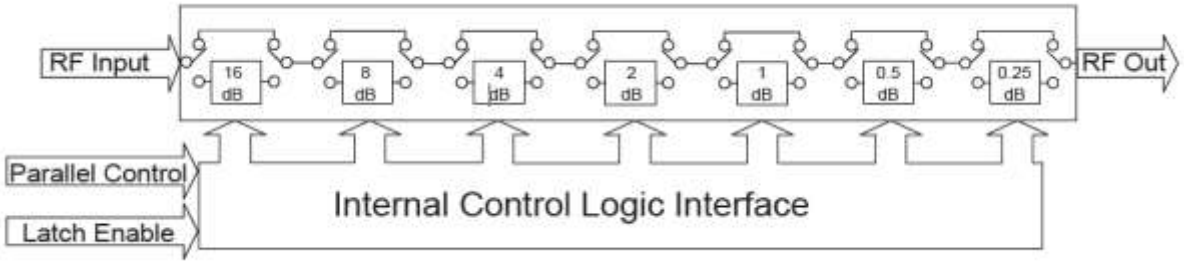

Fig. 6.9. Simplified schematic of the step attenuator.

Once the signals are properly conditioned (filtered and adapted in terms of power level), they are ready to be processed by the Red Pitaya. Hence, the two single polarization 5 MHz-wide signals centered at 32.5 MHz, are converted into digital format at the sampling frequency of 125 MSample/sec (each digital sample is represented with 14 bit) corresponding to an instantaneous bandwidth of 62.5 MHz, in accordance with the Nyquist's theorem. The Red Pitaya is a System-on-a-Chip (SOC) board characterized by a dual-core ARM9 processor, working at 800 MHz, a FPGA with 28 000 logic cells, 512 MB of DDR3 RAM system memory, 2 RF inputs and 2 RF outputs, an overall 3dB-bandwidth of 50 MHz, a sample rate of 125 Msps and 14 bit of ADC resolution.

At this stage, the general-purpose nature of the board allows any type of digital signal processing upon these signals. Initially, each Red Pitaya was able to provide the digital data in a "raw" format, via the 1 Gbit/sec link that the board is equipped with; in this case, the board would only operate as a digitizer and packetizer. However, because of the BPF at 30 MHz placed before the board, this unnecessary oversampling would be a useless waste of resource. In order to avoid the latter, a digital down-conversion (DDC) has been performed. The DDC converts a real, time domain signal into a complex one, centered in baseband. The process of frequency conversion is achieved by mixing the input signal with

a digital tone (i.e. a sinusoid) at the center of the bandwidth of interest, 32.5 MHz in our case. This creates two copies of the signal, one centered near zero, and one centered at twice the tone frequency. This is possible using a second sinusoid, out of phase by 90 degrees. A direct digital synthesizer (DDS) generates the sinusoids internally. Once the base-band complex data, a low-pass filtering is necessary to remove unwanted spectral information and to avoid aliasing phenomena. Since a considerable decimation is needed, we used the well-known CIC-FIR chain. The Cascade Integrator Comb (CIC) filter (also known as the Hogenauer filter) has proven to be an effective element in high-decimation systems, however CIC filters present an unsatisfactory frequency response, thus a Finite Impulse Response (FIR) filter is used in cascade so as to compensate the CIC response and, as a consequence, to improve the overall filter response. Fig. 6.10 shows a block diagram of the digital processing chain.

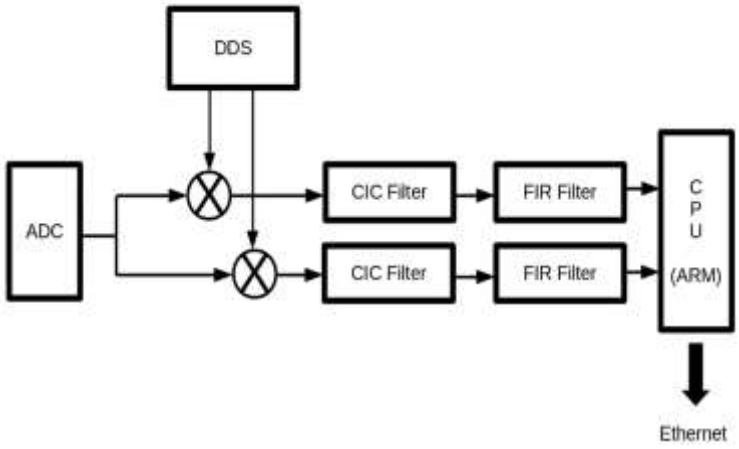

Fig. 6.10. Block diagram of the digital signal processing chain.

The described procedure creates a base-band complex signal that can be stored and subsequently divided in several sub-bands by means of a Fast Fourier Transform (FFT). The FFT engine could be implemented in the FPGA as well, however the number of spectral points would be limited by the available memory on the FPGA, thus the engine has been implemented in the CPU/GPU boards [22].

A complete characterization of the receiving chain has been performed in the Microwave Laboratory of the Cagliari Astronomical Observatory (INAF-OAC). The instrumentation employed for the characterization include: two signal generators, model SMC100A from Rohde & Schwarz, a spectrum analyzer, model FSV from Rohde & Schwarz, and a Vector Network Analyzer (VNA), model ZVA67 from Rohde & Schwarz. The first section to be characterized has been the P-band receiver block, with the latest

addition of the two BPFs at 410 MHz. For this measurement, the cryogenic front-end of the P-band receiver has been neglected, injecting a signal directly in the warm section (i.e. Linear to Circular Polarizer), and characterizing the whole block using the VNA. The response of the receiver block, in terms of scattering parameters, is reported in the results section. The down-conversion block has been characterized taking into account the overall conversion gain, the compression point and the evaluation of possible spurious frequencies, within the useful bandwidth, of the whole block. The conversion gain is a standard index of the performance of a heterodyne or super-heterodyne receiver system, determining, essentially, the amount of IF power at the output of the examined section, given an input RF power level. In order to produce this result, a RF signal of -40 dBm, spanning from 407 to 413 MHz, has been injected in the block using a signal generator, setting the LO power to 13 dBm and the frequency to 380 MHz. The RF signal level has been chosen low enough to avoid any saturation of the amplifier. A spectrum analyzer has been connected to the output of the amplifier of the acquisition chain, to detect the overall output signal. The conversion gain curve related to the down-conversion block is reported in the next section. The evaluation of the compression point of the chain is useful to predict the level of signal that induce a non-linear response, due to the saturation of the amplifier, that could, ultimately, produce signal distortion, and/or intermodulation products. In order to identify this value, a relatively low power signal has been injected at the top of the down-conversion block, and increased gradually, until the output signal started to flatten (as shown in Fig. 10 in the next section). The result of this measurement has been obtained as a function of the input power of the RF signal at 410 MHz. The RF input power has been varied from -40 dBm to -15 dBm with 1-dB steps. Once again the LO has been set with a power of 13 dBm and a frequency of 380 MHz. As for the analysis of the spurious frequencies, every contribution at the input of the block, including undesirable signals, could be potentially down-converted and fall into the receiving chain bandwidth. These frequencies can be evaluated using the following formula:

$$\omega_S = n \cdot \omega_{LO} - m \cdot \omega_{RF} \tag{34}$$

where ω_{LO} is the LO frequency, ω_{RF} is the input RF frequency and $\{n, m\} \in \mathbb{Z}$, $|n, m| \leq 5$. Higher values of the coefficients n and m give poor and, therefore, negligible contribution to the evaluation of the spurious frequencies. All the possible combinations of these values have been covered, giving no remarkable input in the IF bandwidth.

The system described in the previous sections has been tested during the recent re-entry of the Chinese space station Tiangong-1. The Chinese National Space Administration (CNSA) launched the space station in September 2011, from the Jiuquan space center. However, in March 2016, the CNSA lost contact with the Tiangong-1; thereby, the re-entry in the Earth's atmosphere was, probably, uncontrolled. The BIRALET system was able to observe two passages of the Tiangong-1 on March 29, 2018 using the new receiving channel in P-band, not long before the space station re-entered in the Pacific Ocean, at 00:16 UTC of April 2nd, 2018. The received echoes of the Tiangong-1 by the BIRALET system are reported later in this chapter.

The response of the P-band receiver, in terms of scattering parameters, with the addition of the BPFs at 410 MHz, can be seen in Fig. 6.11 and 6.12, which show the vertical linear polarization and horizontal linear polarization, respectively.

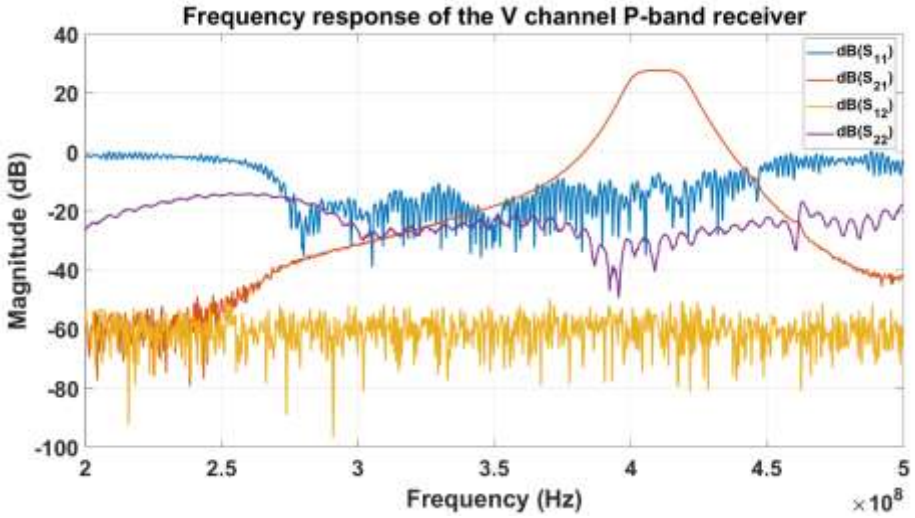

Fig. 6.11. Response of the vertical polarization channel, filtered with the BPF at 410 MHz.

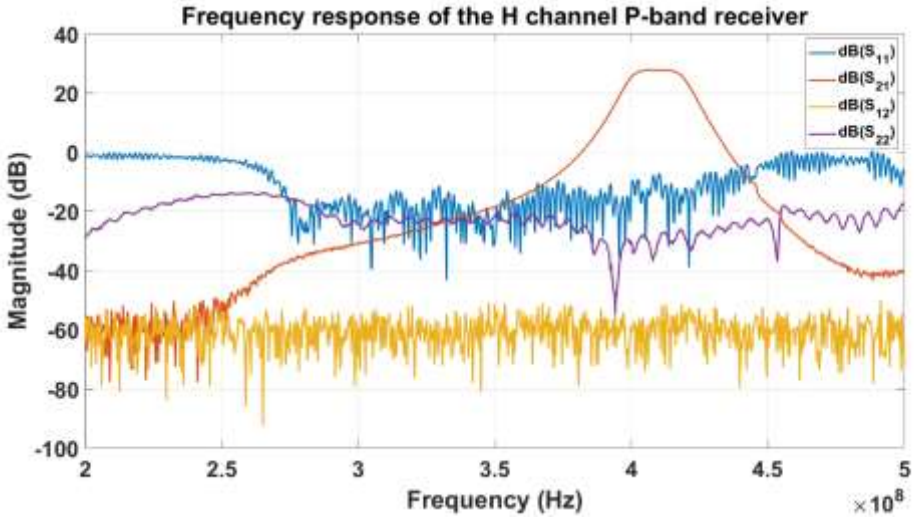

Fig. 6.12. Response of the horizontal polarization channel, filtered with the BPF at 410 MHz.

From the S_{21} curve, it is possible to appreciate the contribution of the BPF at 410 MHz that confines the signal in the 3-dB bandwidth 400.4-419.6 MHz. The S21 curve shows a maximum gain of about 27 dB, which matches, apart from some losses imputable to the coaxial cables used during the measurement, with the overall gain of the warm section of the P-band receiver (Fig. 6.3). The conversion gain of the whole down-conversion block is reported in Fig. 6.13 showing a 3-dB bandwidth of about 5 MHz, between 27.5 and 32.5 MHz, with a maximum value of 33 dB in the bandwidth 29-33 MHz. Obviously, such behavior was expected because of the BPFs centered at 30 MHz with 5 MHz bandwidth.

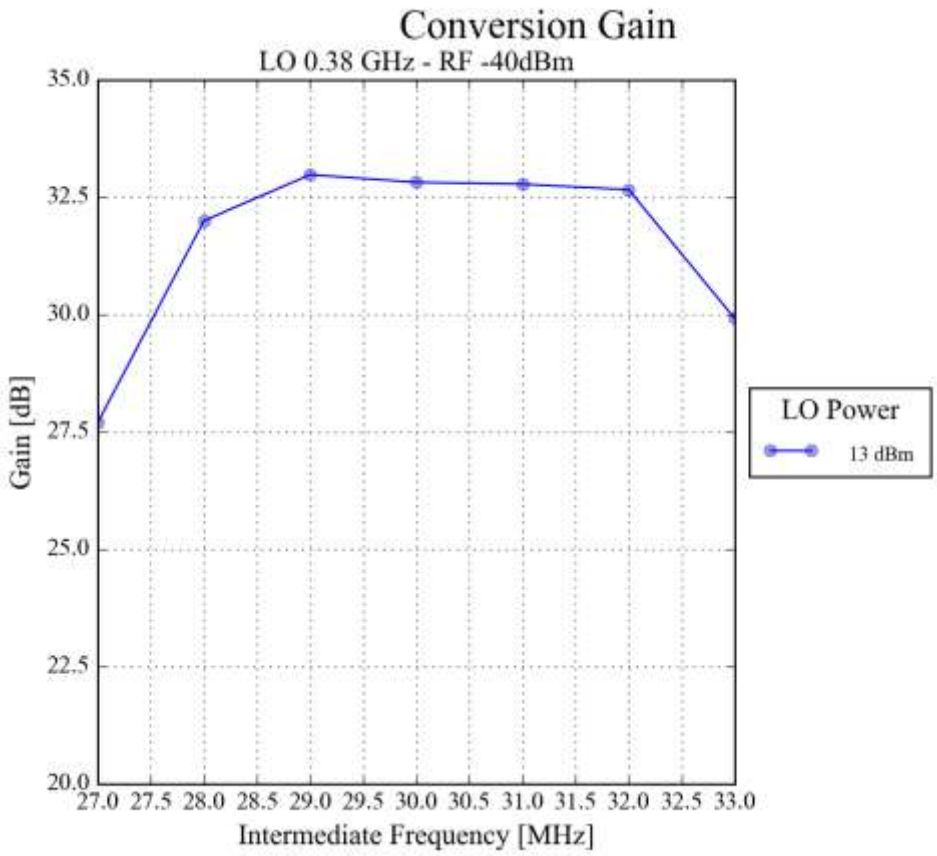

Fig. 6.13. Measured conversion gain of the down conversion block.

The 1-dB compression point is reported in Fig. 6.14. The dashed line represents the ideal output power and the slope of the curve represents the gain. The red line is the real output power of the block. It can be seen that the 1-dB compression point, after which the chain no longer works in the linear region and enters in the compression region, is found for the RF input signal equal to -21.24 dBm. This means that, for signals with a power of about -20 dBm in input at the down-conversion block, no further amplification occurs and signal distortion phenomena may begin to manifest.

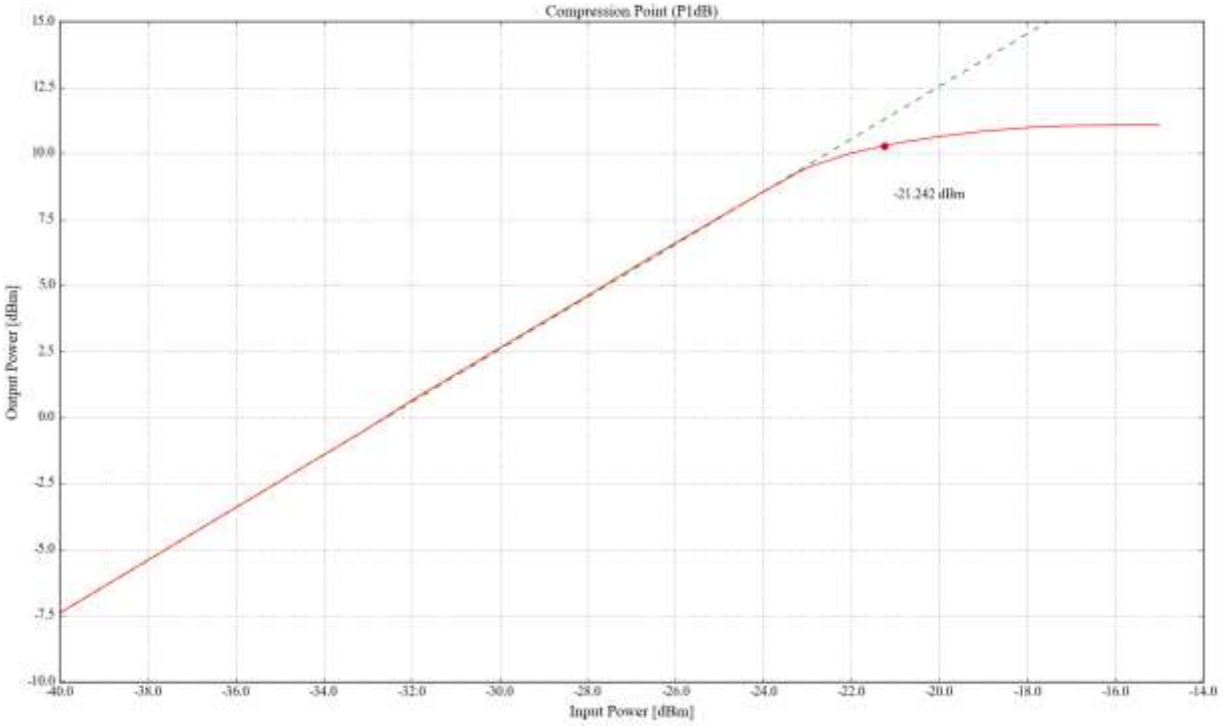

Fig. 6.14. Measured 1-dB compression point of the down conversion block.

Fig. 6.15. Picture of the down-conversion and back-end section of the new receiving channel.

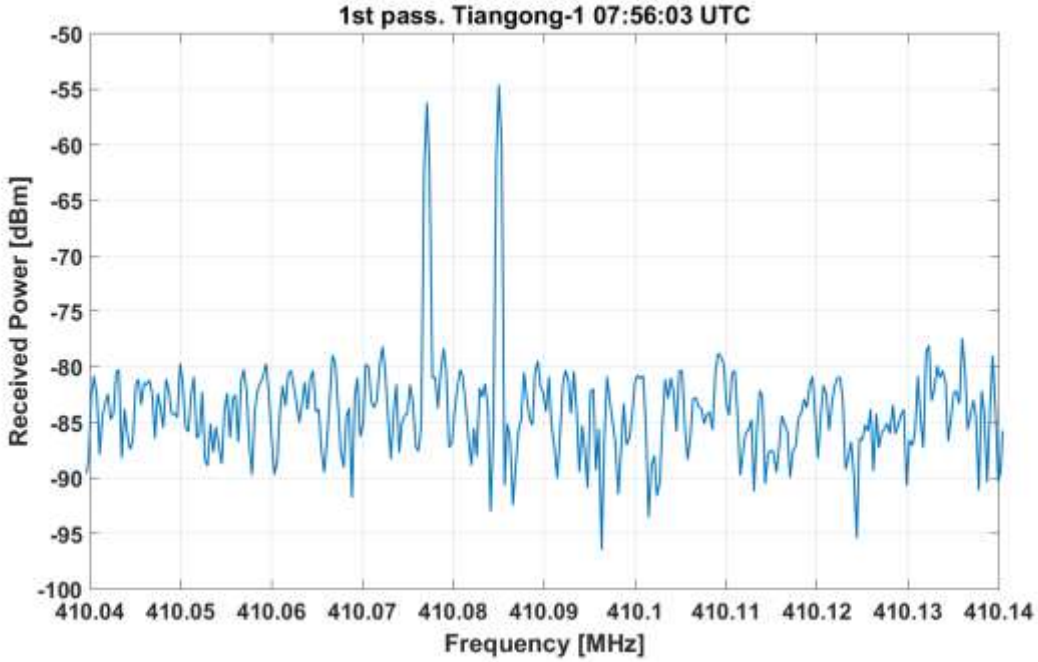

Fig. 6.16. Doppler of the first transit of the Tiangong-1.

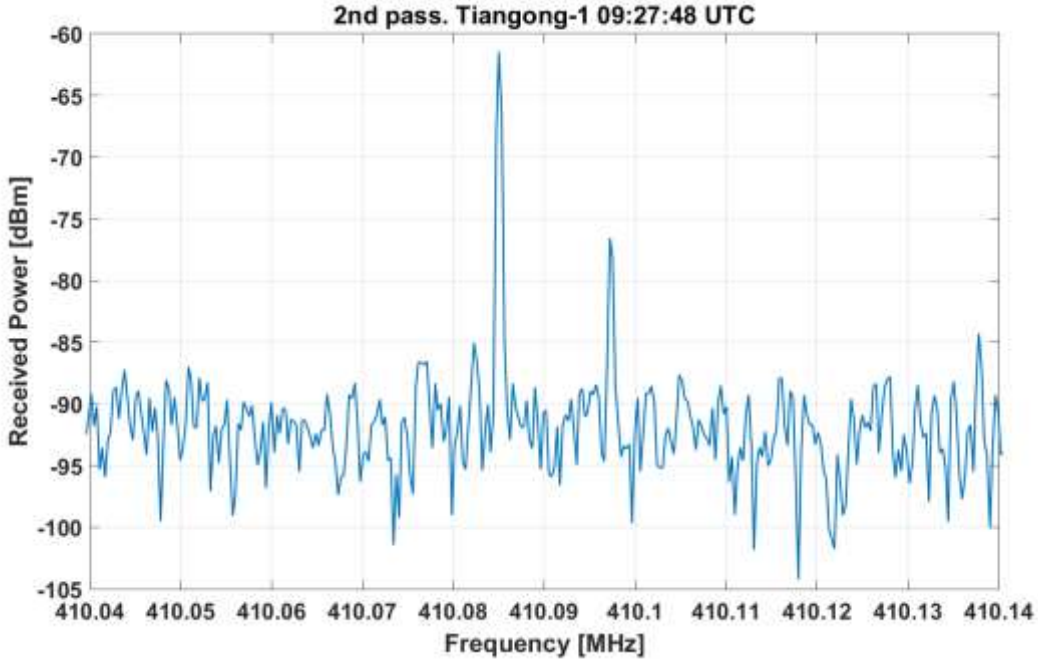

Fig. 6.17. Doppler of the second transit of the Tiangong-1.

A picture of the realized down-conversion and back-end section of the new channel is reported in Fig. 6.15. Within this picture it is possible to identify the components highlighted in Fig. 6.4. The measured Doppler of two passages of the Chinese space station

Tiangong-1 are reported in Fig. 6.16 and 6.17, whereas the spectrogram for the same passages is reported in Fig. 6.18 and 6.19. The first transits took place at 07:56:03 UTC of 29/03/2018, pointing the SRT toward 29.93° in azimuth and 24.38° in elevation with a measured Doppler of about -8 kHz, whereas the second transit took place at 09:27:50 UTC, pointing the SRT toward 268.05° in azimuth and 45.57° in elevation with a measured Doppler of about 12.5 kHz.

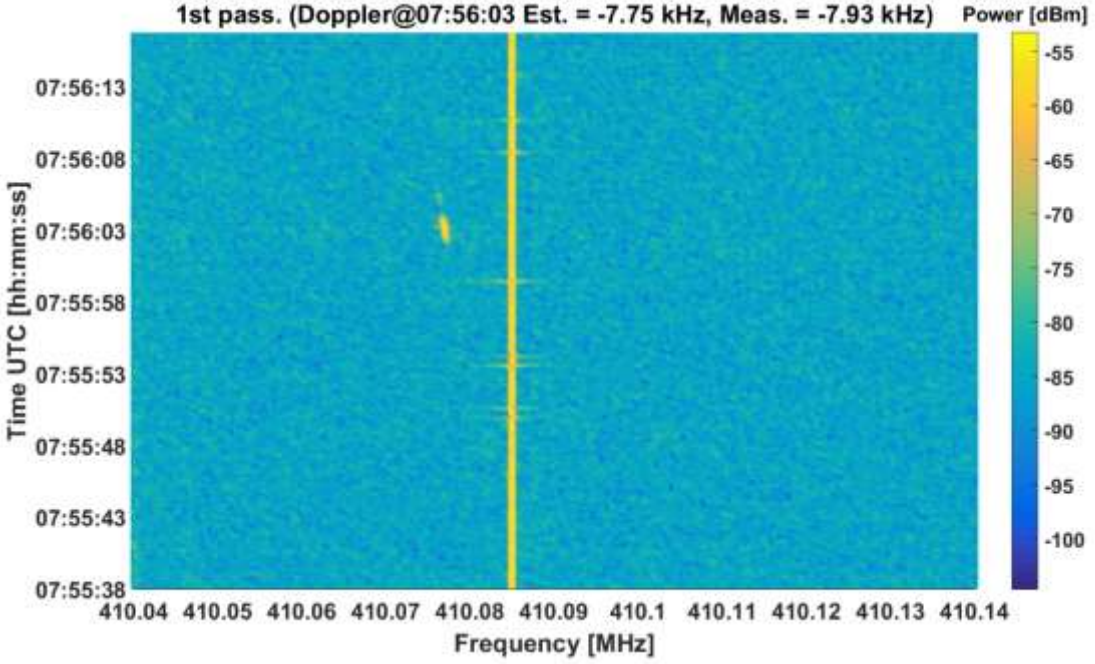

Fig. 6.18. Spectrogram of the first transit of the Tiangong-1.

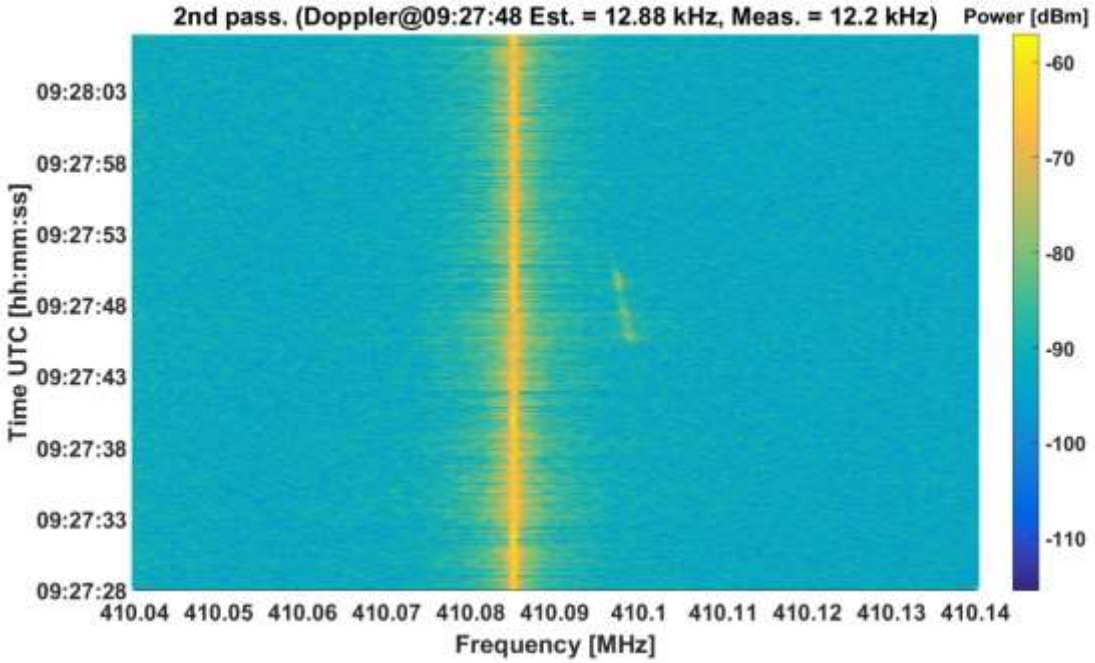

Fig. 6.19. Spectrogram of the first transit of the Tiangong-1

It can be noticed that the signal of the carrier from the transmitter is clearly visible, due to the proximity of the transmitter and receiver antennas. Thus, the Doppler frequency has been computed by the difference between the carrier frequency and the echo of the Tiangong-1. The results of the measurements are summarized in table 6.1.

Table 6.1. Summary of the 29/03/2018 measurements on the Tiangong-1.

Transit	**Time (hh:mm:ss) UTC**	**Azimuth (deg)**	**Elevation (deg)**	**Doppler (kHz)**	**SNR (dB)**
First	07:56:03	29.93	24.38	- 7.93	27
Second	09:27:48	268.05	45.57	12.2	18

It is worth remarking the difference between the Doppler measurements shown in chapter 5 and the Doppler measurements reported in this chapter. The background in the measurements of the 17/04/2014 is very noisy. The noise floor shows an excursion of about 20 dB, and if the echoes scattered from the debris were characterized by a lower SNR, the peaks could have been overlapped by the noise. In the new measurements the noise floor excursion is highly reduced. This means that the new back-end is much more sensitive with respect to the old acquisition setup, making possible the detection of echoes characterized even by a low SNR. Obviously this advantage can be exploited in order to be able to spot smaller and/or more distant objects.

7. CONCLUSION

Space debris are an important problem for space operations and a hot topic for the space surveillance research. A structured network of radar sensors is already present worldwide, giving vital information about the debris status. In recent years, also the Sardinia Radio Telescope (SRT), a 64-m dish located in Sardinia (Italy), has been inserted in the European plan for space debris monitoring and it has already shown its potential. In fact, during a measurement campaign in 17/04/2014, focused on the detection of debris and small-sized satellite, the SRT was able to detect every object within the list provided by the Italian Air Force. However, due to the fact that the radio telescope operating time is mainly devoted to radio astronomy applications, the necessity to upgrade the receiving chain of the SRT, not optimized for space debris' echo detection, is risen. For this reason, the research group of the Department of Electrical and Electronic Engineering of the University of Cagliari, in collaboration with the Cagliari Astronomical Observatory (OAC), has studied a set of upgrades for the L-P band receiver of the SRT, in order to make the antenna a suitable instrument within the European space debris detection plan. These modifications have resulted in the design, realization, characterization and testing of a new receiving channel for the SRT, specifically designed for space debris monitoring purposes. As regards the testing of the new receiving channel, we took advantage of the recent re-entry of the Chinese space station Tiangong-1, receiving the echo Doppler of the huge debris in two different passages. The new channel has shown better performances with respect to the receiving systems previously employed.

BIBLIOGRAPHY

[1] A. Ruggiero, P. Pergola, M. Andreucci, “Small Electric Propulsion Platform for Active Space Debris Removal”, *IEEE Transactions on Plasma Science*, vol. 43, pp. 4200–4209, 2015.

[2] M. Grassi, E. Cetin, A. Dempster, “Enabling Orbit Determination of Space Debris Using Narrowband Radar”, *IEEE Transaction on Aerospace and Electronic Systems*, vol. 51, pp. 1231-1240, 2015.

[3] United Nations, “Technical Report on Space Debris”, New York, 1999.

[4] F. R. Hoots, P. W. Schumacher, R. A. Glover, “History of Analytical Orbit Modeling in the U. S. Space Surveillance System”, *Journal of Guidance Control and Dynamics*, vol. 27 (2), pp. 174–185, 2004.

[5] G. Muntoni, L. Schirru, T. Pisanu, G. Montisci, G. Valente, F. Gaudiomonte, G. Serra, E. Urru, P. Ortu, A. Fanti, “Space Debris Detection in Low Earth Orbit with the Sardinia Radio Telescope”, *Electronics*, vol. 6 (3), 59, August 2017.

[6] A. Orfei, M. Morsiani, G. Zacchiroli, G. Maccaferri, J. Roda, F. Fiocchi, “Active Surface System for the New Sardinia Radio Telescope”, *Proceedings of SPIE 5495 Astron. Struct. Mech. Technol.*, 2004.

[7] H. Klinkrad, “Space Debris – Models and Risk Analysis”, *Springer*, 2006.

[8] M. I. Skolnik, “Radar Handbook”, *McGraw-Hill*, 1990.

[9] B. Weeden, P. Cefola, J. Sankaran, “Global Space Situational Awareness Sensors”, *Advanced Maui Optical and Space Surveillance (AMOS) Conference*, 2010.

[10] D. A. Vallado, J. D. Griesbach, “Simulating Space Surveillance Networks”, *Paper AAS 11-580 presented at the AAS/AIAA Astrodynamics Specialist Conference*, July 2011.

[11] P. Masekell, O. Lorne, “Sapphire: Canada’s Answer to Space-Based Surveillance of Orbital Objects”, *Advanced Maui Optical and Space Surveillance (AMOS) Conference*, 2008.

[12] J. Markkanen, M. Lehtinen, and M. Landgraf. "Real-time space debris monitoring with EISCAT", *Advances in Space Research*, vol. 35 (7), pp. 1197-1209, 2005.

[13] D. Mehrholz, L. Leushacke, R. Jehn, “The COBEAM-1/96 Experiment”, *Advances in Space Research*, vol. 23 (1), pp. 23-32, 1999.

[14] H. Wilden, C. Kirchner, O. Peters, N. Ben Bekhti, A. Brenner, T. Eversberg, “GESTRA – A Phased-Array Based Surveillance and Tracking Radar for Space Situational Awareness”, *2016 IEEE International Symposium on Phased Array Systems and Technology (PAST)*, pp. 1-5, 2016.

[15] J. Ender, L. Leushacke, L. Brenner, H. Wilden, “Radar Techniques for Space Situational Awareness”, *2011 IEEE Proceedings International Radar Symposium (IRS)*, pp. 21-26, 2011.

[16] H. Klinkrad, “Monitoring Space – Efforts Made by European Countries”, *International Colloquium on Europe and Space Debris*, November 2002.

[17] I. A. Gomez, S. A. Vildarraz, C. Garcia, J. M. H. Garnica, C. Perez Hernandez, M. A. R. Prada, J. U. Carrazo, G. M. Pinna, S. Moulin, P. Besso, H. Krag, J. R. Benayas, P. Ortiz Sanz, A. Gallego Torrego, A. M. A. Sanchez, N. Sanchez Ortiz, R. Dominguez Gonzalez, N. Ortiz, "Description of the Architecture of the Spanish Space Surveillance and Tracking System", *Proceedings of the 7th European Conference on Space Debris*, 2017.

[18] D. Ladd, R. Reeves, E. Rumi, M. Trethewey, M. Fortescue, G. Appleby, M. Wilkinson, R. Sherwood, A. Ash, C. Cooper, P. Rayfield. "Technical Description of a Novel Sensor Network Architecture and Results of Radar and Optical Sensors contributing to a UK Cueing Experiment", *Advanced Maui Optical and Space Surveillance (AMOS) Conference*, 2017.

[19] T. Pisanu, L. Schirru, E. Urru, F. Gaudiomonte, P. Ortu, G. Bianchi, C. Bortolotti, M. Roma, G. Muntoni, G. Montisci, F. Protopapa, A. Podda, A. Sulis, G. Valente. "Upgrading the Italian BIRALES System to a Pulse Compression Radar for Space Debris Range Measurements", *IEEE 22nd International Microwave and Radar Conference (MIKON)*, 2018.

[20] P. Bolli, A. Orlati, L. Stringhetti, A. Orfei, S. Righini, R. Ambrosini, M. Bartolini, C. Bortolotti, F. Buffa, M. Buttu, A. Cattani, N. D'Amico, G. Deiana, A. Fara, F. Fiocchi, F. Gaudiomonte, A. Maccaferri, S. Mariotti, P. Marongiu, A. Melis, C. Migoni, M. Morsiani, M. Nanni, F. Nasyr, A. Pellizzoni, T. Pisanu, M. Poloni, S. Poppi, I. Porceddu, I. Prandoni, J. Roda, M. Roma, A. Scalambra, G. Serra, A. Trois, G. Valente, G. P. Vargiu, G. Zacchiroli, "Sardinia Radio Telescope: General Description, Technical Commissioning and First Light", *Journal of Astronomical Instrumentation*, vol. 4 (03n04), 2015.

[21] E. Cenacchi, "SRT Project Book", version 1, May 2006.

[22] L. Schirru, G. Muntoni, T. Pisanu, E. Urru, G. Valente, F. Gaudiomonte, P. Ortu, A. Melis, R. Concu, G. Bianchi, G. Montisci, "Upgrading the Sardinia Radio Telescope to a Bistatic Tracking Radar for Space Debris", *1st IAA Conference on Space Situational Awareness (ICSSA)*, November 2017.

[23] G. Valente, A. Orfei, R. Nesti, A. Navarrini, S. Mariotti, P. Bolli, T. Pisanu, J. Roda, L. Cresci, P. Marongiu, A. Scalambra, D. Panella, A. Ladu, A. Cattani, L. Carbonaro, E. Urru, A. Cremonini, F. Fiocchi, A. Maccaferri, M. Morsiani, M. Poloni, "Status of the Radio Receiver System of the Sardinia Radio Telescope", *Proceedings of SPIE 9914*, July 2016.

ACKNOWLEDGEMENTS

Time to switch to Italian.

Durante tre anni la lista delle persone da ringraziare diventa importante. Il ringraziamento più grande va ovviamente al mio tutor, Giorgio, che mi ha dato fiducia e mi ha insegnato a relazionarmi al mondo della ricerca. Insieme a lui anche alle altre persone, all'interno del gruppo di elettromagnetismo, che hanno segnato profondamente il mio cammino da dottorando, in primis Alessandro (senza il quale il mio dottorato non avrebbe avuto ragion d'essere) e prof. Mazzarella (che risolve un problema apparentemente insormontabile in pochi istanti, con solo un foglio e una penna!).

Durante i miei tre anni da PhD ho trascorso buona parte del tempo in "adozione", presso l'Osservatorio Astronomico di Cagliari, dove ho conosciuto un gruppo di persone eccezionale, che ha aiutato la mia crescita, in particolar modo dal punto di vista pratico (componente, purtroppo, non particolarmente marcata nel corso degli studi universitari). Per questo motivo un grosso "GRAZIE" va a Tonino, per avermi permesso di lavorare sull'argomento degli space debris e avermi dato l'opportunità di lavorare, seppure a distanza, con il Sardinia Radio Telescope. Un ringraziamento che si estende a tutto il suo team e i suoi collaboratori: Enrico, Lino, Frank, Giuse, Adelaide, Andrea, Alessandro, grazie per aver condiviso la vostra esperienza con me.

Sempre in ambito OAC, un ringraziamento specialissimo va a chi ha passato innumerevoli giornate con me, all'interno del laboratorio di elettronica, al mio collega dottorando "sbertidori" Luca, col quale ho condiviso gioie, dolori e momenti di pausa memorabili (l'uscita di sicurezza docet), al mitico Gigione, il re dell'elettronica che con coraggio si oppose al regno di terrore della madre e infine a Robertino, la cui permanenza è stata breve ma intensa.

Doveroso ringraziamento ai miei colleghi dottorandi del laboratorio di elettromagnetismo, primo fra tutti Sergione, IL collega per eccellenza, col quale ho fatto "coppia fissa" per molto, molto tempo. Alle nuove leve, Nico e il buon Matteo Bruno. E non dimentichiamo quel fenomeno (da baraccone) di Marco!

Passando oltre (e in maniera piuttosto scontata) vorrei ringraziare tutta la mia famiglia, Cenzo e Rina, Marta e Paola, Max e Nico, Violetta e Chiccu.

E Vale, questa tesi, come sempre, è dedicata a te, semplicemente perché sei tu. Un grazie anche alla tua famiglia che ormai è un po' anche mia.